COMPARATIVE CT DENSITOMETRY OF MURINE PULMONARY DISEASE MODELS

COMPARATIVE CT DENSITOMETRY OF MURINE PULMONARY DISEASE MODELS

By

SHARON A. WHITTY, B.Sc.

A Thesis

Submitted to the School of Graduate Studies

in Partial Fulfilment of the Requirements for the Degree

Masters of Science

McMaster University

MASTER OF SCIENCE (2011) McMaster University

(Physiology and Pharmacology) Hamilton, Ontario

TITLE: Comparative CT Densitometry in Murine Pulmonary Disease Models

AUTHOR: Sharon A. Whitty, B.Sc. (University of Guelph)

SUPERVISOR: Dr. N.R. Labiris

SUPERVISORY COMMITTEE: Dr. A. Holloway

Dr. J. Valliant

Dr. M.D. Inman

NUMBER of PAGES: xiii, 149

ABSTRACT

Using micro-computed tomography it is possible to detect the presence of pathologies which alter the lung's normal density. The density of the lungs can be altered depending on the amount of air, tissue, cells or fluid they contain. Using established mouse models of house dust mite (HDM) induced asthma, TGF-β1 induced pulmonary fibrosis (PF) and lipopolysaccharide (LPS) induced neutrophilic inflammation, this thesis examines if CT densitometry can distinguish between different pathophysiological processes. An airway segmentation method was applied to the CT images and data from these regions were assessed to determine: first, if pathologies can be detected compared to control animals; secondly, if pathological progression within each model can be measured; and finally, if it is possible to distinguish between the pathologies themselves. Lung histology and bronchoalveolar lavage fluid cytology, and total lung resistance (for the asthma model only) were assessed to confirm the disease models. The results showed that a healthy lung can be distinguished from a diseased lung in all three models. Pathological progression and resolution were also visible in the asthma and LPS groups. No changes were noted between the examined time points in the PF model. This corresponded to histological findings. It is also possible to distinguish between many of the pathologies based on the density profiles alone. Thus, CT densitometry affords a non-invasive method to longitudinally assess disease progression and resolution which is useful for the testing of novel therapeutics within the same subject.

Regional CT density assessment, allows for the detection of localized pathologies around the airways which whole lung assessments may not be sensitive enough to detect.

ACKNOWLEDGEMENTS

I would like to thank all the people who helped me along the way. Without their help this Masters project could not be completed. First, to my supervisor N. Renee Labiris, for her support and patience; my committee members, Alison Holloway, Mark Inman, and John Valiant for their constructive criticism and intellectual input; Mark Inman and Russ Ellis for their help with the asthma model; Jack Gauldie and Jane-Ann Smith for assistance with the pulmonary fibrosis model; Iris Wang for her technical assistance and work on the pulmonary fibrosis and LPS inflammation models; Charlie Goldsmith for his assistance with the statistical analysis; Rod Rhem and Chantal Saab from Small Animal Medical Imaging at McMaster for their help with the CT and for their imaging expertise. A special thank you to: my family for always being there, the lab members in the Labiris lab for creating an entertaining working environment, and my dearest friends who were always there for me.

TABLE OF CONTENTS

1 INTRODUCTION 1
1.1 CT imaging 2
1.1.1 *CT Background* 2
1.1.2 Micro-CT Background 5
1.1.3 CT Densitometry 6
1.1.3.1 Standard Values of Attenuation 8
1.1.3.2 Clinical CT Densitometry of the Lung 9
1.1.3.3 Methods of CT Lung Densitometry 10
1.1.4 Micro-CT Densitometry 13
1.1.4.1 Segmentation Methods in Micro-CT Densitometry 14
1.1.5 CT Image Quality 15
1.1.5.1 CT vs. Micro-CT Image Quality 16
1.1.6 In Vivo Micro-CT Densitometry Imaging Considerations 17
1.2 Asthma 18
1.2.1 Clinical Presentation 18
1.2.2 Murine Asthma Models 19
1.2.2.1 Allergen Induced Murine Asthma 20
1.3 Pulmonary Fibrosis 21
1.3.1 Clinical Presentation 21
1.3.2 Murine Models of Pulmonary Fibrosis 22
1.3.3 Adenovirus vectors 24
1.3.4 Pathological Progression of PF in Mice after Delivery of adTGFβ1 24
1.4 LPS Induced Neutrophilic Inflammation 26
1.4.1 Clinical Relevance of the Experimental Model 26
1.4.2 Murine Models of LPS Induced Neutrophilic Inflammation 27
1.5 Current State of the Art Applications of Micro-CT in Mouse Models of Asthma, Pulmonary Fibrosis and LPS induced Neutrophilic inflammation 27
1.5.1 Current applications of quantitative micro-CT in mouse models of asthma or pulmonary fibrosis 29
1.6 Purpose of Thesis 30

1.7 Hypotheses 31
1.8 Specific Objectives 31
2 MATERIALS & METHODS 33
2.1 Materials 33
2.1.1 Solution Preparations 33
2.1.1.1 House Dust Mite (HDM) 33
2.1.1.2 Lipopolysaccharide (LPS) 33
2.1.1.3 Transforming Growth Factor Beta Adenovirus Vector (adTGF-β1) 33
2.2 Animals 34
2.3 Animal Models 35
2.3.1 Asthma 35
2.3.2 TGF-β1 Adenovirus Induced Pulmonary Fibrosis 37
2.3.3 LPS Induced Neutrophilic Inflammation 39
2.4 CT Imaging 40
2.5 Lung Segmentation 41
2.5.1 Airway Diameter 43
2.6 Physiology (Asthma Model Only) 44
2.6.1 Pressure Volume Analysis 44
2.7 Inflammatory Cells 45
2.7.1 Bronchoalveolar Lavage (BAL), Total and Differential Cell Counts 45
2.8 Histology 46
2.8.1 Preparation of Slides 46
2.9 Data Analysis 47
2.9.1 CT Image Analysis 47
2.9.2 Statistics 48
2.9.2.1 CT Densitometry Statistics for Individual Disease Models 48
2.9.3 CT Densitometry Statistics for Comparisons of Disease Models 51
2.9.4 BAL, TCC and DCC Statistics 53
2.9.5 Physiology Statistics (Asthma Model Only) 53
2.9.6 Airway Diameter 53
3 RESULTS 54
3.1 Asthma Model 54

3.1.1 Representative CT Images 54
3.1.2 CT Densitometry 56
3.1.3 Total and Differential Cell Counts 61
3.1.4 Histology 63
3.1.5 Physiology: Total Lung Resistance 65
3.2 LPS Induced Neutrophilic Inflammation 66
3.2.1 Representative CT Images 66
3.2.2 CT Densitometry 66
3.2.3 Total and Differential Cell Counts 72
3.2.4 Histology 73
3.3 Pulmonary Fibrosis 75
3.3.1 Representative CT Images 75
3.3.2 CT Densitometry 77
3.3.3 Total and Differential Cell Counts 80
3.3.4 Histology 81
3.4 Comparative CT Densitometry 83
3.4.1 Asthma and Pulmonary Fibrosis Model 83
3.4.1.1 Acute Asthma and Pulmonary Fibrosis Model 83
3.4.1.2 Chronic Asthma and Pulmonary Fibrosis Model 85
3.4.1.3 Recovery Following Chronic Asthma and Pulmonary Fibrosis Model 87
3.4.2 Asthma and Neutrophilic Inflammation Induced by LPS 89
3.4.3 Pulmonary Fibrosis and Neutrophilic Inflammation Induced by LPS 91
4 DISCUSSION 93
5 LIMITATIONS OF STUDY 107
6 CONCLUSIONS 113
7 FUTURE DIRECTIONS 114
8 BIBLIOGRAPHY 118
9 APPENDIX 135

LIST OF FIGURES

Figure 1. Schematic diagram of a typical CT system with fixed patient and rotating gantry..... 5

Figure 2. Definition of the relative area (RA) below -950 HU (RA-950) and 15th percentile point (Perc15)..... 12

Figure 3. Acute and chronic allergen experimental protocol. 36

Figure 4. TGF-β1 induced pulmonary fibrosis experimental protocol. 39

Figure 5. LPS induced neutrophilic inflammation experimental protocol.. 40

Figure 6. Large airway segmentation using Amira 5.2.1..... 43

Figure 7. Representative plot of # voxels vs density from a mouse large airway segmentation..... 48

Figure 8. Representative axial CT images of the lungs in the asthma model and their age matched and vehicle treated controls..... 55

Figure 9. Density distribution around selected large airways in mouse asthma models.. 57

Figure 10. Comparative density distributions of the region around the large airways of asthma models to controls..... 58

Figure 11. Comparative density distributions of the region around the large airways of asthma models. 60

Figure 12. Total cell counts (TCC) from BAL samples of asthma models.. 61

Figure 13. Differential cell counts (DCC) from BAL samples in the asthma models. 62

Figure 14. Representative lungs from asthma models. 64

Figure 15. Slopes from lung resistance compared to dose (Mch) in mouse asthma models. 65

Figure 16. Representative CT image of LPS induced neutrophilic inflammation.. 66

Figure 17. Density distribution around selected large airways in mouse models of LPS induced neutrophilic inflammation. 68

Figure 18. Comparative density distributions around selected large airways in mouse models of LPS induced neutrophilic inflammation from grouped vehicle treated controls.). 69

Figure 19. Comparative density distributions around large airways in mouse models of LPS induced neutrophilic inflammation..... 71

Figure 20. Total cell counts (TCC) from BAL samples of mouse models of LPS induced neutrophilic inflammation..... 72

Figure 21. Differential cell counts (DCC) from BAL samples of mouse models of LPS induced neutrophilic inflammation 73

Figure 22. Representative lungs from LPS induced neutrophilic inflammation models (X20).. 74

Figure 23. Representative axial CT image of the pulmonary fibrosis model following delivery of adTGF-B1 and their age matched and vehicle treated control..... 76

Figure 24. Density distribution of the large airway segmentation of pulmonary fibrosis.. 78

Figure 25. Density distribution of the large airway segmentation in pulmonary fibrosis models compared to controls..... 79

Figure 26. Total cell counts (TCC) from BAL samples of mouse models of PF 80

Figure 27. Differential cell counts (DCC) from BAL samples of mouse models of PF. 81

Figure 28. Representative lungs from adTGF-β induced PF models 2 weeks after delivery 82

Figure 29. Comparative density distribution around selected large airways of acute asthma (HDMA) and PF models. 84

Figure 30. Comparative density distribution around selected large airways of chronic asthma (HDME) and PF models.. 86

Figure 31. Comparative density distribution around selected large airways of the recovery group following chronic HDM exposure (HDMR) and PF models.. 88

Figure 32. Comparative density distribution of selected large airways in mouse models of LPS induced neutrophilic inflammation and asthma.... 90

Figure 33. Comparative density distribution around selected large airways in mouse models of PF and LPS induced neutrophilic inflammation 24 hrs after LPS delivery.. 92

Figure 34. Summary of CT densitometry of PF, asthma and LPS disease models 94

Figure 35. Mixed normal distribution curve fitting to large airway segmentation in a mouse..... 117

Figure 36. Representative cells in BALF from asthma models.. 135

Figure 37. Representative cells in BALF from LPS induced neutrophilic inflammation models (X40).. 136

Figure 38. Representative cells in BALF from adTGF-β induced PF models.. 137

Figure 39. Mean airway diameters of the asthma model.. 138

Figure 40. Mean airway diameters of mice 24 hrs after receiving LPS (n = 6) compared to controls (VEH) (n = 6). 139

Figure 41. Mean airway diameters of pulmonary fibrosis model. 140

Figure 42. Average lung volumes of mice in the asthma model compared to controls.. 141

Figure 43. Average lung volumes of mice in the LPS model after delivery of compared to controls. 141

Figure 44. Average lung volumes of mice in the pulmonary fibrosis model after delivery of adTGFβ-1 compared to controls.. 142

Figure 45. Comparison of the density distribution of selected large airways of two mouse strains (BALB/c and C57BL/6)..... 143

Figure 46. Age comparison of the density distributions of selected large airways in control groups of BALB/c mice..... 144

Figure 47. CT densitometry output from large airway segmentation in mice 2w after delivering TGF-β1. 145

Figure 48. Representational cumulative plot of baseline data in a large airway segmentation..... 146

Figure 49. Cumulative voxel frequency from -249.5 to 220 HU of the large airway segmentations in the three different mouse asthma models.. 147

Figure 50. Cumulative voxel frequency from -249.5 to 220 HU of the large airway segmentations of mice following exposure to LPS. 148

Figure 51. Cumulative voxel frequency from -249.5 to 220 HU of the large airway segmentations in mouse models of pulmonary fibrosis 149

LIST OF TABLES

Table 1. Visual Scoring CT images of 50 asthmatic patients and 10 healthy volunteers reported by four independent observers. 7

Table 2. Parameter 1. Comparison of vehicle control groups 49

Table 3. Parameter 2. Comparison of grouped vehicle data to exposure groups..... 50

Table 4. Parameter 3. Comparison of exposure groups within models ... 50

Table 5. Parameter 2. ANOVA Comparisons between disease groups... 52

CHAPTER 1

1 INTRODUCTION

Mice are one of the most commonly used experimental animals for preclinical studies. The ability to identify and distinguish between different pulmonary pathologies non-invasively in mice would be a valuable tool for longitudinal studies of disease progression and drug therapies. This would enable the study of temporal progression or resolution of pathologies in the same subject without the need of terminal procedures, and thus, eliminate inter-subject variability (Grenier et al, 1996; Guerrero et al, 2007; Cavigli et al, 2009).

Using micro-computed tomography (micro-CT) it is possible to detect the presence of pathologies which alter the lungs' normal density. The lungs possess a distinctly lower density than the surrounding tissues which can be altered depending on the amount of air, cells, tissue or fluid they contain. Density changes have been quantified in CT images in animal models of pulmonary fibrosis, emphysema and asthma in both mice and rats, but so far no attempt appears to have been made to determine if quantifiable differences occur between disease models or if CT is sensitive enough to determine changes in disease progression. The ability to determine changes in the pathology of the lung would be useful because it would provide a non-invasive technique, which

enables longitudinal assessment within the same animal which is beneficial for pre-clinical studies of novel drug therapies.

This thesis examined the possibility of differentiating between the presence of fibrosis, airway remodelling, and eosinophilic and neutrophilic inflammation using quantitative micro-CT. This was accomplished by comparing CT densitometry of the main airways in established murine models of asthma, pulmonary fibrosis, and LPS induced neutrophilic inflammation. For each model total and differential cell counts, histology, and in the case of the asthma model, physiology measurements were performed to ensure that the models were accurately created.

1.1 CT imaging

1.1.1 *CT Background*

Since the discovery of X-ray radiation in 1895, X-rays have been used to create non-invasive images of a structure based on differences in tissue densities (Poulsen and Simonsen, 2006). X-rays are produced by first applying a high energy source to a cathode in a vacuum. The cathode releases electrons which hit an opposite anode (metal target eg. tungsten) and this momentarily disrupts the normal electron shell configuration of the metal. As electrons in the metal fall to lower energy states high energy electromagnetic waves called photons are released. Photons produced in the energy range of 200 eV to 1 MeV are X-rays

(Suryanarayana & Norton, 1998). To control which X-ray energies are produced from the X-ray spectra (200 eV to 1 MeV) the voltage applied at the cathode is regulated. More energy (measured in kilovolts (kv)) at the cathode would produce higher energy X-rays that penetrate tissues easier. In X-ray imaging an object is exposed to an X-ray radiation source and, 180° on the opposite side, a detector (or film) measures the amount of radiation passing through the object. The image is produced by the extent of energy reaching the detector (or film). The amount of X-rays reaching the detector depends on the density of the material. As X-ray photons pass through the material they interact with the electrons of the molecules. From these interactions photons are either absorbed (halted) or deflected (photon scatter decreasing energy) (Suryanarayana & Norton, 1998). Denser materials have higher electron density causing increase X-ray attenuation. These density differences create an image with tones ranging from white to black; denser regions (higher attenuation regions) appear as lighter underexposed sections and less dense regions (lower attenuation regions).

The images produced are planar projections containing superimposed structures in the imaged region. Many improvements in imaging technology have enabled increased resolution of the images. These advances have contributed to improve diagnostic testing; however, imaging capabilities are limited to visualizing the structures on a two dimensional (2D) plane, excluding a great deal of anatomical information (Dobbins and Godfrey, 2003).

Computed tomography (CT) was invented in the early 1970s by G.N. Hounsfield (Hounsfield, 1973). His system used principles similar to projection radiography, in which the subject is exposed to a source of X-ray radiation, however, Hounsfield took multiple planar images 360° around the subject, captured the information with a detector linked to a computer, and reconstructed this data to create a 3D image (Hounsfield, 1973). By combining information from multiple planar images this method creates a non-invasive way of visualizing 3D structures. The resulting image is comprised of 3D pixels, called voxels, and provides spatial and volumetric data as well as an average attenuation value determined by the amount of X-rays detected by the detector, measured in CT units.

Since the 1970s the basic components of the CT have remained the same: the gantry, where the radiation source and the detector are affixed on opposite sides; the table, where the subject (or object) lies; and the computer system (**Figure 1**) (Paulus et al, 2000). However, many improvements in technology have been made: continuous spiral acquisitions; increased number of detectors (multi-detector CT (MDCT)); decreased size of the X-ray focal lens; and the use of cone beam X-rays, are just some of the changes which have all led to improving overall image quality and decreasing acquisition time (Paulus et al, 2000).

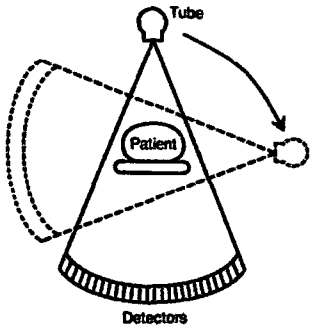

Figure 1. Schematic diagram of a typical CT system with fixed patient and rotating gantry. (Smith, H.J. GE Health, Medical Diagnostics, 2011)

1.1.2 Micro-CT Background

Micro-CT is a smaller scale CT machine which produces voxel sizes in the micrometer range (as opposed to millimetres in most clinical CTs). This is useful for imaging structures such as the lungs of small rodents, which have large airway diameters around 500 – 700 µm. The use of micro-CT for rodent imaging was not common until the mid-to-late 80s when the technology made it feasible to produce images of acceptable quality (Paulus et al, 2000). Presently, technical advances in the focal lens size enable the production of images that can be reconstructed with ~ 10 µm voxel size (Lee et al, 2008). Continued improvements in micro-CT imaging technology have enabled the production of high quality *in vivo* images of small animals. Micro-CT has been employed in studies of animal models of pulmonary diseases such as fibrosis, emphysema, cancer, and asthma in both mice and rats to visualize and quantify pathologies and in some cases track disease progression (Postnov et al, 2005; Froese et al, 2007; Guerrero et al, 2007; Ask et al, 2008; Lee et al, 2008; Jobse et al, 2009; Lederlin et al, 2010).

1.1.3 CT Densitometry

Classically, CT imaging is used as a non invasive way to view anatomical structures within the human body. Each tissue possesses a specific density, thus, changes in tissue density may indicate the presence of pathologies. Visual interpretation of CT images for various disease diagnoses and staging is still the main application of CT using visible differences in tissue density to distinguish healthy from diseased tissues. However, visual interpretation alone is relatively subjective based on the observer. For example, the feasibility of using CT to identify various pathologies in asthma patients was studied by Grenier and colleagues by analyzing the outcomes of four observers. The results found a certain degree of 'acceptable' intra-observer and inter-observer variability (kappa > 0.40) present (**Table 1**) (Grenier et al, 1996). In some clinical studies the use of quantitative outcomes derived from visual assessment are used to produce a standardized interpretation of disease progression; this has been reported for chronic obstructive pulmonary disease (COPD), pulmonary fibrosis, and cystic fibrosis (Akira et al, 2009; Ask et al, 2008; Saavedra and Lynch, 2009). These outcomes, although providing a quantitative value for disease staging, again are reliant on the observer's interpretation and are associated with observer variability (Akira et al, 2009).

Table 1. Visual Scoring CT images of 50 asthmatic patients and 10 healthy volunteers reported by four independent observers. Kw (kappa within) observer agreement, Kb (kappa between) observer agreement, P is statistical significance. (Grenier et al, 1996)

CT findings	*Kw* (*P*)	*Kb* (*P*)
Bronchial wall thickening	0.65 (< 10^{-5})	0.59 (< 10^{-5})
Bronchiectasis		
Presence	0.79 (< 10^{-5})	0.64 (< 10^{-5})
Type	0.62 (< 0.001)	0.35 (< 0.001)
Location	0.61 (< 0.001)	0.40 (< 10^{-5})
Distribution (lobar)	0.68 (< 10^{-5})	0.48 (< 10^{-5})
Mucoid impaction	0.57 (= 0.001)	0.24 (NS)
Small centrilobular opacities	0.60 (< 0.005)	0.52 (= 10^{-5})
Decreased lung attenuation	0.64 (= 10^{-4})	0.40 (< 10^{-5})
Thick linear opacities	0.62 (= 10^{-4})	0.48 (< 10^{-5})
Airspace consolidation	0.70 (< 0.01)	0.48 (NS)

NS, not significant

Using CT it is possible to quantify density changes in a chosen region instead of relying on visual interpretation. Some of the benefits of this include the production of data that avoids biases and variability caused by the interpreter (Grenier, et al, 1996), the possibility of finding early pathological changes the human eye might not be able to detect (Akira et al, 2009) and the ability to measure density changes within a 3D space (Froese et al, 2007). Quantitative CT, termed CT densitometry, is possible because the output data of the image is a physical map divided into voxels (each of a specific physical location and average attenuation value) which provides regional density measurements of a subject. Density changes can be derived from attenuation changes since the attenuation values acquired are linearly related to the density of the tissues imaged (Robinson, 1979).

1.1.3.1 Standard Values of Attenuation

To assist in the interpretation of CT densitometry, attenuation values (called CT units) can be converted to relative density values called Hounsfield Units (HU). This is performed using standards of water and air imaged under the same conditions. Following imaging CT units are measured by selecting a region of interest within a water standard and the air space in the CT image. These values are then set to equal 0 HU and -1000 HU respectively. All other CT units are then converted to HU using a linear scale with the value for air (as -1000 HU) at one end and water (as 0 HU) at another. Thus, each voxel will possess a specific average HU value; for example voxels possessing a value of 0 HU will have a density equivalent to water (Hounsfeld, 1973). The benefit of using this standardized value is to regulate for variation in attenuation values. Since the attenuation measurement depends on the amount of X-ray radiation reaching the detector, variations will occur when: different X-ray energies are used, the length of image acquisition is changed or from variation between machines, as well as within the same machine following calibration (Levi et al, 1982). Therefore, using HUs as the measure of attenuation, longitudinal scans can be compared between time points with minimal concern of variations due to factors other than density changes within the subject's tissues.

1.1.3.2 Clinical CT Densitometry of the Lung

The common elements employed in CT densitometry are the creation of a region of interest (ROI) and then a quantitative assessment of the density profile within this region. For practical purposes only lung CT densitometry will be examined for the remainder of this thesis.

Lung X-ray densitometry has been applied since the 1960s and CT densitometry since the late 1970s (Wegener, 1978; Robsinson, 1979). There are many benefits to employing CT densitometry in the lung. The first is that the lung is comprised of air (-1000 HU) and tissues (blood, cells, fluid; 0 HU), which result in an average lung density < 0 HU (Simon, B. A. et al, 2005). This makes it easy to distinguish and segment the lung from surrounding tissues (eg. skeletal muscle, bones, and vasculature). Another advantage of CT lung densitometry is that alterations in lung density (via destruction of parenchyma tissue, inflammation and/or fibrosis) are usually associated with physiological changes (Washko et al, 2008). Therefore, CT can be used to assist in disease staging, and developed CT densitometry methods can be validated with gold standard pulmonary function tests. In addition, regions of pathology are relatively easy to measure since the presence of increased fluid, cellular infiltrate, or tissue mass will increase densities in the area around 0 HU; whereas destruction of tissue or expansion of the airspace will increase regions in the < 0 HU range.

Currently, lung CT densitometry is not readily used in clinical practice, but methods are being standardized and validated to describe pathologies and

characterize pathological progression in COPD, sarcoidosis, idiopathic pulmonary fibrosis, asthma, pulmonary edema, acute respiratory distress syndrome, and cystic fibrosis (Stoel and Stolk, 2004; Best et al, 2008; Boehm et al, 2008; Coxson, 2008; Goris et al, 2003).

So far, COPD remains the disease with the most research being done on developing a standardized CT densitometry method. Research in this area focuses on developing a method for clinical use in addition to providing a better phenotypic description of the disease (Coxson, 2008; Washko et al, 2008). Recent work in COPD will be discussed briefly in order to introduce common methods of segmentation and analysis in clinical research, since they have also been applied in various animal studies as well as in this thesis.

1.1.3.3 Methods of CT Lung Densitometry

Entire 3D lung segmentations are commonly employed in clinical studies of COPD since 2D lung sampling is not depictive of the entire lung (Wegener, Koeppe, and Oeser, 1978). The lung segmentation is created using density thresholds to define the lung region, and the histogram produced (**Figure 2 A**) can be interpreted in many ways. Full lung segmentation has been applied in clinical studies of COPD to assess density changes since both the destruction of the lung parenchyma and airway obstruction result in increased areas of air trapping producing an overall decrease in mean lung density (Stoel and Stolk,

2004; Washko et al, 2008). Thus, progression of the disease increases regions of low attenuation within the lung.

One outcome measurement commonly used to measure density changes in the lung is the mean lung density (or attenuation) (MLA), which is simply the average of the density values of all the voxels in the lung segmentation. Using this technique, Cavigli and colleagues, have shown that entire lung CT densitometry in patients with emphysema is more accurate than visual assessment at predicting severity of disease (Cavigli et al, 2009).

Although MLA is commonly used and has been correlated with pulmonary function tests in COPD, it is found to lack sensitivity since small changes are not always detectable (Akira et al, 2009). Thus, new parameters have been examined to focus on pathological changes associated with the disease. Individuals with COPD express emphysematous or air trapped regions in the lung which are measured as regions of low attenuation by CT. Thus, an evaluation of the number of voxels from a predetermined density threshold in the less dense range (-910 or -950 HU for COPD) has been applied. This has been termed the relative area (RA) of lung (**Figure 2 B**). Another variation of RA determines the density (in HU) where the n^{th} percentile occurs instead of using an arbitrary threshold value; this is determined using a cumulative plot (**Figure 2 B**). These measurements focus on the area of the lung in the less dense region, which is associated with pathological progression in COPD.

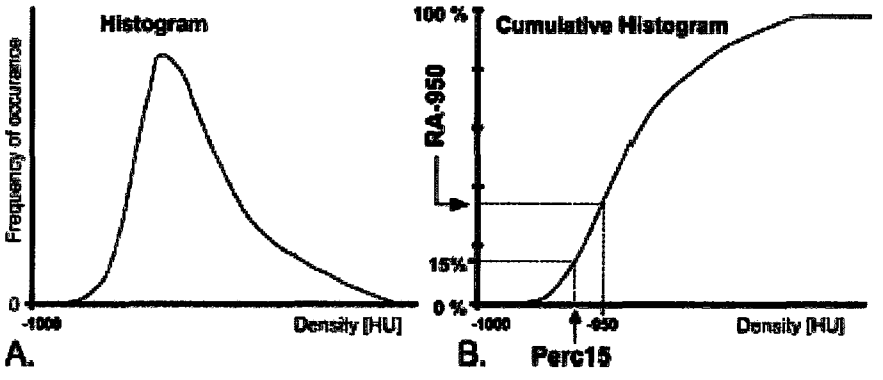

Figure 2. Definition of the relative area (RA) below -950 HU (RA-950) and 15th percentile point (Perc15). (A) Typical histogram of the densities in the human lung. (B) Cumulative histogram by which Perc15 and RA-950 have been defined (Stoel and Stolk, 2004).

It has been found that the strength of the correlation between pulmonary function tests and the quantitative outcomes depends on the methods used in the densitometric analysis (Stoel and Stolk, 2004). These commonly employed methods: MLA, RA (-910 and -950 HU), and n^{th} percentiles (5^{th} and 15^{th}) were assessed in patients with COPD at inspiration and expiration and compared to visual assessment using a gold standard visual scoring method and pulmonary function tests (Akira et al, 2009). This work has indicated MLA is not as sensitive as the RA or nth percentile (nth) in predicting COPD severity, and RA is not as sensitive as the nth percentile for detecting early onset (Stoel and Stolk, 2004, Akira, M., 2009). These results show the importance of choosing the appropriate densitometric measurements (MLA, RA, and nth percentile) in accordance with a desired outcome (Stoel and Stolk, 2004).

The segmentation itself depends on what aspect of the lung you are trying to assess. When trying to correlate density changes with resistance of the airways in COPD, a full lung assessment was found to be an inappropriate segmentation protocol since the changes in lung density were not dependent on resistance. Instead regional airway analysis has been used to look at more specific pathologies. For example, resistance in the airways present in COPD is produced by airway collapse. Yamashiro and colleagues have shown that regional assessment of the changes in distal bronchial wall attenuation has a better correlation with airflow obstruction than MLA (Yamashiro, 2010). Thus depending on the specific aspect of the disease being examined, either full lung or localized region attenuation changes, such as the airways, were shown to be useful.

1.1.4 Micro-CT Densitometry

Some of the benefits of micro-CT lung densitometry for animal models are being able to track anatomical and physiological changes over time within the same animal. This makes it possible to measure disease progression within the same animals longitudinally as well as quantify possible improvements in pulmonary pathologies with the use of therapeutic drugs. Additional benefits include the derivation of functional data such as functional residual capacity and tidal volume from images (Schuster et al, 2003). This was explored by Guerrero, in a murine model of pulmonary fibrosis induced by irradiation. Lung compliance was measured using lung volumes acquired from 3D lung segmentations of

micro-CT images (Guerrero et al, 2007). Finally, the ability to assess pathological changes in a three dimensional space is extremely useful for quantifying and tracking heterogeneous pathologies in the lung, since a 2D lung slice might not be representative of the extent of pathological progression (Froese et al, 2007).

1.1.4.1 Segmentation Methods in Micro-CT Densitometry

Methods of analysis in mouse and rat models of pulmonary disease have included full lung segmentations (Froese et al, 2007), thoracic segmentations (Jobse et al, 2009, Ask et al. 2008), and regional segmentations (Lederlin et al, 2010). Like in clinical research, lung segmentation can be employed using a semi-automated program that isolates the lung based on a specific density range (Froese et al, 2007). This has been employed in mouse models of emphysema (Froese et al, 2007), however, pulmonary diseases that produce increased attenuation values in the lung, due to the presence of either fluid, cellular infiltration or fibrotic tissue, hinder the ability to isolate the lungs from surrounding tissues based on density values typical of a normal lung. Thus, indirect measurements have been performed such as measuring changes in lung volume using region growing algorithms or thoracic segmentation (Cavanaugh et al, 2006; Rodt et al, 2010; Ask et al, 2008; Jobse et al, 2009). These methods have been applied in studies using micro-CT to assess lung damage in mice and rats with pulmonary fibrosis (Cavanaugh et al, 2006; Rodt et al, 2010; Ask et al. 2008) and in rat models of asthma (Jobse et al, 2009). In addition, a direct regional

measurement of airway density has also been examined in a mouse model of asthma, which is characterized partly by structural airway changes (Lederlin et al, 2010). These have all been shown to be useful for characterizing the presence of pathologies in pulmonary disease that increase lung density.

1.1.5 CT Image Quality

The accuracy of the CT densitometry outputs depends on the CT imaging and reconstruction protocols. These affect image quality which, in turn, will affect the accuracy of the attenuation values and the ability to segment fine structures. This section will mention factors affecting CT image quality that can easily be altered, since they are pertinent to this thesis.

The parameters that are chosen for the CT protocol include image acquisition time, X-ray energy, the number of rotations, and the voxel size at which the image is reconstructed. These all contribute to image quality. Essentially, when the data is first reconstructed, producing the 3D image, many assumptions are made based on the number of X-rays reaching the detector. The main assumption is that all the X-rays measured at the detector have traveled linearly from the source. This idea assumes that random X-ray scatter does not occur and neighbouring tissues do not affect local X-ray attenuation values (Levi et al, 1982). The detector and the focal lens are collimated to attempt to regulate the direction of the radiation to decrease random photon scatter, however, some variability, termed noise, will still be present in the data. As noise increases the

accuracy of the attenuation values decrease. Variability of attenuation values (noise) increases with decreasing X-ray energy, less projections/shorter acquisition, and smaller voxel size. These all decrease the amount of X-ray attenuation information describing the object.

1.1.5.1 CT vs. Micro-CT Image Quality

The spatial resolution and image contrast are two measured outcomes that are affected when components such as voxel size and X-ray energy are altered. Voxel size mainly dictates the spatial resolution. Clinical CT images of the lungs are generally reconstructed to produce 1.25 mm slices to visualize the fine structures of the pulmonary airways and vasculature (Akira et al, 2009). In pre-clinical imaging the voxel size would need to be smaller (46 – 150 μm) in order to define the fine micro-structures of the rodent lungs (Tanimoto and Arai, 2009). When imaging on the micro-scale, using small voxel sizes, a high degree of variability is present in the attenuation values. To improve the accuracy of CT densitometry outputs, it has been suggested that the use of larger voxel sizes in clinical studies will reduce the amount of noise (or variability of attenutation values) (Stoel and Stock, 2004). However, this is not possible in pre-clinical imaging; thus, micro-CT densitometry in the rodent lung will always have an increased variability in the outputs compared to clinical CT densitometry in the lung.

Image contrast depends largely on the X-ray energy used which is chosen based on the organ being imaged as well as the size of subject (such as in the case of pre-clinical imaging). The thorax which is made up of high contrast tissues would require less energy to be able to produce sufficient image contrast. The voltage used for clinical CT scans of the lungs is around 120 Kev (Akira et al, 2009). For animal studies lower energies are used (~70-80 Kev) to improve contrast in the soft tissues of the rodent lung since body thickness is significantly smaller, thus, less energy is needed to penetrate the tissues. This decrease in X-ray energy is also associated with a higher degree of variability in the attenuation values of the image.

Hence, pre-clinical imaging of rodent lungs with a micro-CT has inherently more error associated with it compared to the common CT parameters used in human lung studies.

1.1.6 In Vivo Micro-CT Densitometry Imaging Considerations

When imaging live animals there are certain aspects that must be considered in order to accurately evaluate the lung and perform safe and repeatable experiments. Lung density changes readily with the breathing cycle and this translates to CT lung densitometry changes with images of inhalation and exhalation producing different histograms (Wegener et al, 1978). In human imaging studies patients hold their breath during imaging. For animals, respiratory gating software which compartmentalizes the data into full inhalation

and exhalation, or mechanical ventilation, producing periods of constant pressure, have been applied to minimize motion artefacts and density changes caused by breathing (Schuster et al, 2003; Farncombe, 2008).

For prolonged imaging, X-ray dosages must be limited so that the lethal dose is not reached when performing longitudinal studies. In mice a radiation dose of approximately 5.0 to 7.6 Grays (one Gray (Gy) equals 1 joule of radiation energy per 1kg of body mass) will kill 50% of exposed mice in 30 days ($LD_{50/30}$) (Ford et al, 2003). Thus, the length of each scan and the number of repeat samplings must be considered in order to keep the total X-ray dose under lethal levels. Exposed animals take time to neutralize the damage after radiation exposure (0.25-0.5 Gy/day for mice when exposed daily); if there are multiple repeat CTs, damage from radiation doses could accumulate to lethal levels (Ford et al, 2003).

1.2 Asthma

1.2.1 Clinical Presentation

Asthma is an inflammatory disease of the airways which is defined by physiological changes including reversible obstruction, inflammation and airway hyperresponsiveness (AHR) (GINA, 2009). Remodelling of the airways is defined by a number of structural changes that include smooth muscle hypertrophy, epithelial and subepithelial fibrosis, vascularisation, and goblet cell hyperplasia, and is also a characteristic of asthma (Bogaert et al, 2009). These pathologies

are believed to result from a loss of tolerance to certain aeroallergens, in association with chronic or intermittent exposure over an extended period of time (Nials and Uddin, 2008). The extent of asthma severity ranges from mild to severe. In severe asthma some patients show persistent symptoms, and possess neutrophilia and airflow restriction (Auffray et al, 2010). This variability of the disease is likely due to a heterogeneous combination of both environmental and genetic factors (Fahy, 2008; Bogaert et al, 2009). Clinically, a non-invasive pulmonary function test is used to assess AHR using a non-specific cholinergic agonist which is typically methacholine (GINA, 2009). A diagnosis of asthma is made if there is a reduction ≥ 20 % forced expiratory volume in 1 second (FEV_1) after inhaled methacholine (≤ 8 mg/ml) (Sont et al, 1999).

1.2.2 Murine Asthma Models

Asthma is not a naturally occurring disease in mice, thus various protocols have been produced to stimulate an asthma-like response (Nials and Uddin, 2008). Either transgenic animals over-expressing various inflammatory mediators can be used, or allergen is delivered to mice to create an immune response (Fulkerson et al, 2005). Allergen induced asthma models are believed to be more clinically relevant to the induction of asthma (Fulkerson et al, 2005). Previously, ovalbumin (OVA) was the most commonly employed allergen; however, in some cases animals have developed tolerance to OVA (Johnson et al, 2004). The use of house dust mite (HDM) has been found to be more successful than OVA at

recreating aspects found in human asthma producing a model with prolonged AHR, airway remodelling, and eosinophilic inflammation (Johnson et al, 2004).

1.2.2.1 Allergen Induced Murine Asthma

To produce asthma-like symptoms in mice, first there has to be an initial period of sensitization, during which allergen is administered to the animal (either as an aerosol or injected) (Nials and Uddin, 2008). The length of sensitization time varies with the model. For aeroallergens (such as HDM) after a 7-10 day exposure period the animal is responsive to the allergen; there is peribronchial, perivascular and parenchymal inflammation (with eosinophilia); and increased airway resistance following a methacholine challenge due to AHR (Johnson, et al, 2004; Nials and Uddin, 2008). Intermittent, exposure to the allergen over an extended period of time (5-8 weeks after initial delivery) has been shown to produce airway remodelling in addition to chronic eosinophilic inflammation, and AHR (Johnson et al, 2004; Nials and Uddin, 2008; Southam et al, 2008). Termination of allergen exposure results in an eventual resolution of lung inflammation, but airway remodelling persists (Johnson et al, 2004). Therefore, chronic exposure to HDM is thought to be more relevant to human asthma than the acute exposure model since it enables the study of structural airway changes and mechanisms of AHR (Fulkerson, et al. 2005; Auffray, 2010). However, acute models are still useful for studying initial disease progression (Fulkerson, et al. 2005).

1.3 Pulmonary Fibrosis

1.3.1 Clinical Presentation

Pulmonary fibrosis (PF) is a progressive lung disease which is characterized by the increased production of fibrotic extracellular matrix (increasing collagen deposition) in the airways and parenchyma (Gross and Hunninghake, 2001). As the disease progresses throughout the parenchyma it leads to decreased lung compliance and gas exchange, eventually resulting in death (Kolb et al, 2002). The exact causes of disease initiation are not known, but it may occur in response to an inflammatory assault from an acute or chronic lung injury, or there can be no apparent cause at all, as seen in idiopathic pulmonary fibrosis (Sime et al, 1997). Some of the important contributors are believed to be inflammation, growth factors released from macrophages, and defects in extracellular matrix homeostasis (Brass et al, 2007).

PF is commonly diagnosed using physiological measurements such as pulmonary function tests in combination with visual radiological assessment (X-ray or high resolution CT (HRCT)) (Ask et al, 2008; Best et al, 2008). Histological changes in the alveoli and airways, which include honeycombing, increased fibrotic deposition and inflammation can be identified using HRCT. This is performed by radiologists who measure the area of lung occupied by regions of honeycombing, consolidation, hazy opaque regions (termed ground glass opacity), and abnormal reticular changes (Sverzellati et al, 2007). This

established visual scoring method is commonly employed for diagnosis and disease staging to predict mortality.

The use of quantitative CT analysis is being examined in patients with PF to assess its usefulness for describing disease progression and as a predictor of mortality; however, research is in the early stages of development (Best et al, 2003; Sverzellati et al, 2007; Best et al, 2008). Unlike COPD, which expresses increased regions of low attenuation, diseases such as pulmonary fibrosis have inflammation and fibrotic deposition present in the lungs which increase regions of attenuation, in addition to emphysematous regions, making it more difficult to quantify. Thus, in addition to using averaged data such as MLA, which might not be able to detect regions possessing both fibrosis and emphysema, analyses of the histogram shape assessing kurtosis and skewness have been used (Best et al, 2003; Lynch, 2007; Best et al, 2008).

1.3.2 Murine Models of Pulmonary Fibrosis

Animal models of PF have been used to explore early development of the disease since clinical presentation does not usually occur until later stages of disease progression. They are also used to better understand the pathological processes involved. (Brass et al, 2007). Many different models have been created using asbestos, irradiation, bleomycin, and more recently the transforming growth factor-β (TGF-β) and IL-1β (Kolb et al, 2001; Moore and

Hogaboam, 2008). The bleomycin model is the most commonly used; however, it has been shown to be limited for studying therapeutic drugs since fibrosis naturally decreases over time (Moore and Hogaboam, 2008). The TGF-β1 model has been shown to create a robust PF model which produced fibrosis with minimal inflammation. Transitory overexpression of TGF-β1in the respiratory epithelium in animals is achieved by insertion of the TGF-β1 gene using an adenoviral vector (AdTGF-β1) (Sime et al, 1997). The use of TGF-β1 for the creation of PF in animal is a relevant model because PF is associated with a number of cytokines including, TGF- β, which promote an accumulation and increased production of extracellular matrix protein such as collagen. TGF-β1 (one of the TGF- β isoforms) has been found to be involved in the production of pulmonary fibrosis in both humans and animal models (Warshamana et al, 2002). However, pulmonary fibrosis in humans generally progresses as a region of fibrosis which eventually spreads throughout the lungs producing a heterogeneous pattern of pathology (Moore and Hogaboam, 2008). Murine models of pulmonary fibrosis are generally created by an intratracheal delivery of either the adenovirus expressing active TGF-β1 or some other substance. This produces regional development of fibrosis which is initially more pronounced around the airways (Washamana et al, 2002).

1.3.3 Adenovirus vectors

The adenovirus is used in animal research to insert genetic material into cells preferentially targeting the respiratory epithelium. The virus infects a cell by first binding specific receptors (eg. Coxsackie adenovirus receptor (CAR) or integrin) which promote its internalization into the host cell, following which the virus is uncoated and eventually the viral DNA enters the nucleus (Einfeld et al, 2001). The viral DNA is then transcribed and translated using replication factors from the host cell (Einfeld et al, 2001). In adenoviral vectors the DNA containing the viral genome is mutated to prevent viral replication and a genetic sequence of interest is incorporated into the viral DNA to produce a recombinant plasmid (Sime et al, 1997). Following infection of the viral vector, host cells will express the factor transcribed by the inserted gene which will continue to be transcribed within the cell until its death. At this point gene expression will be halted since the inserted DNA is not replicated during cell division. The adenovirus vector is ideal since it has low rates of genetic recombination within the virus as well as low rates of integration with the host DNA. Thus, its genome will generally remain intact during creation of the adenovirus vector and within the host cell (Graham & Prevec, 1991; Xing et al, 1994).

1.3.4 Pathological Progression of PF in Mice after Delivery of adTGFβ1

The adenovirus constructed with a gene producing active TGF-β1in the recombinant DNA plasmid (adTGF-β1) has been employed to cause an over

expression of active TGF-β1(Sime et al, 1997). The virus infects the cells and inserts TGF-β1-containing plasmids. Replication occurs within the cells resulting in increased levels of TGF-β1expression. Direct delivery of adTGF-β1 to the lungs of rats has been shown to cause a transient over expression of active TGF-β1 measured in the bronchoalveolar lavage fluid (Sime et al, 1997). Sime and colleagues demonstrated that following intratracheal delivery of adTGF-β1 to rats, activeTGF-β1 levels peak at 7 days and are not statistically different after 2 weeks compared to animals receiving the control virus (Sime et al, 1997). There is also an associated period of peribronchial and perivascular inflammation (which is mainly monocytes) occurring 3 days after, decreasing by 7 days, and mostly resolved by 2 weeks. One week after delivery of the vector, fibrotic regions were noted around the airways in the parenchyma. At 3 and 9 weeks post instillation, collagen deposition was significantly increased (determined by measuring hydroxyproline content) compared to controls (Sime et al, 1997). Using a slightly different adTGF-β1viral vector, Warshamana, and colleagues, assessed pathological progression using various doses of adTGF-β1(10^6-10^9pfu) in C57BL/6 mice (Warshamana et al, 2002). They found that the temporal presentation of inflammation and the extent of fibrosis is dose dependant. In addition, animals receiving higher doses ($5X10^7$pfu) had persistent inflammation (macrophages) present over the examined 28 day period (Warshamana et al, 2002).

1.4 LPS Induced Neutrophilic Inflammation

1.4.1 Clinical Relevance of the Experimental Model

Lipopolysaccharide (LPS) is found in the outer membrane of gram negative bacteria. For laboratory use it has been purified to induce neutrophilic inflammation in animals without the associated infection (Galani et al, 2010). Administration of LPS directly to the lungs or systemically in rats and mice has been used to replicate acute lung injury (ALI) or its more severe form, acute respiratory distress syndrome (ARDS), which occurs in humans (Langheinrich et al, 2004; Alm et al, 2010).

ALI/ARDS is characterized by pulmonary edema and acute inflammation with neutrophilia, causing the alveoli to be filled with fluid which leads to poor gas exchange. This is caused by an increase in the permeability of the epithelium and vasculature which leads to edema in the lungs. If inflammation persists past two weeks, deposition of collagen and alterations of lung structure will start to occur (Galani et al, 2010). ALI/ARDS can occur due to various insults, both directly in the lungs (eg. pneumonia or aspiration of gastric juices) and systemically (eg. shock or sepsis). ALI/ARDS is usually diagnosed with radiological assessment (X-ray or CT) and by measuring blood gases (eg. PaO_2/fraction of inspired oxygen (FIO_2)) (Galani et al, 2010).

1.4.2 Murine Models of LPS Induced Neutrophilic Inflammation

An acute delivery of isolated LPS has been shown to stimulate a spontaneous and short lived immune response leading to inflammation characterized by pulmonary edema, neutrophilia, increased protein infiltration and an increase in levels of chemotactic factors in mice and rats (Alm et al, 2010). Bozinovski and colleagues found after delivering LPS to the lungs of BALB/c mice (10 µg /mouse) neutrophils were significantly higher than the control group at 6 hours with cell counts peaking at 24 hours and resolving after 3 days (Bozinovski et al, 2004). Thus, using LPS to initiate an inflammatory response makes it possible to study temporal and regional pathophysiological changes following the LPS challenge without biosafety concerns or worsening conditions due to prolonged infection.

1.5 Current State of the Art Applications of Micro-CT in Mouse Models of Asthma, Pulmonary Fibrosis and LPS induced Neutrophilic inflammation

To date, applications of micro-CT have been employed in models of LPS induced ALI, pulmonary fibrosis and asthma in rats (Langheinrich et al, 2004; Ask et al, 2008; Jobse et al, 2009), and pulmonary fibrosis and asthma models in mice (Lederlin et al, 2010; Cavanaugh et al, 2006; Lee et al, 2008; Rodt et al 2010). Both visual and quantitative-CT were applied to describe the presence of lung pathologies compared to control animals and have also been used to assess longitudinal progression in disease models.

Due to the limited resolution capabilities of micro-CT visual interpretation of images for preclinical studies generally does not allow differentiation between pathologies. Yet, visual interpretation still can be used to describe pathological changes from the normal lung. This was demonstrated by Rodt and colleagues who assessed lung consolidations in mice models of TGFβ-1 induced pulmonary fibrosis (Rodt et al, 2010). However, with improvements in imaging resolution (with reported voxel sizes of 10 μm) some papers have attempted to describe visual pathological changes from micro-CT images (Langheinrich et al, 2004; Lee et al, 2008). Lee and colleagues took sequential micro-CT images of mice (reconstructed to a voxel size of 35 μm) after exposing them to bleomycin to induce pulmonary fibrosis. Two experienced radiologists were then able to characterize clinical outcomes in the micro-CT images, including ground-glass opacity, consolidation, honeycombing, parenchymal lines and peripheral bronchial dilation to describe the extent of fibrosis and inflammation (Lee et al, 2008). To date, there are no other similar studies in the literature, likely because Lee and colleagues used image resolutions not available in many of the micro-CTs employed by most researchers. Furthermore, many studies hope to achieve a non-biased measurement of pathologies using micro-CT and visual assessment of images will have a certain degree of observer-induced variability. Thus, for pre-clinical analysis of pathologies in disease models, micro-CT densitometry is more frequently used.

1.5.1 Current applications of quantitative micro-CT in mouse models of asthma or pulmonary fibrosis

From the literature examining the use of micro-CT densitometry to identify pathologies in mice there exists one paper on murine models of asthma (Lederlin et al, 2010), and two papers on murine models of pulmonary fibrosis (with only one assessing PF initiated by TGF-β1 adenovirus vector) (Cavanaugh et al, 2006; Rodt et al 2010). Previous studies in rats have assessed changes in semi-automated lung segmentations in rat models of both pulmonary fibrosis and asthma (Ask et al, 2008; Jobse et al, 2009). Using this method they were able to detect the presence of pathologies (Ask et al, 2008; Jobse et al, 2009). Applying semi-automated lung segmentations that rely on density thresholds (eg. a range of -1000 to -200 HU) to isolate the lung becomes difficult in the presence of any pathology that increases lung density (eg ~0 HU due to inflammation or fibrosis). In mice it is even more difficult since all work is done on a smaller scale. Distal mouse airways may be described by a single voxel so a density increase within this voxel could halt the region growing algorithm and exclude the rest of the lung attached to the airway. To compensate for this limitation indirect and regional measurements of lung density changes have been employed (Cavanaugh et al, 2006; Rodt et al, 2010; Lederlin et al, 2010).

In the asthma mouse model, airway remodelling following chronic administration of OVA was measured at a single time point using an airway segmentation method. With this technique Lederlin and colleagues were able to

show that regional increases in airway density can be measured in OVA exposed mice compared to controls (Lederlin et al, 2010). In micro-CT densitometry studies of models of pulmonary fibrosis murine models induced by bleomycin (Cavanaugh et al, 2006) and the TGFβ-1 adenovirus vector (Rodt et al, 2010) have been employed. Due to lung segmentation limitations an indirect measurement of aeration to quantify the extent of fibrosis was used by Rodt and colleagues (Rodt et al, 2010) and a similar lung volume measurement was performed by Cavanaugh and colleagues (Cavanaugh et al, 2006). Both studies were able to identify the presence of pathologies based on micro-CT densitometry and the outcomes were validated by terminal histological procedures.

1.6 Purpose of Thesis

Quantitative micro-CT has been shown to be useful to determine the presence of pathologies in murine pulmonary disease models; however, it is unknown whether the pathological process can be characterised by quantitative CT alone. Using established mouse models of HDM induced asthma, TGF-β1 induced PF and LPS induced neutrophilic inflammation this thesis examines if CT densitometry can be used to distinguish between healthy and diseased lungs, and different pathophysiological processes.

1.7 Hypotheses

Animal models of pulmonary fibrosis, neutrophilic inflammation and acute and chronic asthma will express denser lung profiles compared to the associated control groups due to the presence of fibrotic tissues, inflammation and airway remodelling.

1. These different pathologies (eosinophilic inflammation, airway remodelling, fibrosis, and neutrophilic inflammation) can be distinguished from controls based on CT densitometry
2. Disease progression and resolution within each model can be quantified using CT densitometry
3. Eosinophilic inflammation, airway remodelling, fibrosis, and neutrophilic inflammation will each have a unique density profile

1.8 Specific Objectives

The first objective was to create a lung segmentation protocol which could be applied to all three disease models, to distinguish the presence of pathologies in the lung. Note: Due to the increased density of the lungs, full lung segmentations were not able to be performed in all the models. Since the asthma, PF and LPS model expressed peribronchial pathologies an airway segmentation method was created to assess a 3D region surrounding the airway.

The second objective was to determine if CT densitometry can differentiate between different pathophysiological processes, including inflammation, remodelling and fibrosis, using well established animal models of disease. Histological and physiological (for the asthma models only) data were used to confirm the successful generation of the models.

Chapter 2:

2 MATERIALS & METHODS

2.1 Materials

2.1.1 Solution Preparations

2.1.1.1 House Dust Mite (HDM)

The HDM *Dermatophagoides pteronyssinus* extract (Greer Laboratories, Lenoir, NC, USA) was suspended in phosphate buffered saline (PBS) producing doses of 15 µg (measurement based on protein content) of HDM in 30 µl of PBS. The solution was prepared in advance, and kept at -70°C until needed. PBS (30µl) served as a vehicle control.

2.1.1.2 Lipopolysaccharide (LPS)

LPS was derived from Klebsiella pneumonia (Sigma-Aldrich Canada Ltd, Oakville, ON, Canada) in a 500 µg/ml solution. It was kept frozen at -20°C until used. On the day of the experiment it was diluted in PBS to achieve a dose of 5 µg of LPS per 30 µl volume, which was kept on ice until delivery. PBS (30 µl) served as vehicle control.

2.1.1.3 Transforming Growth Factor Beta Adenovirus Vector (adTGF-β1)

TGF-β1 was delivered in a non-replicating recombinant adenovirus vector carrying an active TGF-β1 (adTGF-β1) porcine derived gene. The adenovirus vector was prepared using the method previously described by Sime,P.J. and

colleagues (Sime et al, 1997). We received the adTGF-β1from Dr. Jack Gauldie's laboratory as titre containing $1.3X10^{11}$plaque forming units per ml (pfu/ml) and $2.0X10^{11}$pfu/ml dosing for the adenovirus vector (adDL-70), which contains the adenovirus vector without the TGF-β1gene and served as control. These were both kept at -70°C until ~1 hr before delivery. Each animal received $2.0X10^{8}$ pfu of adTGF-β1 or adDL-70 in a 50 µl volume suspended in PBS. The solutions were kept on ice until delivery.

2.2 Animals

All animals were supplied by Charles River Laboratories (Saint-Constant, QC, Canada). Female BALB/c mice aged 10 weeks were used for the acute (n = 72) and chronic asthma models (n = 72), and the LPS inflammation model (n = 26). Female BALB/c mice were used since they have been shown to produce increased allergic response compared to males (Melgert et al, 2005). C57BL/6 mice were not used in the asthma model as we wanted to assess hyperresponsiveness associated with HDM sensitization and it has been previously shown that C57BL/6 mice are hyporesponsive following methacholine challenge in an acute exposure protocol (Gueders et al, 2009). Female C57BL/6 mice aged 10 weeks were used for the pulmonary fibrosis model since BALB/c mice have been found to be "fibrosis-resistant" (Kolb, M. et al, 2002). All mice were housed in a Level 2 biohazard clean room which was under a 12 hr light/dark cycle and kept at 25°C. All experiments were approved by the Animal

Research Ethics Board of McMaster University and conducted in accordance to CCAC guidelines.

2.3 Animal Models

2.3.1 Asthma

Acute asthma model was created by a method previously published by Hirota and colleagues (Hirota et al, 2010) and the chronic asthma and recovery models were created similar to a method previously published by Southam and colleagues (Southam et al, 2008). HDM extract was delivered intranasally (IN) using a pipette. For delivery the mice were anesthetised using 2.5% isoflurane with 1.5 l/min oxygen. HDM (15 µg based on protein content) was administered suspended in 30 µl of PBS. The control group received an equal volume of PBS. Following IN delivery, the mice were held vertically (head up) until they recovered from anaesthesia.

The period of HDM delivery varied depending on the model (**Figure 3**). The acute HDM exposure group (HDMA) was sensitized to HDM (or vehicle) daily for 2 weeks on a 5 day treatment/weekends off schedule. Following the initial 2 week sensitization the chronic HDM exposure (HDME) and recovery following HDM exposure (HDMR) groups, received an additional 6 weeks of HDM delivery 3 days a week (alternating delivery every other day with weekends off). The HDMR

groups were housed for an additional 4 weeks without further HDM exposure to allow inflammation to subside.

The HDMA, HDME and HDMR groups were imaged at day 15, 57 and 85 respectively after commencement of HDM sensitization. For the HDMA and HDME groups HDM was delivered IN 24 hr before imaging. The following day (day 16, 58 or 86) physiology measurements were performed. Animals were euthanized by exsanguination via cardiac puncture and histological procedures were performed (**Figure 3**).

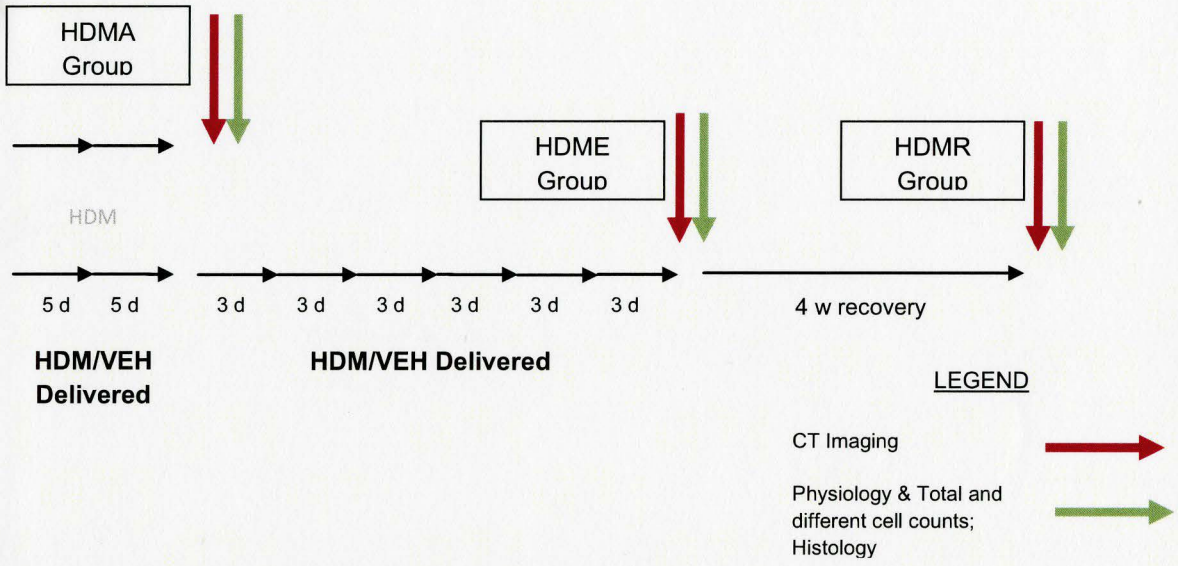

Figure 3. Acute and chronic allergen experimental protocol. The acute group (HDMA) outcome measures occurred right after the period of HDM sensitization, which lasted the first two weeks (with weekends off). For the chronic groups (HDME and HMDR) a continued weekly exposure to HDM was sustained for another 6 weeks. HDME outcomes were at the end of this period. HDMR groups were housed for another 4 weeks without further HDM exposure. Red arrows indicate dates of CT imaging and the green indicate when physiological, BAL and histological data were obtained.

2.3.2 TGF-β1 Adenovirus Induced Pulmonary Fibrosis

Using a method previously described by Kolb and colleagues the adTGF-β1 was delivered intratracheally (IT) to three different groups of animals (termed group 1, 2, 3) (Kolb et al, 2002). Groups 1 & 2 received the dose by the same IT method and group 3 by a slightly altered IT technique. The vehicle group received the vector (adDL-70) by the same method as groups 1 & 2.

For group 1 and 2 the mice were anesthetised using ketamine (150 mg/kg)/xylazine (10 mg/kg) injected intraperitoneally (IP). Each animal was suspended by their top incisors on a mounting board (set at ~60°) and held in place with surgical tape (Micropore™3M™). The tongue was drawn to the side with forceps and trachea was visualized using an otoscope (Welch Allyn Canada, Mississauga, ON, Canada). A 20 gauge plastic catheter tip (BD Insyte, Sandy, UT, USA) was inserted down the trachea with the assistance of an endotracheal tube (ET) guide (Mouse ET Tube guide, Hallowell EMC, Pittsfield, MA, USA). The ET guide was removed and a pipette tip containing water was inserted in the catheter tube to visualize if it was properly down the trachea (a positive response was the movement of the water indicating in/exhalation). Once the tube was confirmed to be down the trachea a gel-loading pipette tip attached to a pipette, containing either the adTGF-β1or adDL-70, was placed down the tube. The $2X10^8$ pfu/animal dose was delivered in two 25 µl aliquots, removing the loading-tip in between deliveries. This was followed by a delivery of 50 µl air down the plastic catheter tip using the pipette. Mice were injected with 1 ml of

subcutaneous saline1 hr after delivery to prevent dehydration, ocular lubricant (Lacri-lube, Allergan, Markham, ON, Canada) was placed on their eyes and they were monitored until they recovered from the anaesthesia.

For group 3, mice were anesthetised using 2.5% isoflurane with 1.5 l/min oxygen. They were placed on a mounting board, the trachea was visualized with an otoscope (same as previously mentioned), and the adTGF-β1 was delivered intratracheally (IT) by pipette as one 50 µl dose using a standard pipette tip. Post-delivery monitoring was the same as described above.

Following administration of the adenovirus, all cages were kept half on a heating pad for 7 days; the animals were weighed daily, monitored and given a subcutaneous injection of 1 ml of saline twice daily for 10 days. At 14, 21, and 28 days following adenovirus administration the mice were imaged by CT then the following day they were euthanized by exsanguination from the descending aorta and BAL and histological procedures were performed (at 15, 22, and 29 days) (**Figure 4**). The time points were chosen to assess if it was possible to measure differences in fibrosis over time. Previous studies have found increased collagen deposition up to 64 days after delivery in rats (Sime et al, 1997).

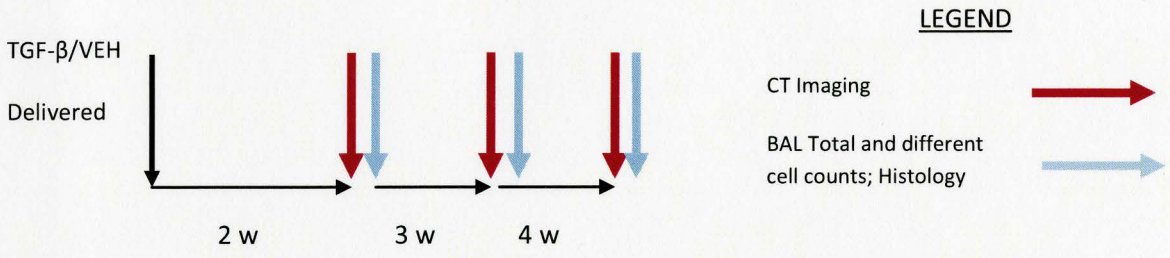

Figure 4. TGF-β1 induced pulmonary fibrosis experimental protocol. The adTGF-β1 and control (adDL-70) were delivered IT as a single exposure. Red lines indicate dates of CT imaging and the blue indicate when BAL and histological data were obtained.

2.3.3 LPS Induced Neutrophilic Inflammation

Using a method similar to that previously described by Bozinovski and colleagues the LPS solution was administered IN as a single dose of 5 μg of LPS in 30 μl of PBS or an equivalent volume of PBS (vehicle control) after the mice were anesthetized (2.5% isoflurane with 1.5 l/min oxygen) (Bozinovski et al, 2004). Following delivery the animals were imaged at 7, 24 hours or 14 days post instillation. These time points were chosen since previous studies have reported that inflammation (measured by total cell counts) peaks at 24 hrs after LPS delivery in BALB/c mice (Alm et al, 2010) and at 14 days following administration of LPS inflammation should be completely resolved (Santos et al, 2006). Following imaging the animals were euthanized by exsanguination from the descending aorta (**Figure 5**) and histological and BAL procedures were performed.

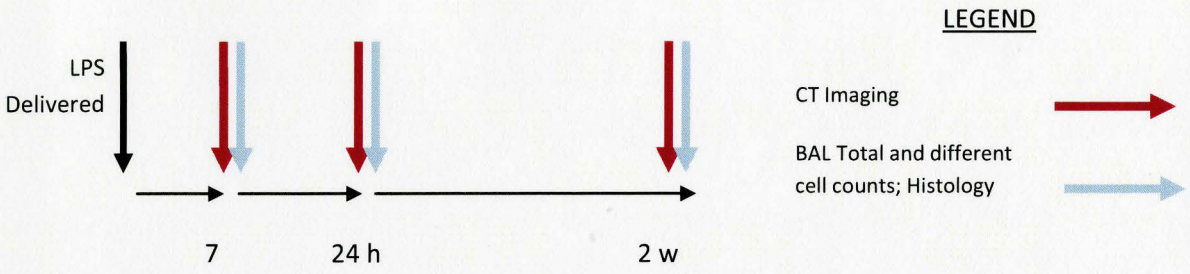

Figure 5. LPS induced neutrophilic inflammation experimental protocol. LPS and the PBS vehicle were delivered IN as a single exposure. Red lines indicate dates of CT imaging and the blue indicate when BAL and histological data were obtained.

2.4 CT Imaging

CT images were acquired using the CT portion of a SPECT/CT (X-SPECT, Gamma Medica-Ideas, Northridge, CA, USA) in the McMaster Centre for Pre-Clinical and Translational Imaging. Images were acquired using two rotations of 1024 projection each at a voltage of 75 kVp and a current of 220 μA. Animals were freely breathing in HEPA-filter fitted animal holding tubes under anaesthesia with 1.5% isoflurane using 1.0 l/min oxygen flow. Data was reconstructed using a Feldkamp cone beam back projection algorithm into 512x512x512 matrix (115 mm^3 voxels). Each animal was imaged with a water tube which was used as a standard to convert the CT units into Hounsfeld Units (HU) along with an ROI of the surrounding air, used as the air standard. The resulting data then expresses voxels possessing densities in HU where any voxel with the density of air will be -1000 HU and voxels with the density of water will be 0 HU.

Respiratory gating (RespGate Software, Hamilton, ON) was applied to the reconstructed micro-CT images and divided into three different gates: Summed, which contains all inspiratory and expiratory projections; Gate 1, which uses projections acquired on the expiratory cycle; and Gate 4, which contain projections on the inspiratory cycle (Farncombe, 2008). Data from Gate 1 was used to control for density changes due to altered breathing (affecting the summed data). Before segmenting the data a Gaussian filter, using a sigma value of one, was used to improve visual resolution of the image using Amira 5.2.1 software (Visage Imaging, Andover, MA, USA). This filter works by averaging the HUs between neighbouring voxels.

2.5 Lung Segmentation

Typically lung segmentations are used in clinical densitometry studies, however, this would be done using a region growth algorithm which segments the lungs based on a density range; for example -990 to -100 HU is a range that was previously reported for segmenting mouse lungs (Guerrero, et al, 2007). This methodology could not be used in the present study because density changes in the lung, due to an increase in fluid or extracellular matrix deposition (~0 HU), in the three disease models would be excluded from the lung segmentation. Manual lung segmentation is extremely time-consuming and differentiating lung tissue from other surrounding structures like the heart, blood vessels and skeletal muscle can be difficult and subjective. Due to these limitations and since asthma,

PF and LPS models have been shown to express peribronchial pathologies, for this thesis a new airway segmentation method was developed that selects an area around the large airways.

To isolate 3D regions of interest (ROI) in the lung micro-CT images were segmented and quantified using Amira 5.2.1 software (Visage Imaging, Andover, MA, USA). The region around the main bronchi was isolated from the rest of the lung (**Figure 6**). It was created using a uniform circular diameter (brush size 20, approximately 2.30 mm in diameter) and selecting around the large airway from rib 7 to rib 9, interpolating between ribs and going 23 slices down (2.65 mm in depth). This produces a volume of 11 µl which is ~9 % of the total lung air volume at expiration (lung air volume calculated as being around 126 µl - determined from baseline data). The densities of each of the voxels in the segmented regions were plotted as a total number of voxels in each 33 HU density bin. The brush size of 20 was chosen in order to include as much of the area surrounding the main bronchi without including other tissues such as the heart. At rib 7 there are two defined bronchi and it is just before the main bronchi bifurcate (or in some cases trifurcates). The main dorsal branch was chosen as the midpoint for the circular region and this was traced down to rib 9. Rib 9 was selected as the end point since it is the depth in which the main bronchi were still able to be visualized and thus confidently selected.

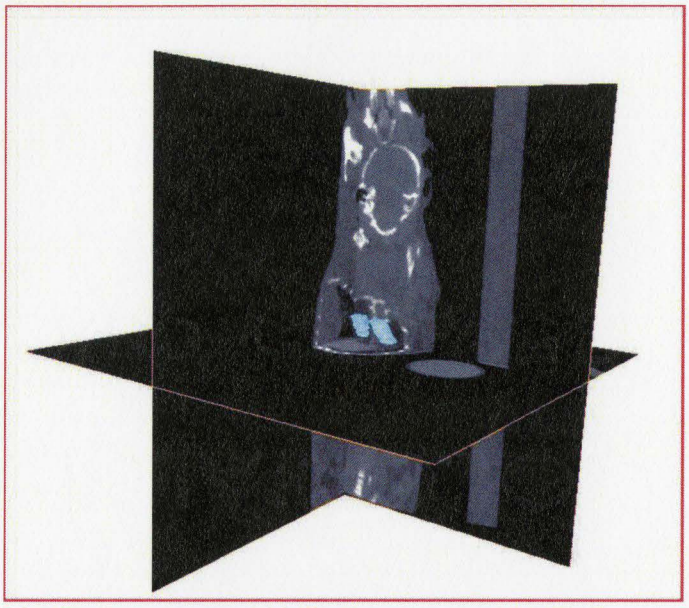

Figure 6. Large airway segmentation using Amira 5.2.1. The blue regions are an isosurface of the airway segmentations. Axial, sagittal and coronal sections of a micro-CT image from a control mouse were used to illustrate the location and relative size of the segmentation.

2.5.1 Airway Diameter

Since the airway segmentation method contains both surrounding tissues and the lumen the airway diameters were measured in the asthma, pulmonary fibrosis, and LPS models to determine if alterations in density could be contributed to changes in lumen size. Two measurements of lumen diameter (coronal and sagittal) were taken at rib 7, 8 and 9 in each animal and at each rib measurements were averaged. This was performed using the 3D measuring tool with Amira 5.2.1 software (Visage Imaging, Andover, MA, USA).

2.6 Physiology (Asthma Model Only)

2.6.1 Pressure Volume Analysis

At endpoint total lung resistance was measured using flexiVent v5.2 rodent ventilator (Scireq, Montreal, QC, Canada) at baseline (PBS alone) and after administering 5 increasing doses (3.1, 6.3, 12.5, 25, and 50 mg/ml diluted in PBS) of nebulized acetyl-β-methylcholine (Mch; Sigma-Aldrich).

Animals were anesthetised by an IP injection of xylazine (~30 mg/kg). Approximately 5 minutes following initiation of anaesthesia mice were inhibited from freely breathing via pancuronium bromide (20 mg/kg) delivered IP (Sandoz, QC, Canada) so the physiological measurements would not be affected by the animals own breathing pattern. A tracheotomy was performed and an 18 gauge tube was inserted and affixed with suture. The mouse was attached to the flexiVent v5.2 rodent ventilator and total lung resistance measurements were taken. The lung pressure was normalized before each Mch dose to 30 cmH_20 for approximately 6 seconds then ventilated for 30 seconds at each dose at a rate of 150 breaths/min. Total lung resistance was measured using a single compartment, standardized breathing signal that measures dynamic resistance (Leigh et al, 2002). This was then plotted as a resistance versus time plot and the slope was determined from Mch dose 3.1 to 25 mg/ml. The slope was used to determine airway reactivity (the steeper the slope the more reactive the airways are to the stimulus).

2.7 Inflammatory Cells

2.7.1 Bronchoalveolar Lavage (BAL), Total and Differential Cell Counts

At end point the animals were euthanized by exsanguination and bronchoalveolar lavage fluid (BALF) was extracted intratracheally (IT) using two washes of 0.25 mL of PBS. This was done either through a 22 gauge needle fitted with PE50 polyethylene tubing (Becton Dickinson and Co., Mississauga, ON, Canada) for the LPS and PF model or through an 18 gauge endotracheal tube for the asthma models. The BALF was then kept on ice and centrifuged at 15,000 g for 10 min (Hermle model Z233M, Germany). The supernatant was extracted and stored at -25°C. The remaining cell pellet was resuspended in 150 µl of PBS and the total cells (TCC) were counted on a hemocytometer (Bright-Line, Horsham, USA) using either Turks (for the LPS and PF models) or Trypan Blue stain (for the asthma model) as a 1:1 stain to BALF ratio. Another 150 µl of PBS was added to the cell pellet and slides were prepared by centrifugation in a Shandon Cytopin3 (Shandon Inc., Pittsburgh, USA) at 9.6 X g for 2 min for the LPS and PF samples and in a Shandon Cytospin3 (Shandon Scientific Ltd., UK) for the asthma model samples in two steps. The slides for the asthma model were prepared for cell adhesion by first delivering 90 µl of PBS to the cassette and putting it in the Cytospin for 3 min at 300 rpm following which the cell suspension was added (90 µl) and spun for 5 min at 300 rpms. The slides were stained with either hematoxylin & eosin (H&E; for the LPS and PF models) or

Wright-Giemsa stain (for the asthma models). Differential cell counts (DCC) of BAL cells on the slides were performed counting up to 200 cells on the slide classifying neutrophils, eosinophils, lymphocytes, and macrophages based on visual histological morphology using an Olympus CX41 microscope (Markham, ON, Canda) (**Appendix**, **Figure 36** to**Figure** 38 for representative BALF slides).

2.8 Histology

2.8.1 Preparation of Slides

The lungs were removed and inflated under a constant pressure of 15 cmH_2O (for the asthma model) or 20 cmH_2O (for other models) and kept in 10% formalin for 24 hrs before being dehydrated in a graded ethanol series (in 50%, then 75% ethanol for 30 min each) samples were stored in 75% ethanol until they were embedded in paraffin. They were sectioned (3 μm thick) and stained with Hematoxylin and Eosin (H&E) to examine lung morphology as well as Picrosirius Red (PSR) for the PF group to stain for the presence of collagen. H&E stain is useful for describing normal cell morphology by staining acidic structures blue (Hematoxylin) and basic structures red (Eosin). Hematoxylin is a basic dye that reacts with acidic molecules such as nucleic acid (dying them blue), whereas Eosin is an acidic dye reacting with basic structures like collagen and muscle (dying them red). This enables the differentiation of structural elements in the tissues which are comprised of both basic and acidic molecules. (Wheat, Burkitt

& Daniels, 1987). PSR stain is useful for detecting the presence of collagen since the sulphonic acid groups in the PSR stain reacts with the basic groups of collagen. This stain is useful since it enhances the double refractory phenomenon of the collagen fibres, which can best be viewed under polarized light microscope (Junqueira, Bignolas & Brentani, 1979). Lung inflammation was assessed from H&E stained slides and characterized based on cellular lung infiltration. Airway remodelling was characterized from H&E stained slides as increased smooth muscle deposition and goblet cell hyperplasia. All practises were performed using standard techniques according to the ATS guidelines (Hsia et al, 2010).

2.9 Data Analysis

2.9.1 CT Image Analysis

The CT image is divided into many voxels each possessing an average measure of x-ray attenuation which is relative to tissue density. This attenuation value was then converted into Hounsfield Units (HU) based on standards of water (0 HU) and air (-1000 HU). The airway segmentation was applied to the CT and within the segmented region the frequency of voxels in the density interval of -1025 to 625 HU were determined. This interval was divided into 50 bins which were 33 HU in width. The data were plotted as voxel frequency at each density bin (**Figure 7**).

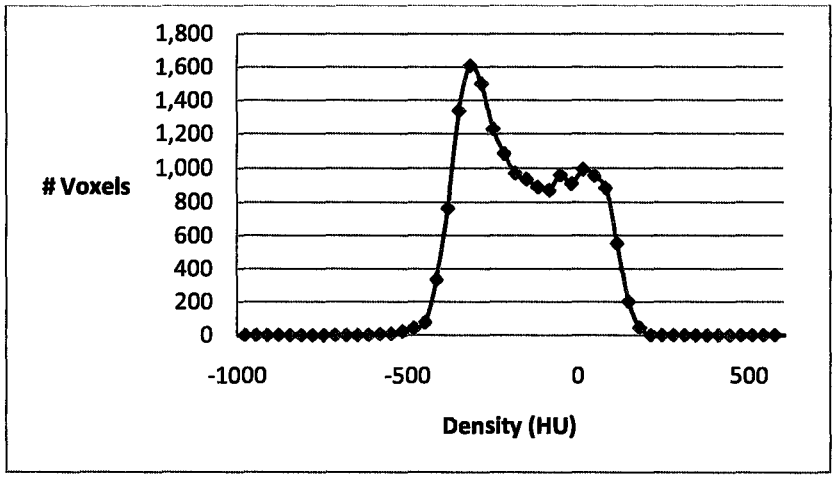

Figure 7. Representative plot of # voxels vs density from a mouse large airway segmentation. The plot shows the total number of voxels at each density bin around the large airways from rib 7 to 9.

2.9.2 Statistics

All data is expressed as mean ± SEM. SEM was used to regulate for variation in sample sizes between the groups. The analysis was performed on IBM SPSS Statistics 19. A p-value of 0.05 was deemed statistically significant.

2.9.2.1 CT Densitometry Statistics for Individual Disease Models

Differences in voxel frequency within each individual disease model (asthma, PF and LPS induced neutrophilic inflammation) were determined using a one way ANOVA. The goal of this analysis was to assess if statistical differences in voxel frequency existed at each density bin between the control groups, between exposure groups and controls, or between the exposure groups themselves. The parameters compared were:

1. The age-matched; vehicle-treated controls to themselves (**Table 2**)

2. The combined vehicle groups within each model to the exposure groups (**Table 3**)
3. The exposure groups in each disease model each other (**Table 4**)

For comparisons 1 and 3, if statistical significance was found a Tukey analysis was performed. Tukey post-hoc analysis assesses all possible pair-wise comparisons of the included data. In each model the controls were found to be no different from each other so the control data were grouped for parameter 2. A Dunnett's post hoc analysis was performed to determine if differences exist between the control group and each exposure group (**Table 3**). $P < 0.05$ was considered statistically significant.

Table 2. Parameter 1. Comparison of vehicle control groups

Disease Models	Groups Compared		
Asthma	VEH (acute asthma) vs. VEH (chronic asthma)	VEH (chronic asthma) vs. VEH (recovery asthma)	VEH (recovery) vs. VEH (acute asthma)
LPS	VEH (LPS 7h) vs. VEH (LPS 24h)	VEH (LPS 24h) vs. VEH (LPS 2w)	VEH (LPS 2w) vs. VEH (LPS 7h)
Pulmonary Fibrosis	VEH (PF 2w) vs. VEH (PF 3w)	VEH (PF 2w) vs. VEH (PF 4w)	VEH (PF 3w) vs. VEH (PF 4w)

Table 3. Parameter 2. Comparison of grouped vehicle data to exposure groups

Disease Models	Groups Compared		
Asthma	HDMA (acute asthma) vs. VEH-AVG	HDMA (chronic asthma) vs. VEH-AVG	HDME (recovery) vs. VEH-AVG
LPS	LPS 7h vs. VEH-AVG	LPS 24h vs. VEH-AVG	LPS 2w vs. VEH-AVG
Pulmonary Fibrosis	PF 2w vs. VEH-AVG	PF 3w vs. VEH-AVG	PF 4w vs. VEH-AVG

Table 4. Parameter 3. Comparison of exposure groups within models

Disease Models	Groups Compared		
Asthma	HDMA (acute asthma) vs. HDME (chronic asthma	HDMA (chronic asthma) vs. HDMR (recovery asthma)	HDME (recovery) vs. HDMR (acute asthma)
LPS	LPS 7h vs. LPS 24h	LPS 24h vs. LPS 2w	LPS 2w vs. LPS 7h
Pulmonary Fibrosis	PF 2w vs. PF 3w	PF 3w vs. PF 4w	PF 4w vs. PF 2w

2.9.3 CT Densitometry Statistics for Comparisons of Disease Models

Differences in voxel frequency were determined between the three disease models (asthma, PF and LPS induced neutrophilic inflammation) using a one way ANOVA examining frequencies at each bin over the interval of -1025 to 625 HU. The objective was to determine if there are statistical differences in voxel frequency at each bin between the all the vehicle groups or between the exposure groups in each disease model. The parameters compared were:

1. The vehicle groups of each model to assess if visible differences were apparent between control groups
2. All other disease models (exposure groups only) (**Table 5**)

For parameter 1, if statistical significance was found a Tukey post hoc analysis was applied to the data. For parameter 2, if statistical significance was found Dunnett's post hoc analysis was performed using the individual disease group as the control group and comparing it to the other exposure groups in the two other disease models (eg. HDMA was compared to all 3 exposure groups in the LPS models and time points in the PF models; see **Table 5**)

. This method of analysis was chosen to limit the number of hypotheses that were tested, preventing the comparison of the exposure groups within a disease model (ex. HDMA, HDME, and HDMR) to each other since they were previously assessed. $P < 0.05$ was considered statistically significant.

Table 5. Parameter 2. ANOVA Comparisons between disease groups. Arrows show comparison groups. Gray regions indicate groups that were not compared.

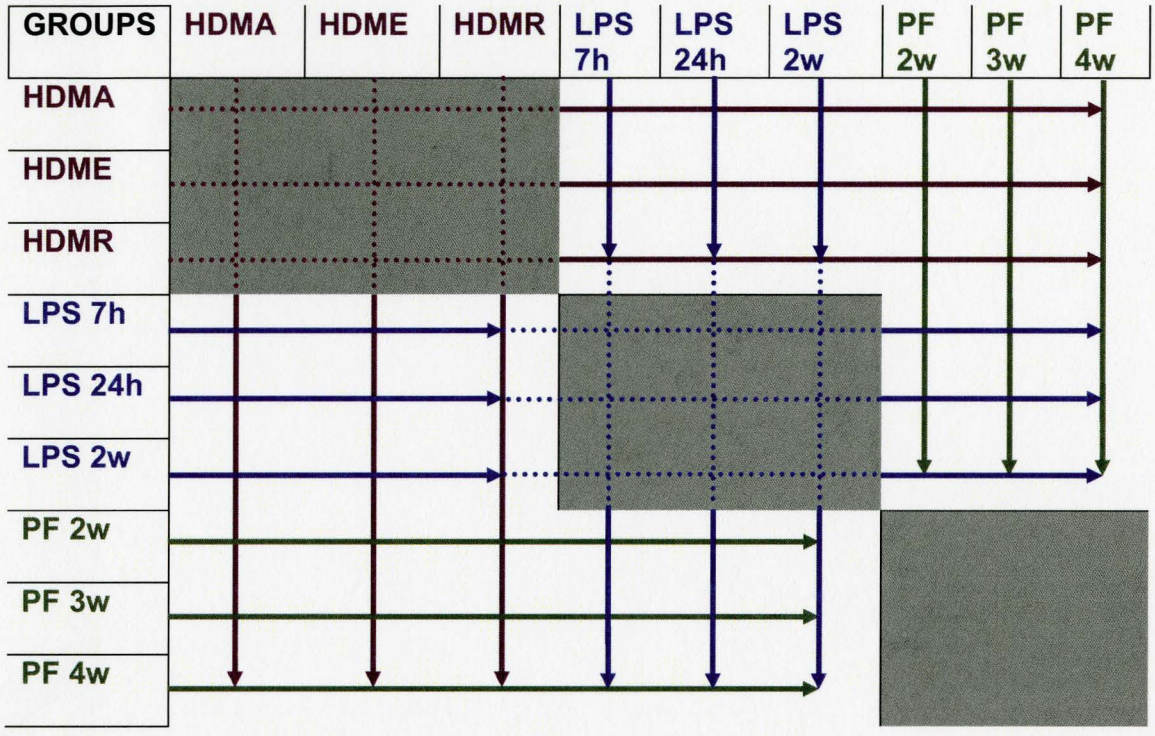

NOTE: Comparison groups found to be significantly different from each other on the y-axis had to span a region more than two bins in width (>66 HU wide) on the x-axis in order to be considered experimentally different. This criterion was made to account for horizontal variability in HUs which was measured in the standards of water and air, each possessing standard deviations of 100 and 50 HU, respectively.

2.9.4 BAL, TCC and DCC Statistics

The total cell counts and differential cell counts were analyzed using a one way ANOVA. The analysis was performed on each individual model (asthma, PF and LPS exposure) to determine if a difference existed between the total and differential cell counts between control groups, between the control and disease groups, and between disease groups. The parameters compared were:

1. The vehicle groups within each model
2. Each exposure group to its age-matched and vehicle-treated control
3. The exposure groups in each disease model to themselves

The parameters were collectively analyzed within each disease model. If statistical significance was found a Tukey's post hoc analysis was performed. Significance was determined to occur at $P < 0.05$.

2.9.5 Physiology Statistics (Asthma Model Only)

Unpaired t-test was performed on the slope from the resistance to dose plots from the dose of 3.1 to 25 mg/ml between the exposure groups and the controls, statistical significance was determined to occur at $P < 0.05$.

2.9.6 Airway Diameter

Differences between airway diameters of the controls and disease groups were analyzed using an unpaired t-test at each time point. Statistical significance was determined to occur at $P < 0.05$.

Chapter 3

3 RESULTS

In this section the results of each disease model are collectively presented. These include representative CT images, CT densitometry plots and histological data (and in the case of the asthma model, physiological data).

3.1 Asthma Model

3.1.1 Representative CT Images

In the asthma model increased areas of density were apparent around the airways in the HDMA, HDME, and HDMR groups (**Figure 8 B, D & E**) with notable increases seen in the HDME group (**Figure 8D**). Airway diameters at rib 7, 8, and 9, had no significant differences between the HDM exposed and the control animals (**Appendix, Figure 39 A-C**) except for the chronic asthma group which had a statistically larger airway diameter at rib 7 compared to the control group (**Appendix, Figure 39 B**).

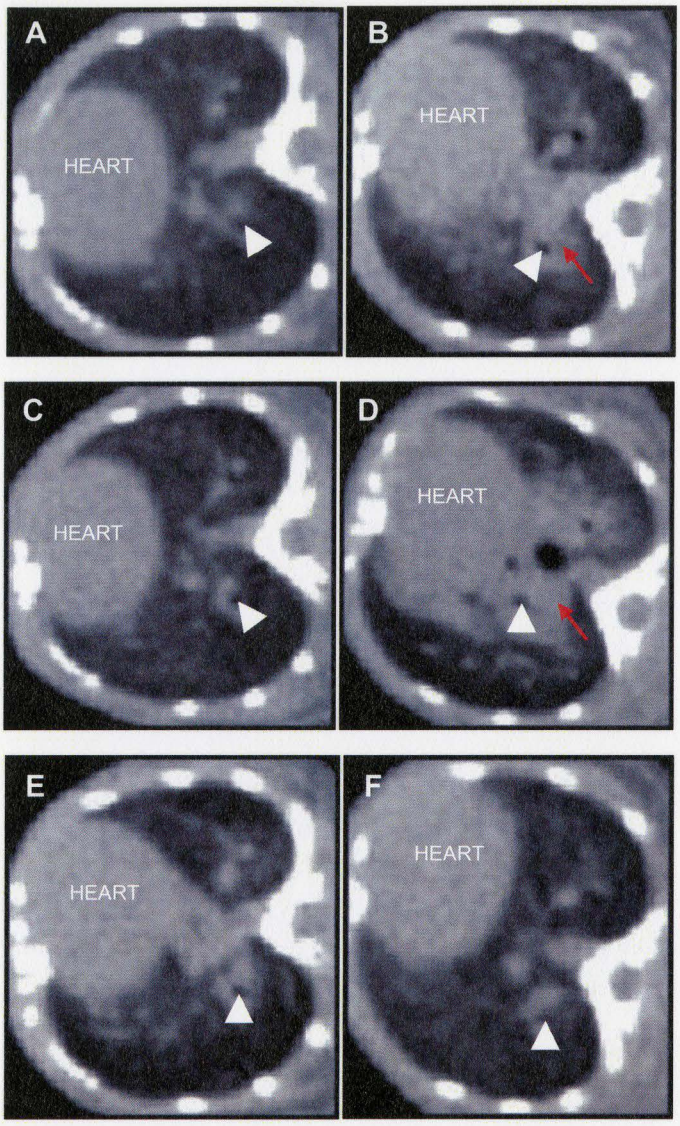

Figure 8. Representative axial CT images of the lungs in the asthma model and their age matched and vehicle treated controls. (A) control and (B) acute asthma, which should express peribronchial/perivascular inflammation; (C) control and (D) chronic asthma model, which should express peribronchial/perivascular inflammation and airway remodelling; (E) control and (F) recovery following chronic HDM delivery, which should express airway remodelling. White arrow indicates airway. Red arrows indicate high attenuation region around airways.

3.1.2 CT Densitometry

The plots from the large airway segmentations in the three different asthma exposure groups (HDMA, HDME, and HDMR) are different from the control group (VEH), with each asthma model group having an overall increase in voxel frequency in the highly dense region (~0 HU) on the plot (**Figure 9**). This shift can be illustrated by the location of the main peaks in each plot. The control lung had a large peak situated around -350 HU whereas the HDMR group had a main peak at -250 HU, and the HDMA and HDME groups both had a pronounced peaks at 15 HU and 50 HU respectively. Statistically significant differences were found between the control and HDMA (**Figure 10 A**), HDME (**Figure 10 B**), and HDMR groups (**Figure 10 C**) in two main regions ($P < 0.05$). All three exposure groups had regions that had significantly more voxels than the controls in the denser region (~-100 to 100 HU) ($P < 0.05$). This shift to the denser region in the disease plots produced significantly smaller voxel frequencies in less dense region (~-400 to -300 HU) in the exposure groups compared to the control group ($P < 0.05$). The results from the CT densitometry plots indicate that within the airway segmentations the exposure groups possess fewer voxels in the low density region and more voxels in the higher density region compared to controls. Over the measured density interval the controls for each asthma group had no regions which were statistically different from each other and therefore were grouped together (Figure not shown) ($P > 0.05$).

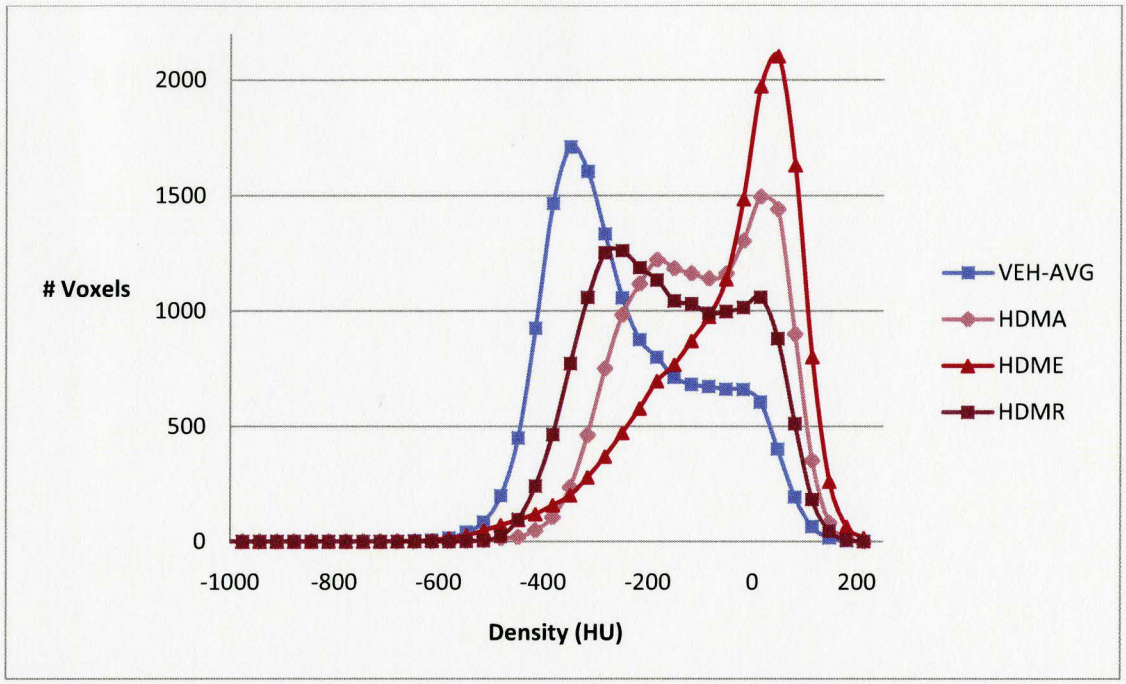

Figure 9. Density distribution around selected large airways in mouse asthma models. The plot contains acute (HDMA) and chronic HDM exposure (HDME) and recovery following chronic HDM exposure (HDMR) and the grouped control data (VEH-AVG).The age matched, vehicle treated controls (VEH-AVG) for each asthma model were combined as they were found to not be statistically different from each other.

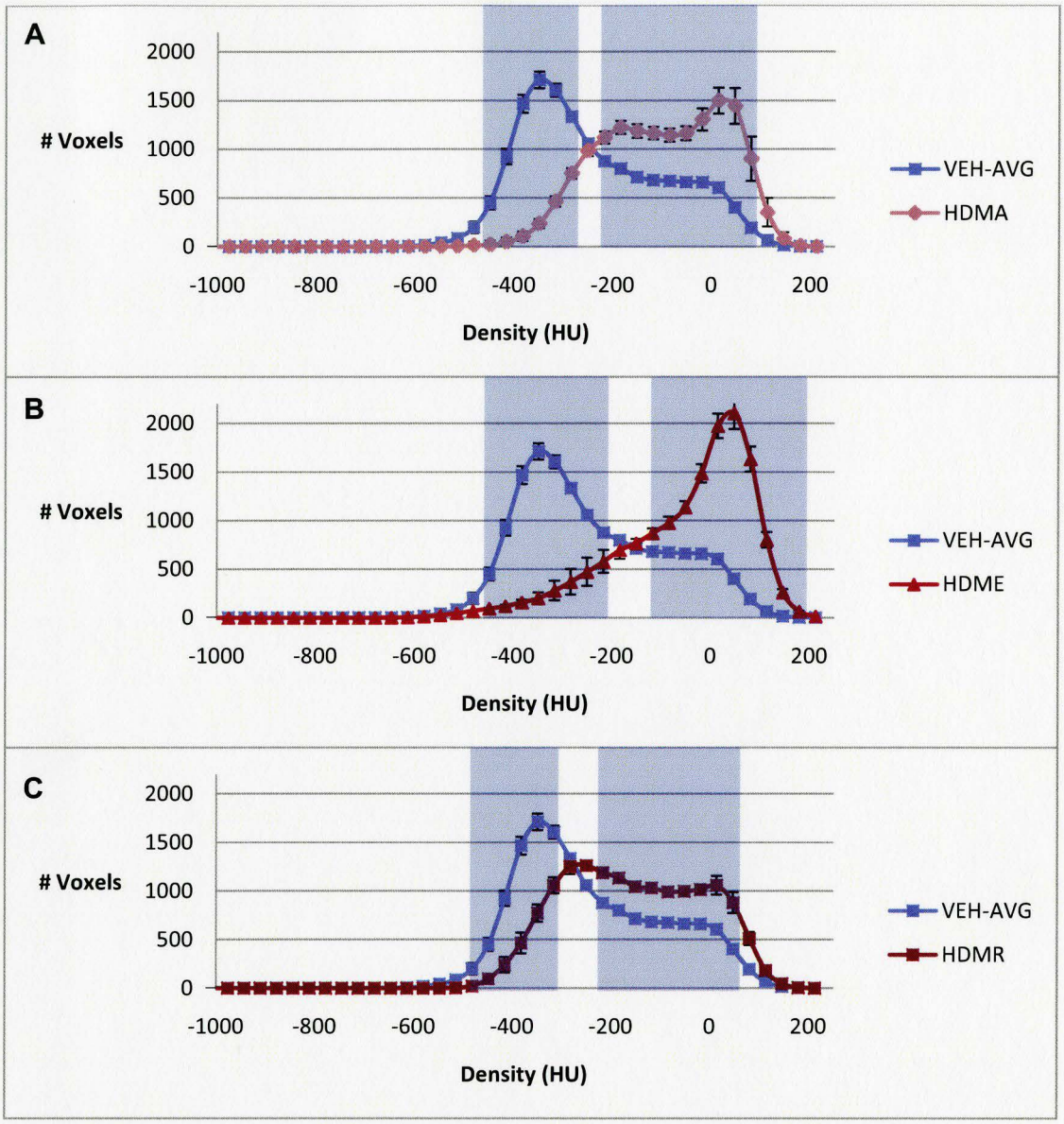

Figure 10. Comparative density distributions of the region around the large airways of asthma models to controls. (A) acute HDM exposure (HDMA) (n = 6) compared to the controls (VEH-AVG) (n=24); (B) chronic HDM exposure (HDME) (n = 12) compared to the controls (VEH-AVG) (n=24); (C) recovery following chronic HDM exposure (HDMR) (n = 6) compared to the controls (VEH-AVG) (n=24). All points represent the mean value and SEM. The blue boxes indicate bins between groups that are statistically different from each other ($P < 0.05$). This was determined by applying one way ANOVAs at each density bin.

To determine if we could discriminate between different exposure groups using CT densitometry, plots of the three groups within the asthma model were compared (**Figure 11**). The HDM exposure groups had regions which were significantly different from each other. The most notable were found between HDME and HDMA and HDMR groups (**Figure 11 A & C**). The HDME compared to HDMA, and to the HDMR group, had an overall shift towards the denser region, with significantly more voxels compared to the other groups in the range 0 to 150 HU, peaking around 50 HU ($P < 0.05$). This rightward shift in the HDME group also caused a region with significantly less voxels from the HDMA and HDMR groups in the lower density region (~-250 to -100 HU) ($P < 0.05$).

The acute asthma (HDMA) and recovery groups (HDMR) were also significantly different (**Figure 11 B**). The HDMA group was shifted rightward to the denser region of the graph compared to the HDMR group. This shift produced a small region of the HDMR group that is significantly greater from the HDMA group in the less dense region (~-300 HU) ($P < 0.05$). Thus, overall there was an increase in voxels found in the denser region of the HDMA group compared to the HDMR group, and an even greater increase in voxels in the denser region in the HDME group compared to the HDMA and HDMR groups.

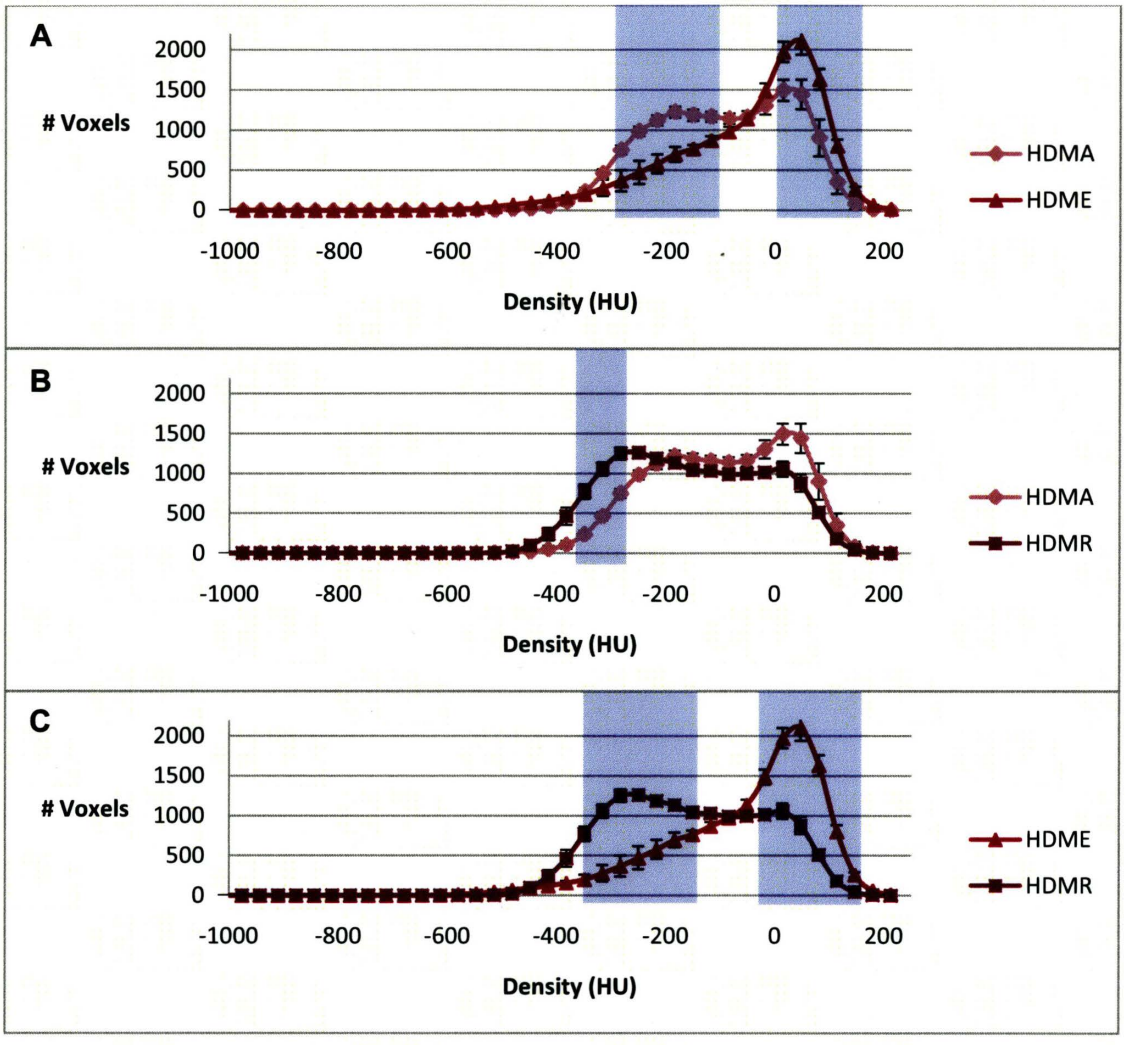

Figure 11. Comparative density distributions of the region around the large airways of asthma models. (A) acute HDM exposure (HDMA) (n = 6) vs. chronic HDM exposure (HDME) (n=12) to assess if differences occur between incidences of eosinophilic inflammation (HDMA) and eosinophilic inflammation and remodelling (HDME); (B) acute HDM exposure (HDMA) (n = 6) vs. recovery following chronic HDM exposure (HDMR) (n = 6) to compare eosinophilic inflammation (HDMA) to remodelling only (HDMR); (C) chronic HDM exposure (HDME) (n=12) vs. recovery following chronic HDM exposure (HDMR) (n = 6) to compare eosinophilic inflammation and remodelling (HDME) to remodelling only (HDMR). All points represent the mean value and SEM. The blue boxes indicate bins between groups that are statistically different from each other ($P < 0.05$). This was determined by applying one way ANOVAs at each bin.

3.1.3 Total and Differential Cell Counts

The acute asthma model (HDMA) and the chronic asthma model (HDME) groups both had statistically higher TCC compared to their controls and to the recovery group (HDMR) (**Figure 12**) ($P < 0.05$). TCC from the HDMR group was found to be no different from its control (VEH-HDMR) (**Figure 12**).

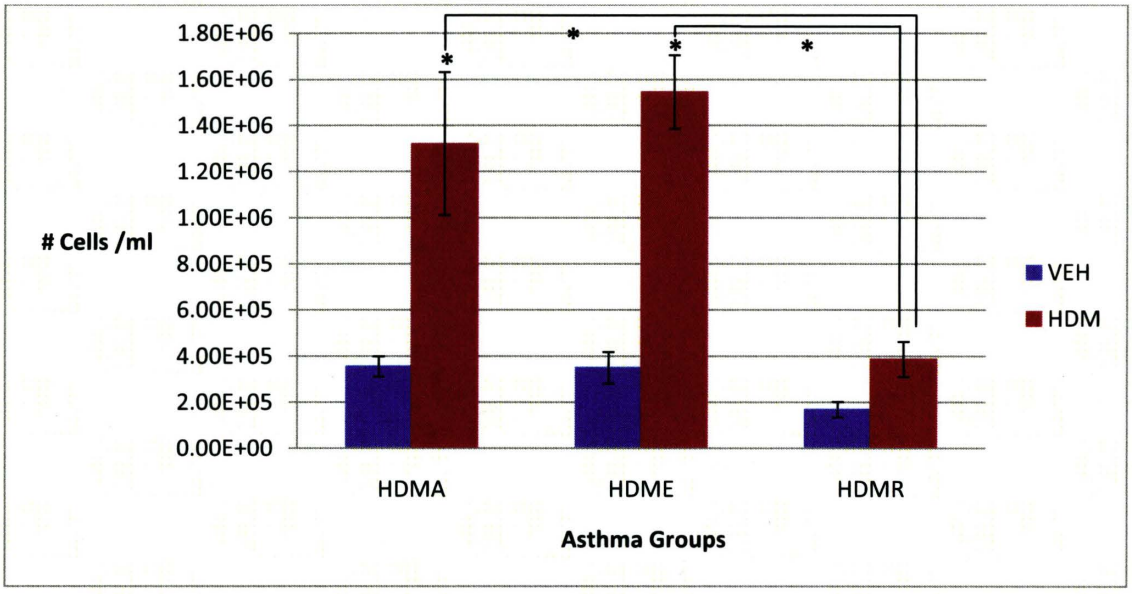

Figure 12. Total cell counts (TCC) from BAL samples of asthma models. Data contains TCC from models of acute (HDMA) (n=12), and chronic (HDME) (n=12) asthma and recovery following chronic HDM exposure (HDMR) (n=11) and their vehicle treated, age-matched controls (VEH-HDMA (n=12), VEH-HDME (n= 12), and VEH-HDMR (n=10)). All bars represent the mean value. Error is expressed as SEM. (*) indicates statistical significance ($P < 0.05$).

The DCC showed that eosinophilia was present in the HDMA and HDME groups (**Figure 13**). Both groups were statistically different from their controls, each other, and from the HDMR group which shows no measurable statistical difference from its control (**Figure 13**) ($P < 0.05$). Lymphocytes and neutrophils

are statistically higher in the HDME group from the control, HDMA, and HDMR groups (**Figure 13**) ($P < 0.05$). No statistical difference was found between any of the groups or their controls in the number of macrophages.

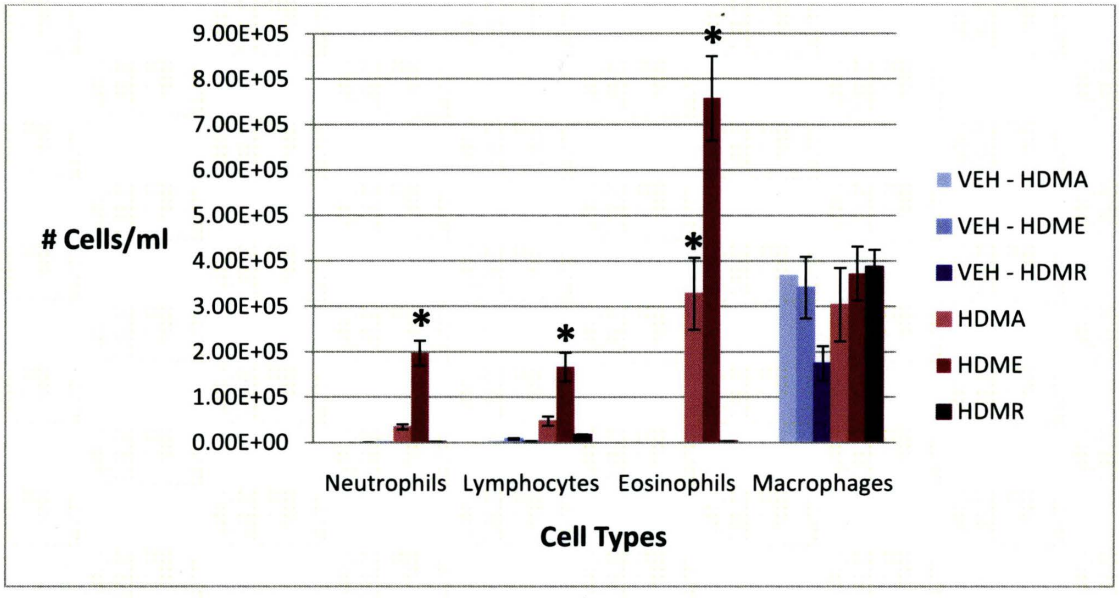

Figure 13. Differential cell counts (DCC) from BAL samples in the asthma models. Data contains DCCs from acute (HDMA) (n=5), and chronic (HDME) (n=9) asthma models and recovery following chronic HDM exposure (HDMR) (n=10) and their vehicle treated, age-matched controls (VEH) (VEH-HDMA (n=5), VEH-HDME (n=12), and VEH-HDMR (n=8)). All bars represent the mean value. Error is expressed as SEM. (*) indicates statistical significance from controls ($P < 0.05$)

3.1.4 Histology

In the HDMA, HDME, and HDMR groups inflammation was present around the airways (indicated by red arrows) (**Figure 14 A**, **C** & **E**). The extent of inflammation appeared to be the highest in the HDME group (**Figure 14 C**). For this study airway remodelling (indicated by black arrows) was said to be present if goblet cell hyperplasia and increased airway smooth muscle were identified. Goblet cell hyperplasia appears as a thickening and increased transparency of the epithelial layer of the airways and an increase in smooth muscle mass can be visualized by the presentation of increased airway thickness. The airways appeared to be thicker in both the HDMR and HDME groups (black arrows) (**Figure 14 C** & **E**).

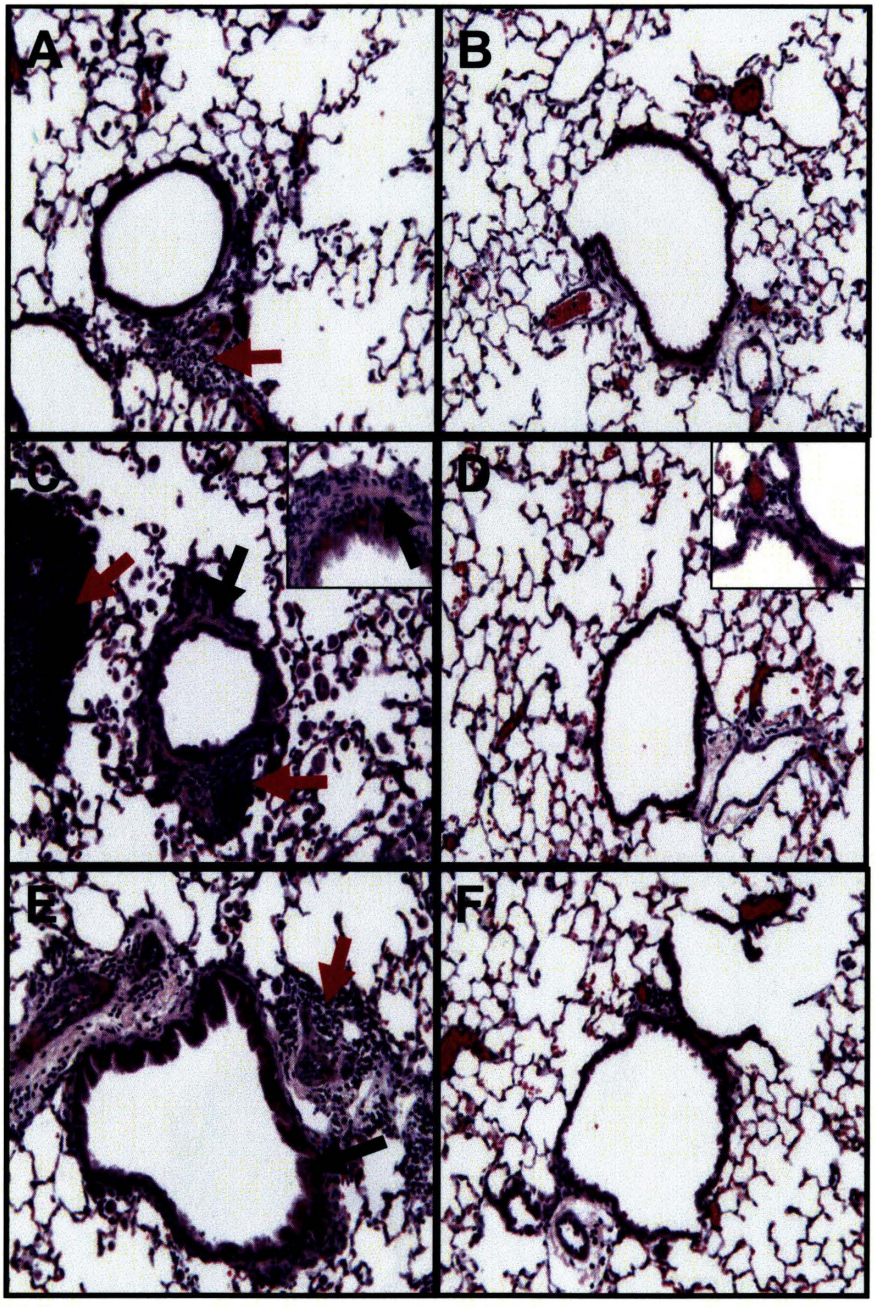

Figure 14. Representative lungs from asthma models. (A) acute HDM exposure (HDMA), (B) vehicle treated control (VEH-HDMA), (C) chronic exposure (HDME), (D) VEH-HDME, (E) recovery following chronic exposure (HDMR), and (F) its vehicle-treated control (VEH-HDMR). Red arrows indicate regions of inflammation. Black arrows indicate regions of remodelling.

3.1.5 Physiology: Total Lung Resistance

When the asthma model is successfully created, we expect to see increased lung resistance following a methacholine challenge in animals sensitized to HDM compared to controls as previously reported by Hirota and colleagues (Hirota et al, 2010). The HDMA, HDME and HDMR groups had a significant increase in slopes compared to controls (**Figure 15**) ($P < 0.05$). This indicates that all disease groups had airway hyperresponsive to Mch producing increased total lung resistance relative to controls.

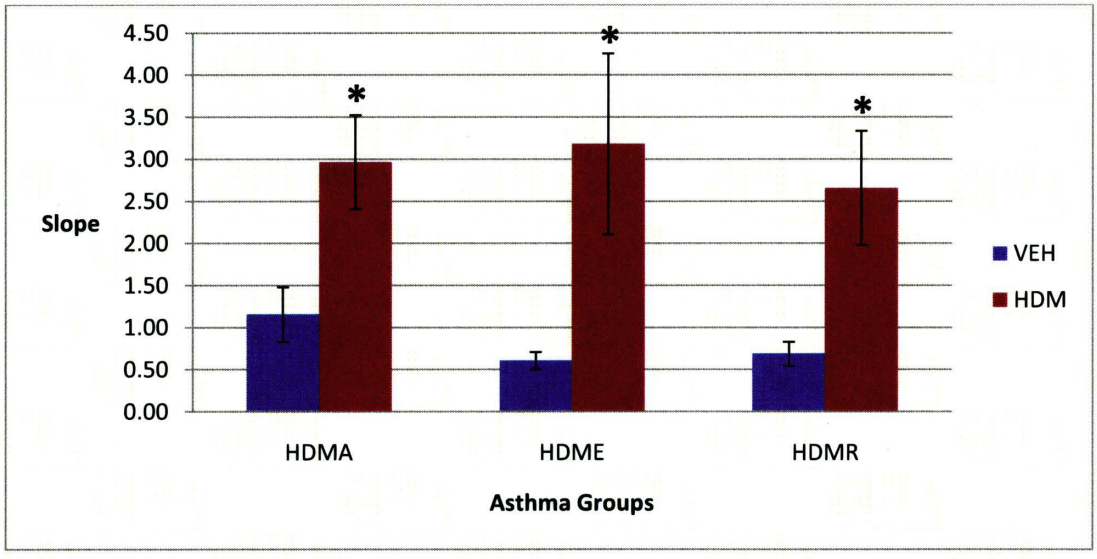

Figure 15. Slopes from lung resistance compared to dose (Mch) in mouse asthma models. The data are from HDMA (n = 12), HDME (n = 12) and HDMR (n = 12), and their age-matched, vehicle-treated controls VEH-HDMA (n = 12), VEH-HDME (n = 12) and VEH-HDMR (n = 12). The mice were given varying doses of Mch and their total lung resistance was measured after each dose. This plot shows the slopes from the dose response plot for all asthma models. An unpaired t-test was performed between the control and HDM exposed animals for each individual model to determine if they are statistically different from each other. (*) indicates statistical significance from the control ($P < 0.05$). Error expressed as SEM.

3.2 LPS Induced Neutrophilic Inflammation

3.2.1 Representative CT Images

Visual assessment of the representative CT images showed regions of high attenuation around the airway in the LPS model at 24 hrs after delivery of LPS compared to controls (**Figure 16**). Increases in attenuation were only marked at the 24 h time point compared to the control (images at 7 hrs and 2 weeks not shown). Airway diameter at rib 7 was statistical larger in the LPS-24h group compared to the control, but diameters at rib 8 and 9 had no significant differences between LPS exposed and control animals (**Appendix**, **Figure 40**).

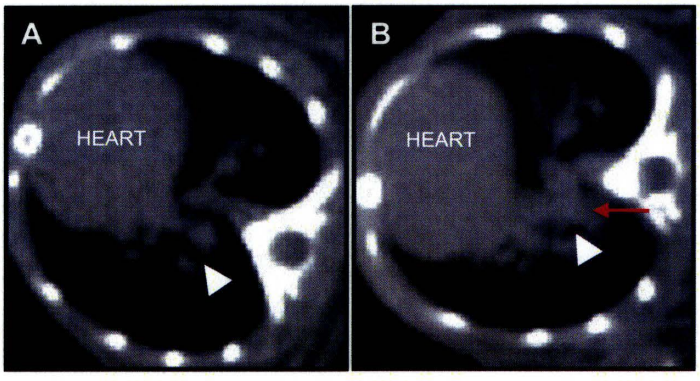

Figure 16. Representative CT image of LPS induced neutrophilic inflammation. This is an axial image of a CT image of the lungs. (A) vehicle treated control and (B) 24 hrs after delivery of LPS. White arrows indicate airways. Red arrows indicate high attenuation region around airways.

3.2.2 CT Densitometry

The plot from the large airway segmentation at the three time points (7 hrs, 24 hrs, & 2 weeks) after exposing the mice to LPS compared to the grouped controls is illustrated in **Figure 17**. From this plot it is possible to see at 24 hours

after LPS exposure (LPS-24h) the shape of the curve is altered compared to controls and to the LPS exposure groups at 7 hours (LPS-7h) and 2 weeks (LPS-2w) after LPS delivery. Of the LPS exposure groups the LPS-7h and LPS-24h were the only groups which had regions that were statistically different from the control group (VEH-AVG) (**Figure 18 A & B**). The LPS 7h group was shifted slightly to the denser region on the right expressing two small regions, one in the less dense area having significantly less voxels compared to the control group (~-300 HU), and one in the denser region (~50 HU) with significantly more voxels than the control group (**Figure 18 A**). The LPS-24h group was shifted to the denser region compared to the control group, producing a single flattened peak (**Figure 18 B**). LPS-24h has a region in the less dense area on the left, which has significantly less voxels than the control (~-350 HU) and on the denser region on the right that has significantly more voxels than the control group (~-200 to 50 HU). These results indicate that an overall increase in voxels in the denser region are apparent in both the LPS-7h and LPS-24h group, with a larger increase in voxel frequency in the higher density range in the LPS-24h group. The LPS-2w group was found to be no different from the controls (Figure 17. Density distribution around selected large airways in mouse models of LPS induced neutrophilic inflammation. **Plots from the segmentations at 7 hours (LPS-7h), 24 hours (LPS-24h) and 2 weeks (LPS-2W) after LPS exposure and their vehicle treated controls (VEH-AVG). Figure 18 C**). Over the measured density

interval the controls had no regions which were statistically different from each other (Figure not shown) ($P > 0.05$).

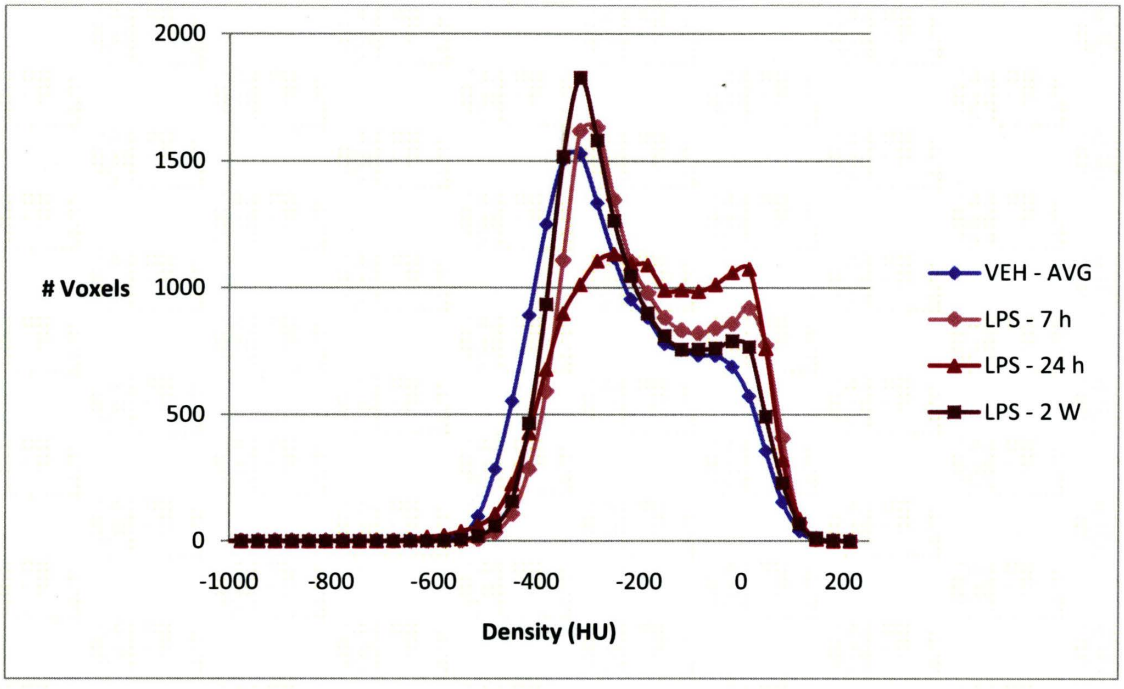

Figure 17. Density distribution around selected large airways in mouse models of LPS induced neutrophilic inflammation. Plots from the segmentations at 7 hours (LPS-7h), 24 hours (LPS-24h) and 2 weeks (LPS-2W) after LPS exposure and their vehicle treated controls (VEH-AVG). The controls (VEH-AVG) (age matched, vehicle treated) for each LPS model were combined as they were found to not be statistically different from each other.

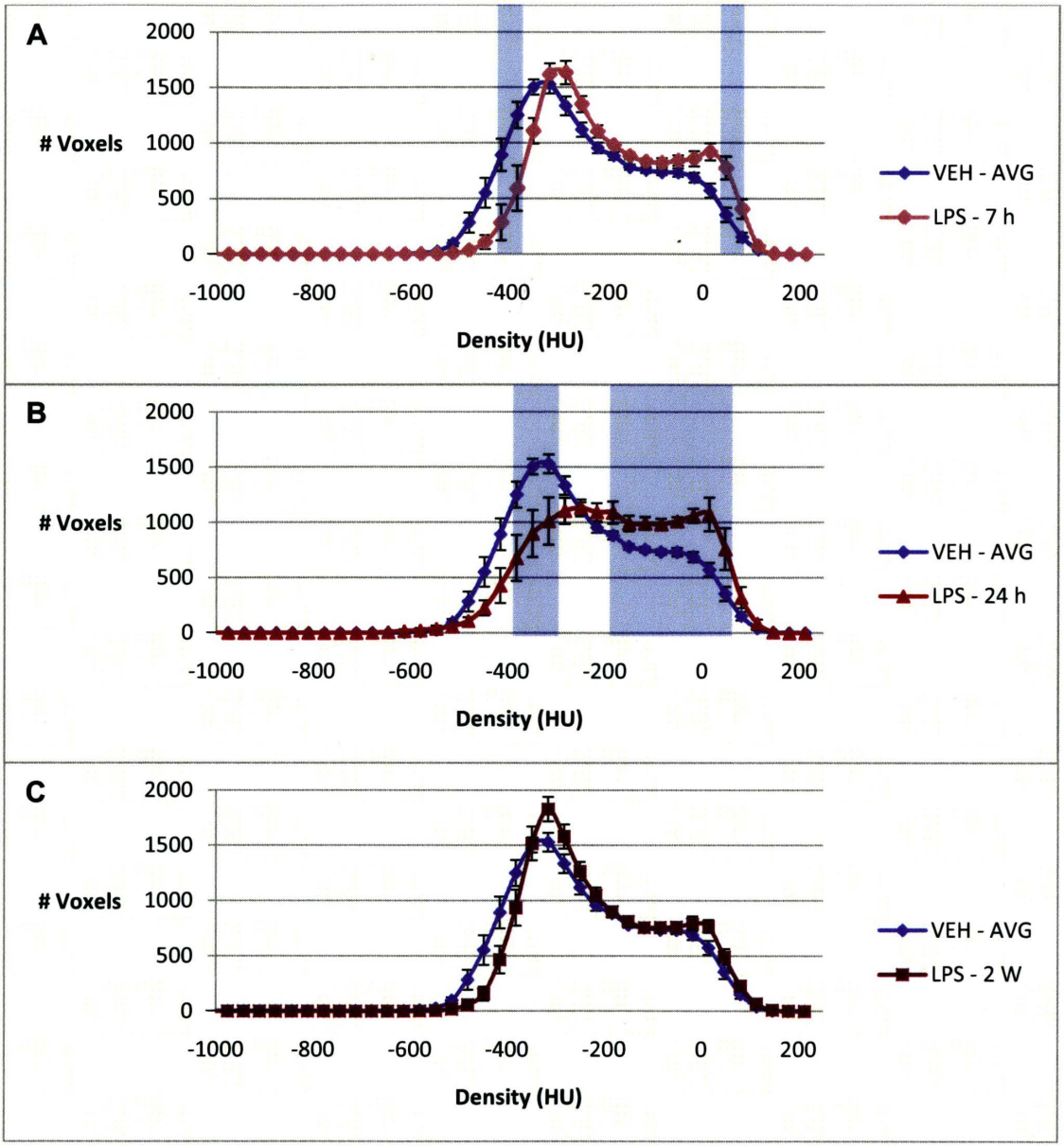

Figure 18. Comparative density distributions around selected large airways in mouse models of LPS induced neutrophilic inflammation from grouped vehicle treated controls. (A) LPS-7h group (n=6) is compared to the vehicle treated controls (VEH-AVG) (n=16); (B) LPS-24h (n=7) is compared to VEH-AVG; and (C) LPS-2w (n=6) group is compared to VEH-AVG. A one way ANOVA was performed at each bin. All points represent the mean and SEM. The blue boxes indicate regions which are statistically different from each other ($P < 0.05$).

The plots of the airway segmentations between each of the three LPS exposure groups showed statistically significant differences between the LPS-24h group and the LPS-7h and LPS-2w exposure groups only. The LPS-24h group had significantly less voxels in the less dense region (~-300 HU) on the left and an increase in voxels on the denser region (-100 HU) compared to the LPS-7h and the LPS-2W groups (**Figure 19 A & B**) ($P < 0.05$). This indicates an overall shift in voxel frequency of the LPS-24h group to denser region compared to the other two exposure groups. No significant difference was detected between LPS-7h and LPS-2w groups (**Figure 19 C**).

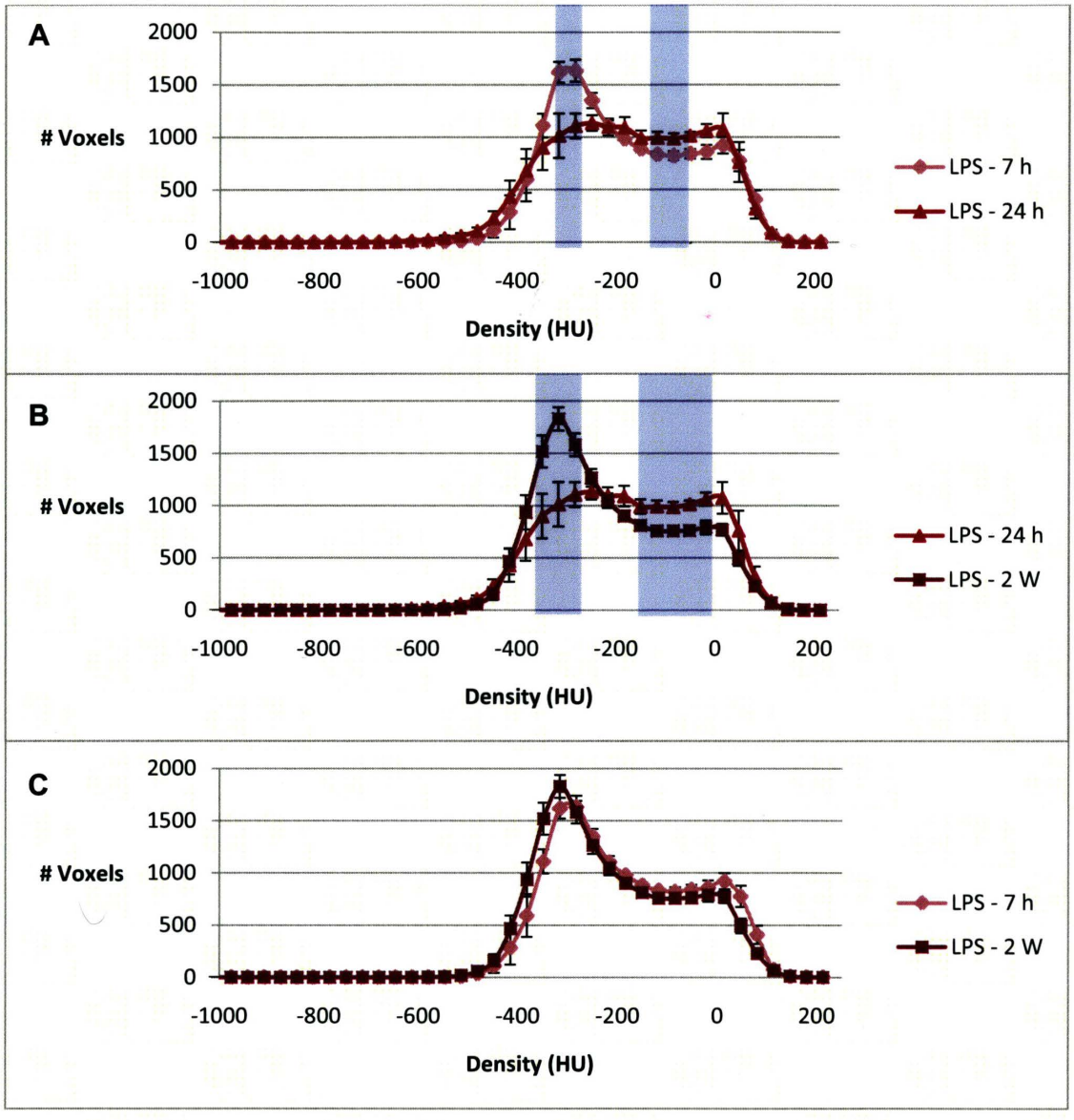

Figure 19. Comparative density distributions around large airways in mouse models of LPS induced neutrophilic inflammation. (A) LPS-7h (n=6) vs LPS-24h (n=7) compares density differences between initiatal and maximum inflammation. (B) LPS-24h (n=7) vs LPS-2w (n=6) compares peak inflammation to recovery following inflammation. (C) LPS-7h (n=6) vs LPS-2w (n=6) compares density differences between iniatial inflammation and recovery. All points represent the mean values and SEM. The blue boxes indicate regions of statistical significance ($P < 0.05$). This was determined by applying one way ANOVAs at each bin.

3.2.3 Total and Differential Cell Counts

TCC were statistically higher in the LPS-24h compared to its control (**Figure 20**) ($P < 0.05$). The 24 h time point was also found to be significantly higher than the LPS-7h and LPS-2w, both of which were found to show no significant difference from their controls (**Figure 20**).

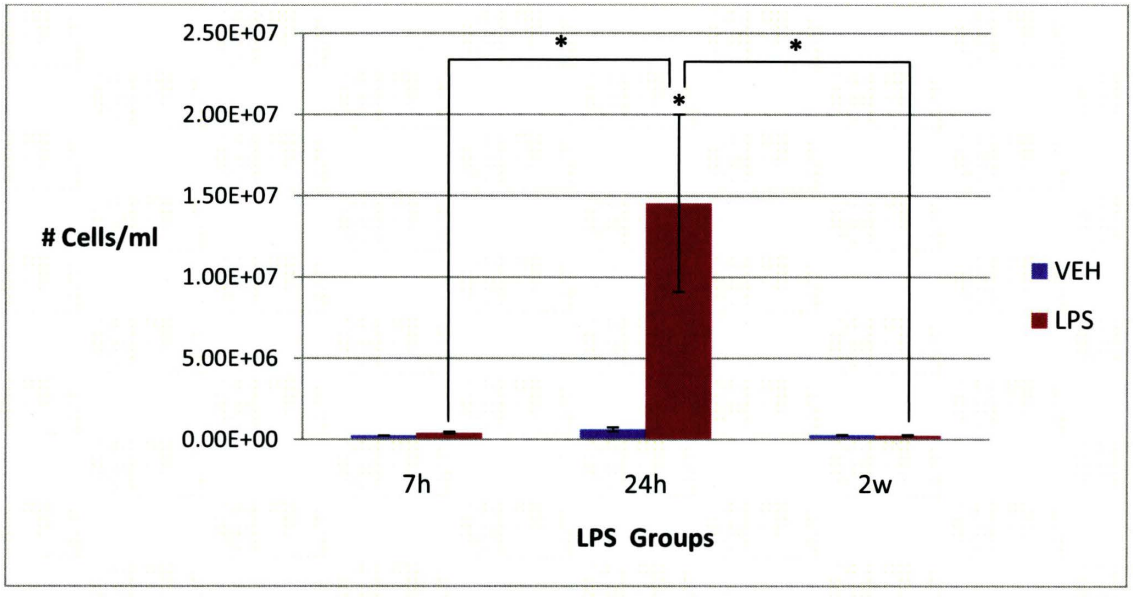

Figure 20. Total cell counts (TCC) from BAL samples of mouse models of LPS induced neutrophilic inflammation. 7h (LPS-7h) (n=6), 24h (LPS-24h) (n=2) and 2w (LPS-2w) (n=6) post exposure and their vehicle treated and age-matched controls (VEH-7h ((n=4), VEH-24h (n=4), and VEH-2w (n=4)). All bars represent the mean value. Error is expressed as SEM. (*) indicates statistical significance ($P < 0.05$)

From the differential cell counts neutrophilia was present in the LPS-24h group compared to its control VEH-24h (**Figure 21**). The LPS-7h and LPS-2w did not have statistically elevated neutrophil counts compared to their controls (**Figure 21**). Macrophage counts were significantly higher at 24 h after LPS

exposure compared to its control and the other exposure groups (LPS-7h and LPS-2w) ($P < 0.05$). Eosinophils and lymphocytes were not present in the counts.

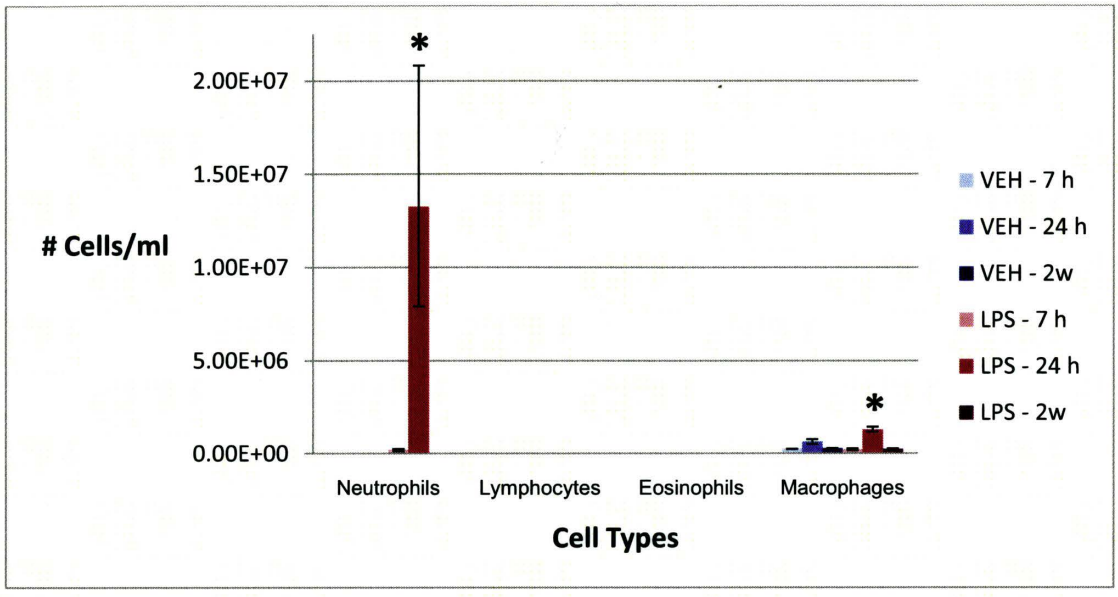

Figure 21. Differential cell counts (DCC) from BAL samples of mouse models of LPS induced neutrophilic inflammation. 7h (LPS-7h) (n=6), 24h (LPS-24h) (n=2) and 2w (LPS-2w) (n=6) post LPS exposure and their vehicle treated and age-matched controls: VEH-7h (n=4), VEH-24h (n=4), VEH-2w (n=4)). All bars represent the mean value. Error is expressed as SEM. (*) indicates statistical significance from controls ($P < 0.05$)

3.2.4 Histology

In the representative lung slices inflammatory cell infiltration into the airspaces is visible 7 h (**Figure 22 A**) and 24 h (**Figure 22 C**) after LPS delivery (indicated by a black arrow). No cell infiltrations were visible in the controls (**Figure 22 B**, **D** and **F**) or 2 weeks following LPS (**Figure 22 E**).

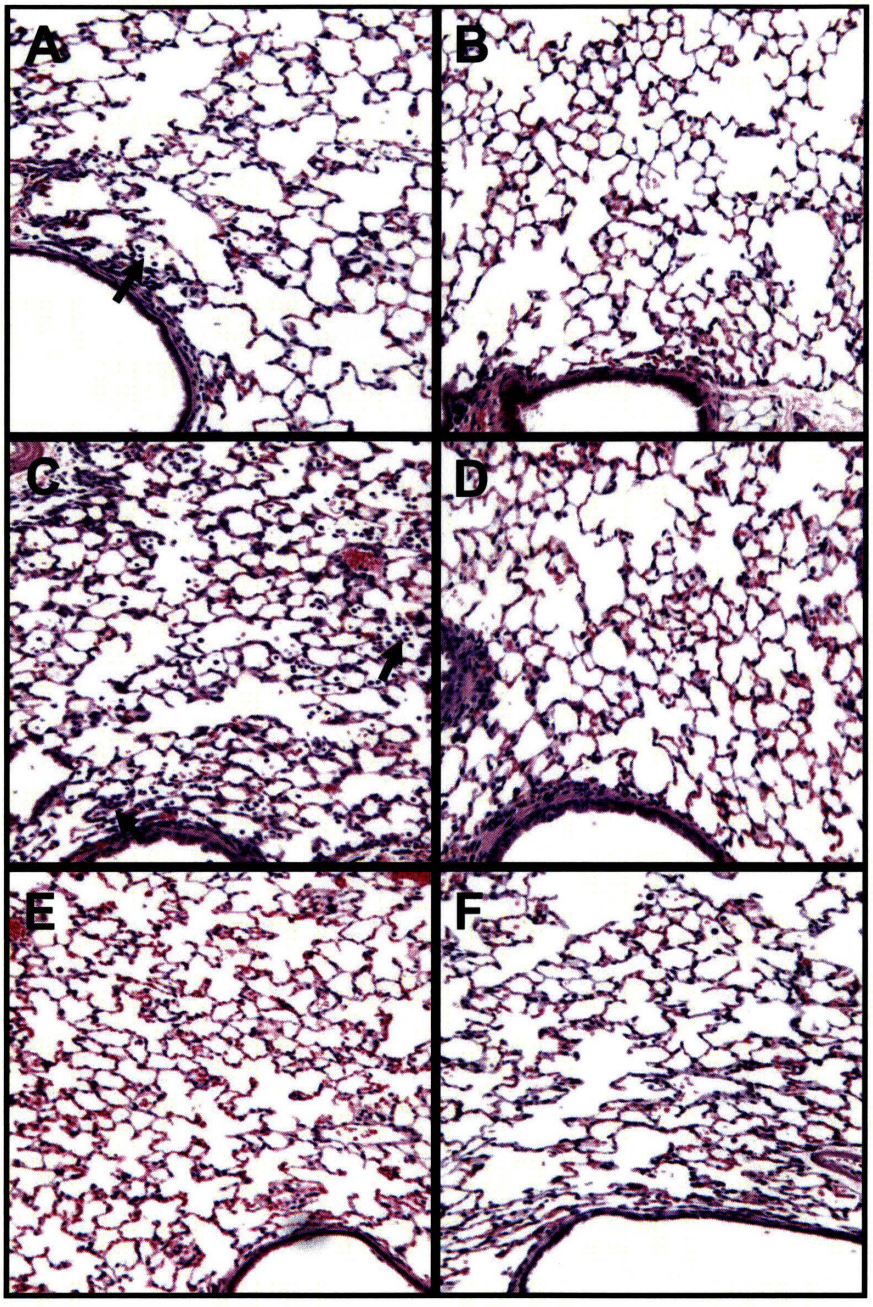

Figure 22. Representative lungs from LPS induced neutrophilic inflammation models (X20). (A) 7 h after LPS delivery; (B) vehicle treated control; (C) 24 hrs after LPS delivery; (D) vehicle-treated control; and (E) 2 weeks after LPS delivery, and (F) vehicle-treated control. Arrows indicate inflammatory cells. The slides were stained with H&E.

3.3 Pulmonary Fibrosis

3.3.1 Representative CT Images

From the representative CT images the pulmonary fibrosis groups showed equivalent large areas of high attenuation around the airways at 2, 3 and 4 weeks after delivery of the TGF-β adenovirus vector (**Figure 23**). Airway diameters at rib 7, 8, and 9, were all statistically larger than the control group 2 weeks after adTGFβ-1 delivery (**Appendix**, **Figure 41A**). Airway diameters were elevated in the 3 weeks post adTGFβ-1 group at rib 7, 8, and were statistically larger at rib 9 compared to the control group (**Appendix**,**Figure 41B**). In the 4 week group no differences in airway diameters were detected compared to the control groups (**Appendix**,**Figure 41C**).

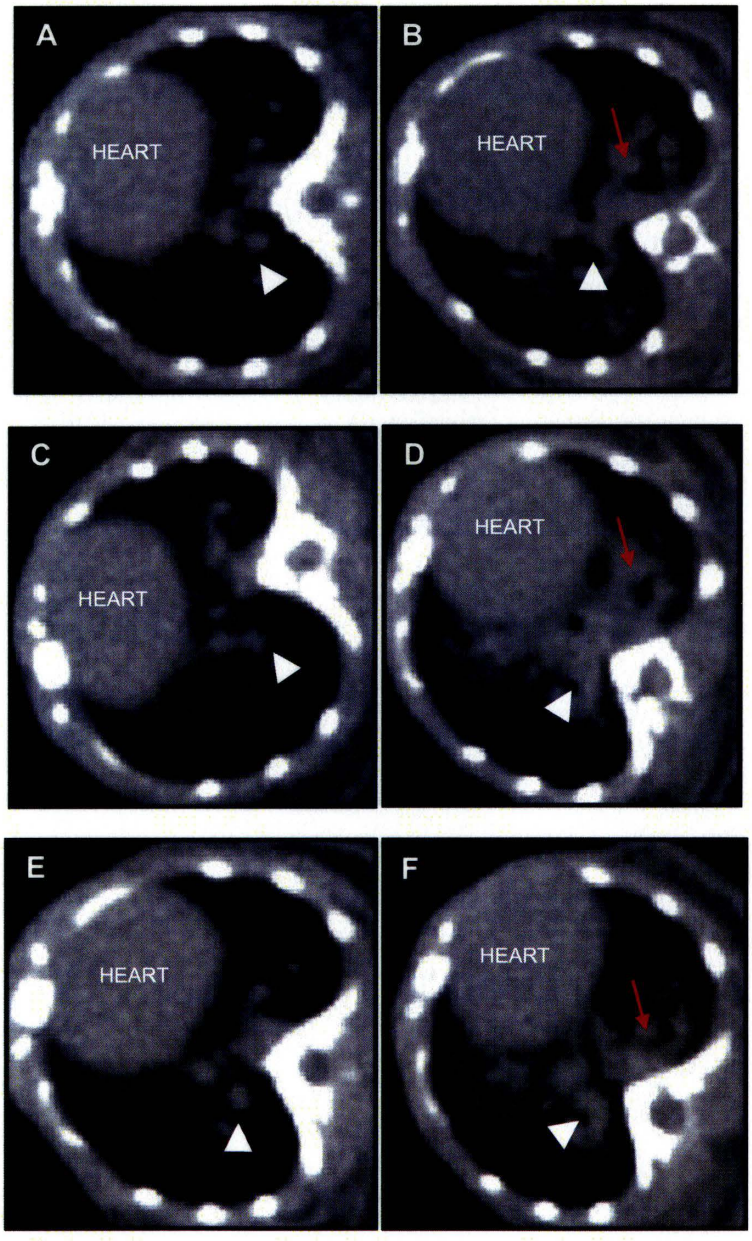

Figure 23. Representative axial CT image of the pulmonary fibrosis model following delivery of adTGF-B1 and their age matched and vehicle treated control. This was taken at rib 8 in the (A) control and (B) the PF groups at 2 weeks; (C) control and (D) the PF groups at 3 weeks; (E) control and (F) the PF groups at 4 weeks. At all time point fibrosis should be present in the disease models. White arrows indicate airways. Red arrows indicate high attenuation region around airways.

3.3.2 CT Densitometry

Figure 24 illustrates the plots from the airway segmentations of all three adTGFβ-1 exposure groups at 2, 3, and 4 weeks after IT delivery of the vector. All three time points had a large number of voxels in the higher density range with a peak around 15 HU compared to controls (peak at -350 HU) (**Figure 24**). **Figure 25** illustrated the statistical differences measured at each density bin between the PF disease groups and the grouped control. The time points TGF-β-2w (**Figure 25 A**); TGF-β-3w (**Figure 25 B**); and TGF-β-4w (**Figure 25 C**) had significantly more voxels in the denser range (-150 to 150 HU) than the controls. This rightward shift of voxel frequency in the disease groups produced regions on the less dense side (-400 to -250 HU) that were significantly different from controls. These results indicate an overall increase in voxels possessing a higher density within the selected region around the airways in the disease groups. In addition at 2 weeks after delivery of TGFβ-1 a significant increase in voxel frequency in the extremely low density range (~-700 to -600 HU) occurred compared to controls. From the airway segmentations no statistical significance was found between the CT densitometry plots at the three time points in the PF groups (**Figure 24**).

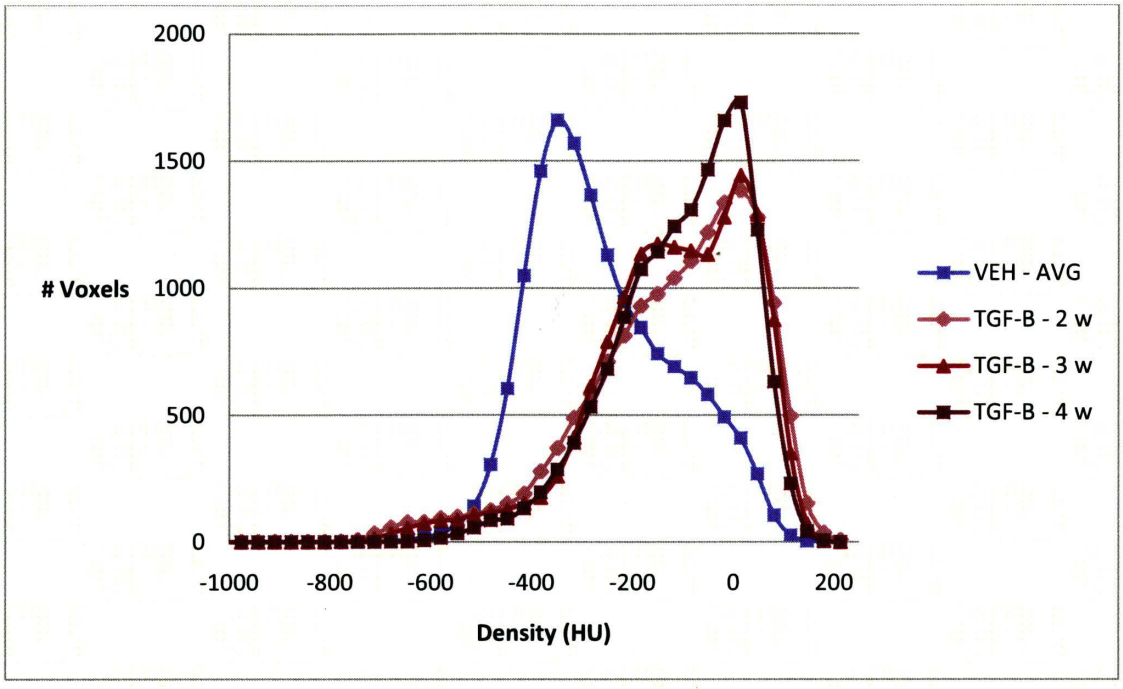

Figure 24. Density distribution of the large airway segmentation of pulmonary fibrosis. Plots from the segmentations at 2 weeks (TGF-β-2w), 3 weeks (TGF-β-3w), and 4 weeks (TGF-β-4w) after received adTGFβ-1 and their vehicle treated controls (VEH-AVG). The controls (VEH-AVG) (age matched, vehicle treated) for each PF model were combined as they were found to not be statistically different from each other.

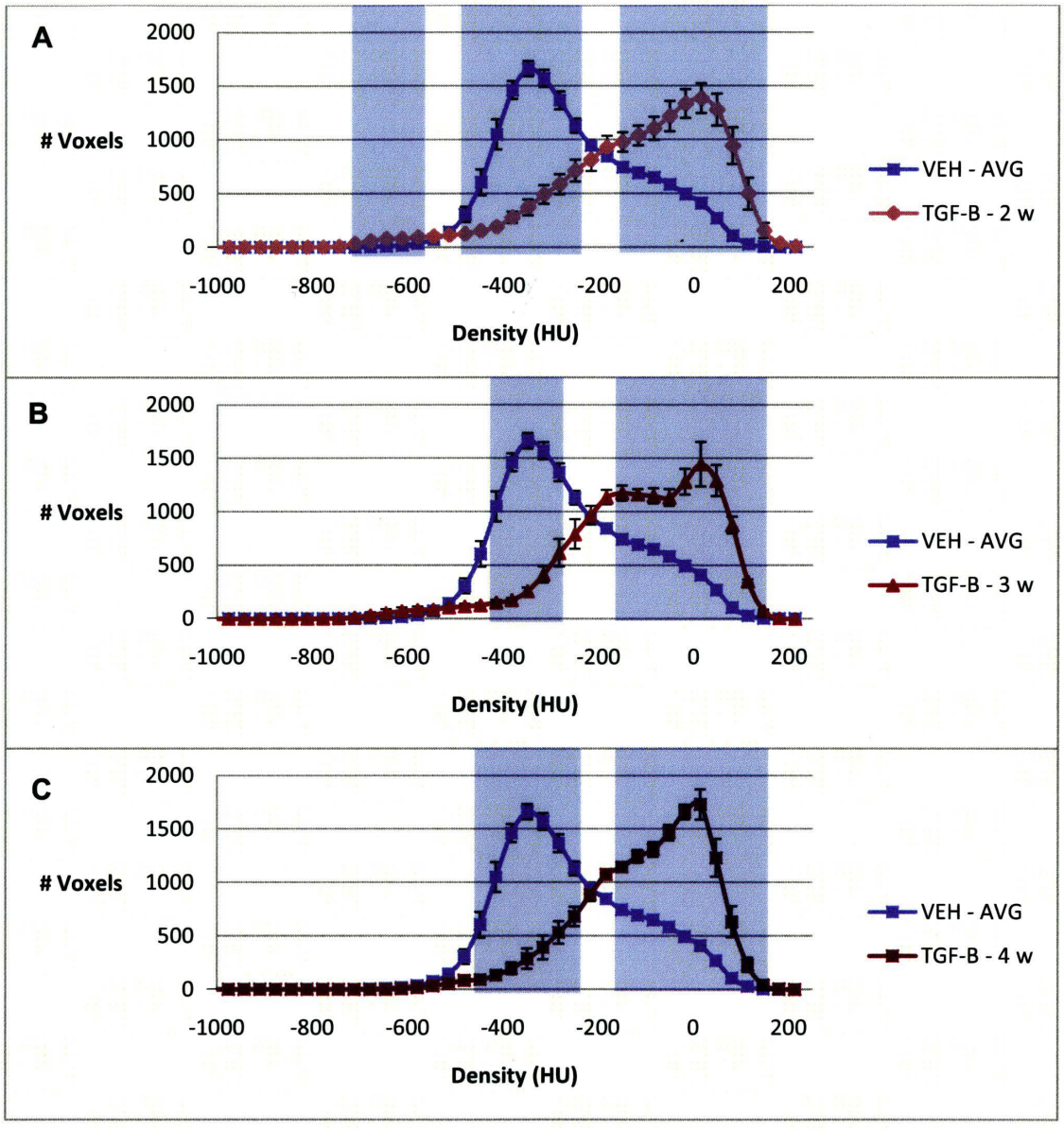

Figure 25. Density distribution of the large airway segmentation in pulmonary fibrosis models compared to controls. These plots display the density distribution of the voxels in the segmentation over the density interval of -1025 to 220 HU following delivery of TGF-B1 at: (A) 2 weeks (TGF-β-2w) (n = 12); (B) 3 weeks (TGF-β-3w) (n = 4); and (C) 4 weeks (TGF-β-4w) (n = 5) to the vehicle treated controls (VEH-AVG) (n = 18). All points represent the mean values. The blue boxes indicate regions of statistical significance ($P < 0.05$). Error is presented as SEM.

3.3.3 Total and Differential Cell Counts

For the three time points there was a trend of elevated cell counts, however, from the one-way ANOVA analysis they were not statistically different from their controls nor each other (**Figure 26**).

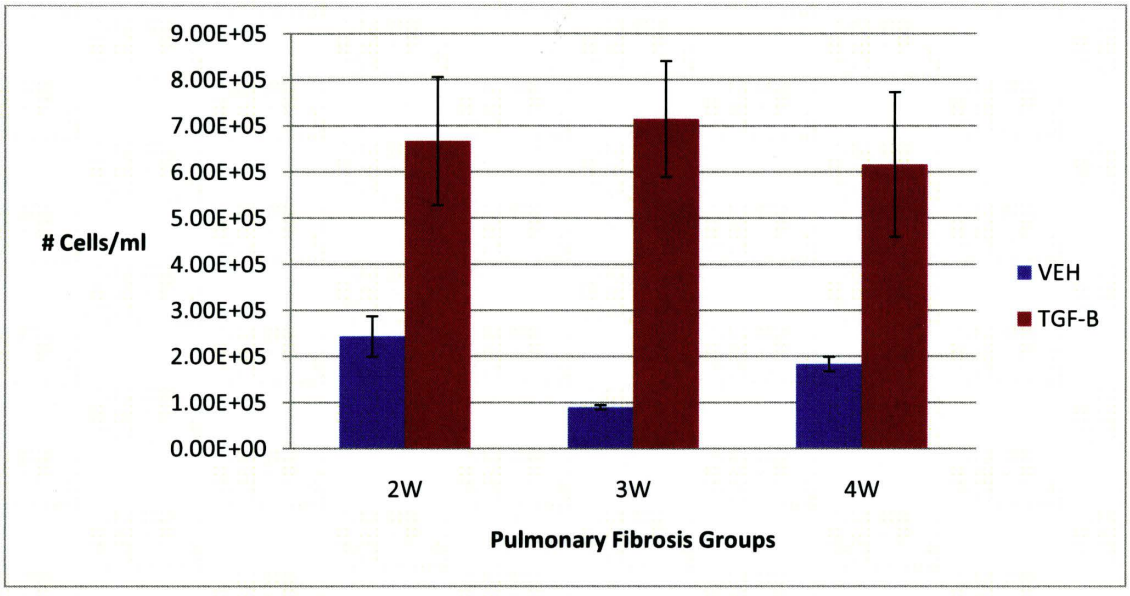

Figure 26. Total cell counts (TCC) from BAL samples of mouse models of PF (TFG-B) 2w (n=3), 3w (n=3) and 4w (n=4) post (adTGF-β1) delivery and their vehicle treated (adDL-70), age-matched controls (VEH) (VEH-2w (n=3), VEH-3w (n=2), VEH-4w (n=3)). All bars represent the mean value. Error is expressed as SEM.

For the three time points there was a trend of elevated macrophages and lymphocytes, however, from the one-way ANOVA analysis they were not statistically different from their controls (**Figure 27**). The number of neutrophils appeared to be higher 2 weeks after delivery of the adTGFβ-1 compared to the control group, but this group had an n = 2 so no statistical assessment could be applied to the data (**Figure 27**).

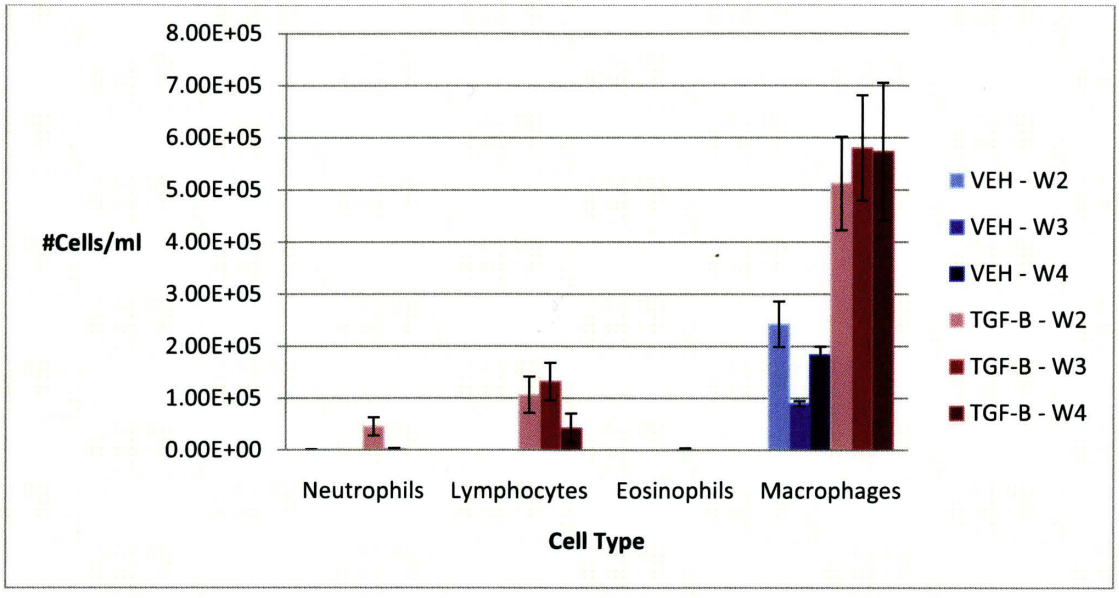

Figure 27. Differential cell counts (DCC) from BAL samples of mouse models of PF 2w (n=3), 3w (n=3) and 4w (n=4) post (adTGF-β1) delivery and their vehicle treated (adDL-70), age-matched controls (VEH) (VEH-2w (n=3), VEH-3w (n=2), VEH-4w (n=3)). All bars represent the mean value. Error is expressed as SEM.

3.3.4 Histology

At all time points following delivery of adTGF-β the lung parenchyma was visibly thicker from the controls in both the H&E and PSR stains (**Figure 28**). The PSR stained slides show collagen deposition (deep red). Visually no difference was seen between 2w, 3w, and 4w after delivery of the vector, thus only week 2 data is shown below (Figure 28).

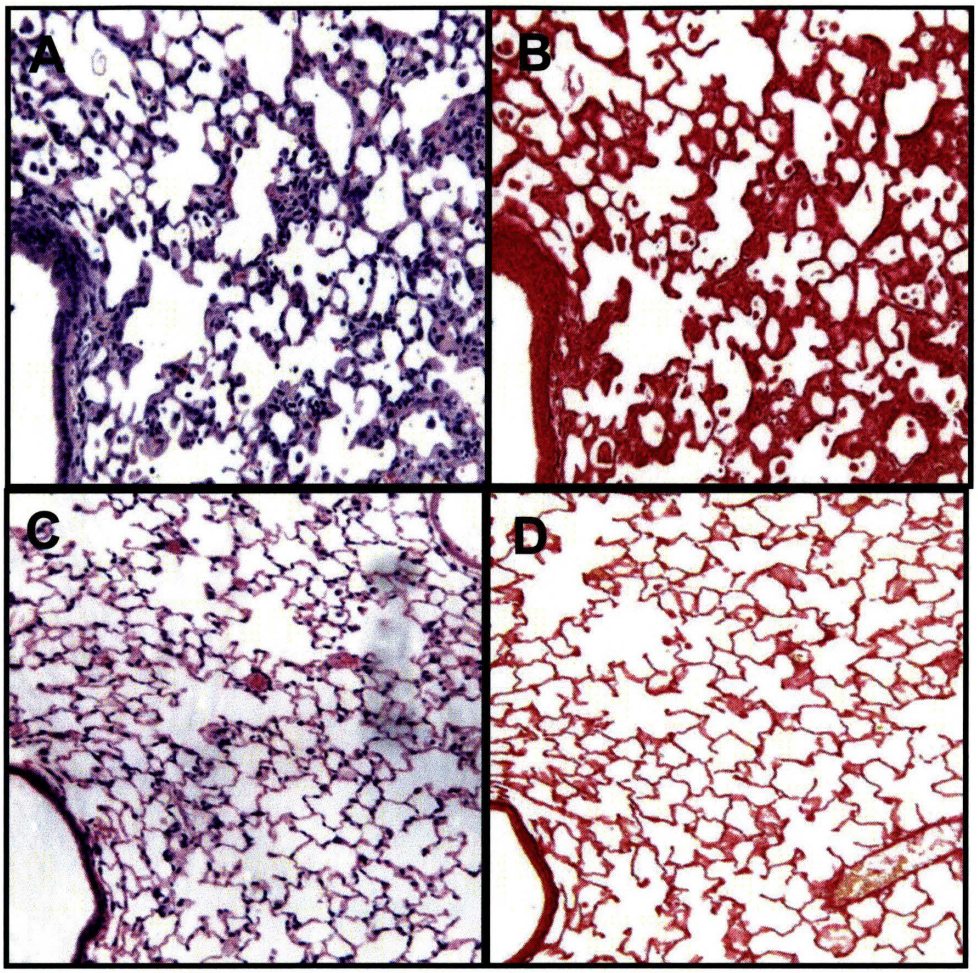

Figure 28. Representative lungs from adTGF-β induced PF models 2 weeks after delivery. (A) PF-2 weeks (H&E), (B) PF-2 weeks (PSR), (C) vehicle treated control (VEH-2w) (H&E), (D) and VEH-2w (PSR) after intratracheal adTGF-β delivery. Deep red staining indicates regions where collagen is present.

3.4 Comparative CT Densitometry

The following sections present data comparing the density distributions of the three disease models to determine if different lung pathologies have unique density profiles. In each subsection first an illustrative plot of all the examined disease groups is shown, followed by paired data sets illustrating regions found to be significantly different between models as determined by pair wise comparisons.

3.4.1 Asthma and Pulmonary Fibrosis Model

3.4.1.1 Acute Asthma and Pulmonary Fibrosis Model

The plots of HDMA and TGF-β-2w (**Figure 29 A**), TGF-β-3w (**Figure 29 B**) and TGF-β-4w (**Figure 29 C**) each had a region that was found to be statistically different from each other. However, overall no significant differences were found between any of the groups in the higher density region. The TGF-β-2w and TGF-β-3w groups both had an increase in voxels in the very low dense region (~-700 to -500 HU) compared to the HDMA group, this was not present at 4 weeks.

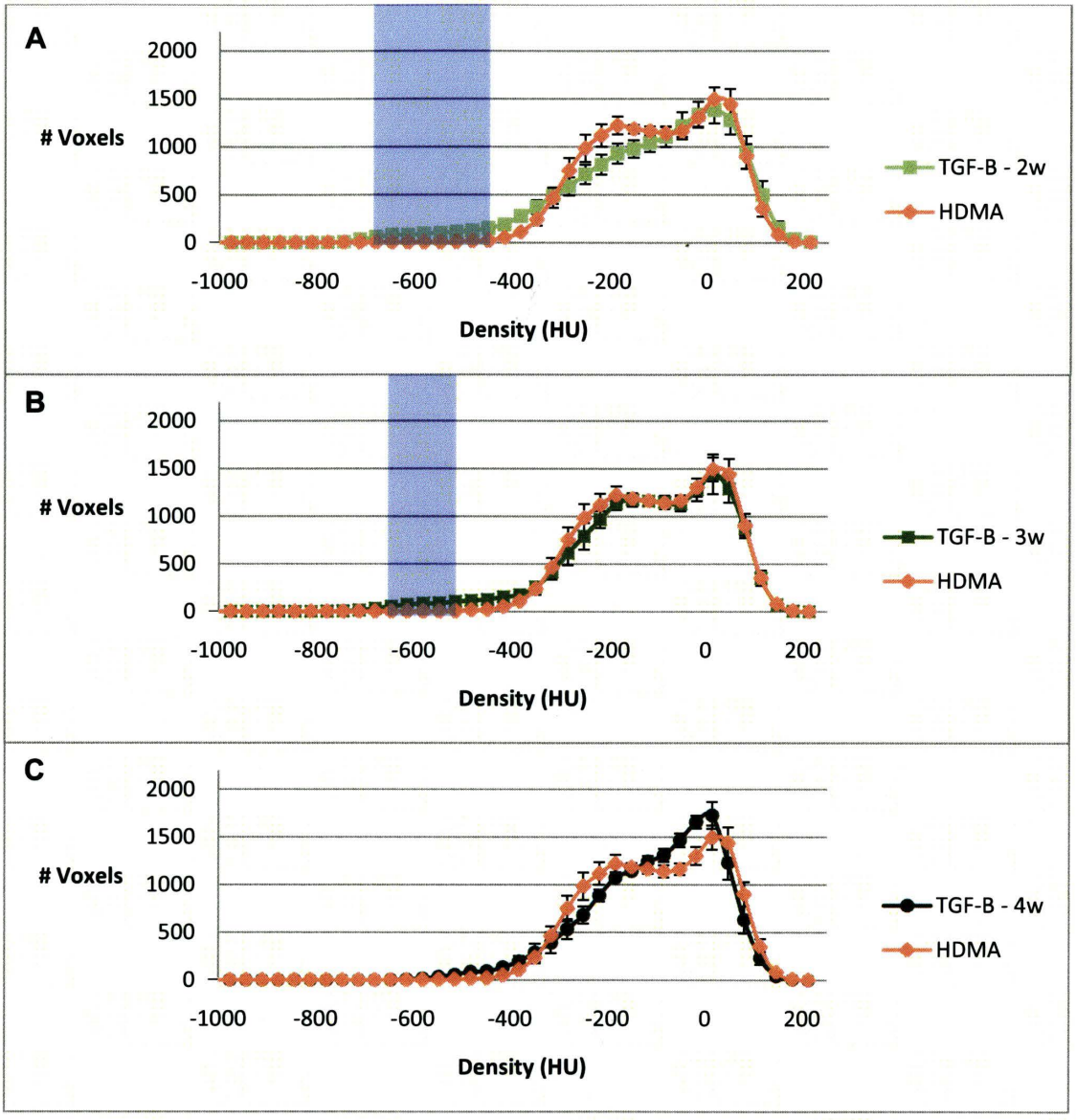

Figure 29. Comparative density distribution around selected large airways of acute asthma (HDMA) and PF models. This plot presents density distributions derived from CT images from the HDMA exposure group (n=6) to mouse models of pulmonary fibrosis at: (A) 2 weeks (TGF-β-2w) (n=12); (B) 3 weeks (TGF-β-3w) (n=4); and (C) 4 weeks (TGF-β-4w) (n=5) following delivery of adTGF-β1. The plots demonstrate if eosinophilic inflammation (HDMA) and fibrosis can be differentiated. The data is expressed as mean values and SEM. A one way ANOVA was performed at each bin. The blue boxes indicate regions of statistical significance ($P < 0.05$).

3.4.1.2 Chronic Asthma and Pulmonary Fibrosis Model

The chronic asthma group (HDME) had a large peak in voxel frequency at a density of ~50 HU compared to all three pulmonary fibrosis groups. This peak in the HDME plot was found to be significantly different than the TGF-β-2w (**Figure 30 A**), TGF-β-3w (**Figure 30 B**) and TGF-β-4w (**Figure 30 C**) groups. In the HDME group there was also a loss of voxels of mid-range density (~-200 to -50 HU) compared to the TGF-β-3w and TGF-β-4w groups, but not in the TGF-β-2w. All three pulmonary fibrosis time points had significantly more voxels in the very low density range on the left (~-700 to -550 HU).

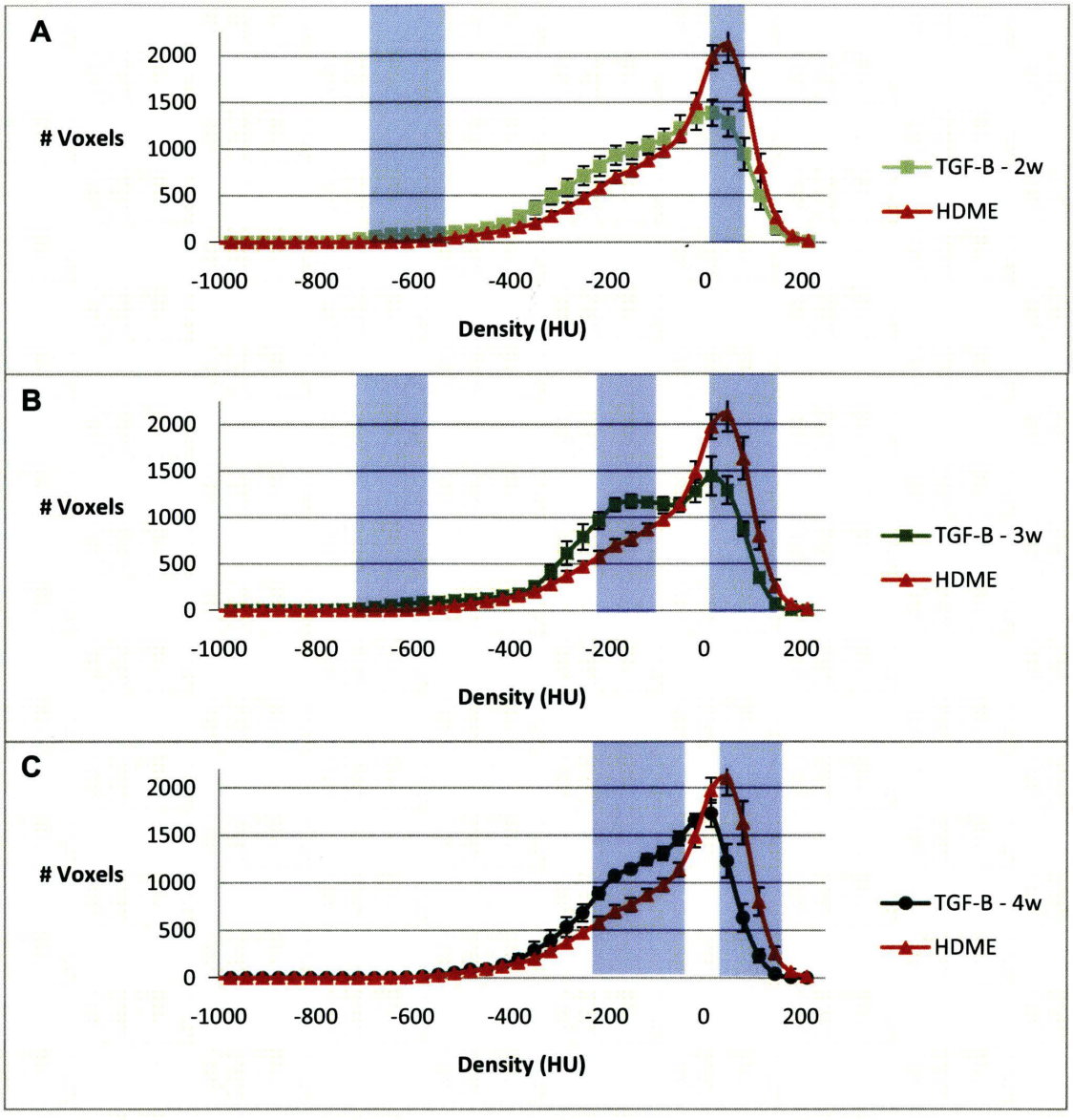

Figure 30. Comparative density distribution around selected large airways of chronic asthma (HDME) and PF models. This plot presents density distributions derived from CT images from the HDME exposure group (n=12) to mouse models of pulmonary fibrosis at: (A) 2 weeks (TGF-β-2w) (n=12); (B) 3 weeks (TGF-β-3w) (n=4); and (C) 4 weeks (TGF-β-4w) (n=5) following delivery of adTGF-β1. The plots demonstrate if fibrosis can be differentiated from eosinophilic inflammation and airway remodeling. The data are expressed as mean values and SEM. A one way ANOVA was performed at each bin. The blue boxes indicate regions of statistical significance ($P < 0.05$).

3.4.1.3 Recovery Following Chronic Asthma and Pulmonary Fibrosis Model

Compared to the recovery group (HDMR), which has its peak density around -300 HU, all three pulmonary fibrosis groups are shifted to the denser region on the right peaking ~15 HU. The peak in the HDMR plot (~-300 HU) was found to be significantly higher than the TGF-β-2w (**Figure 31 A**), TGF-β-3w (**Figure 31 B**) and TGF-β-4w (**Figure 31 C**) groups. In addition, the week 4 PF group was found to possess significantly more voxels than the HDMR group in the denser region (~-50 to 15 HU). The week 2 and 3 groups of the pulmonary fibrosis time points both had significantly more voxels in the very low density range on the left (~-700 to -550 HU).

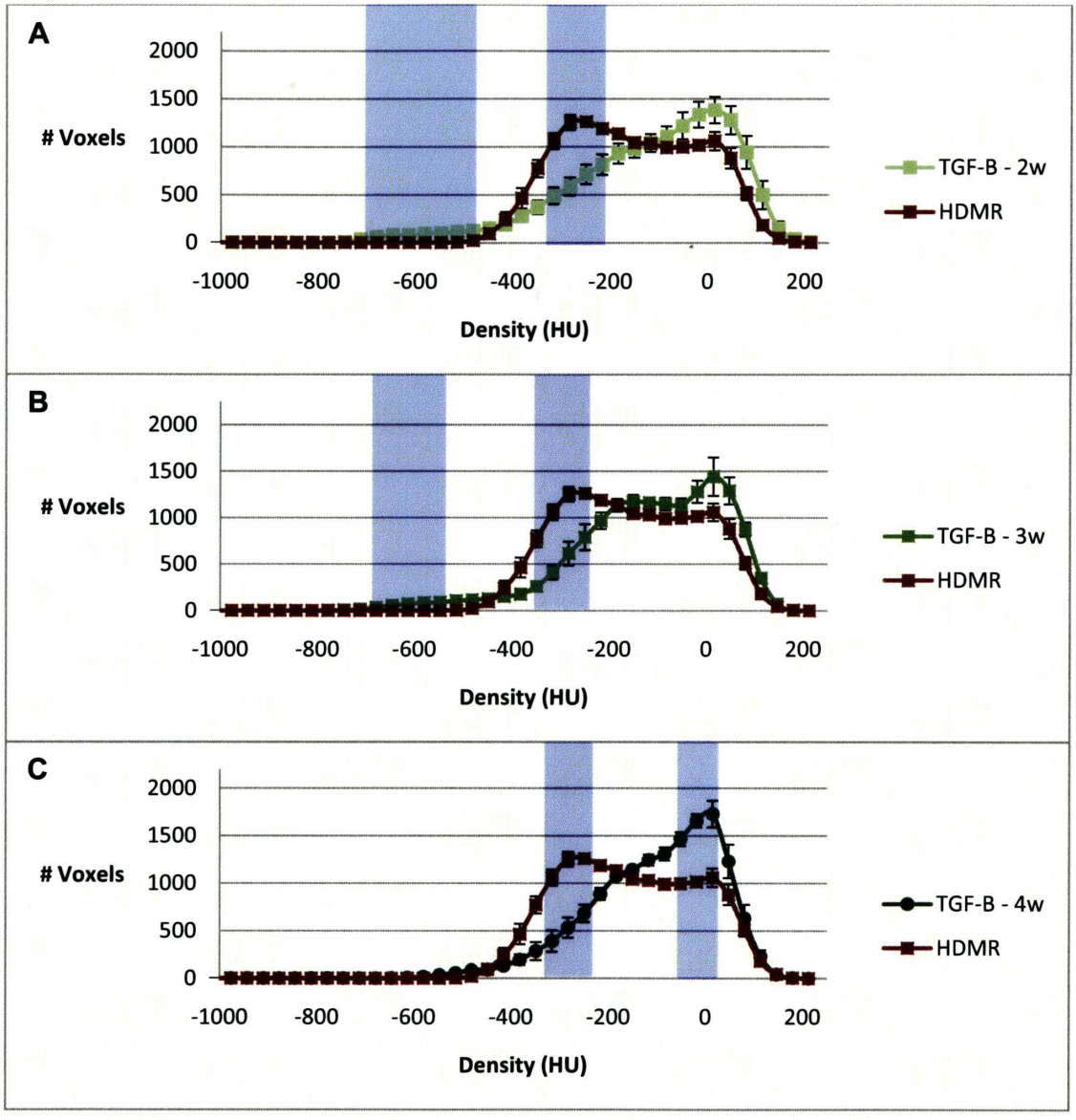

Figure 31. Comparative density distribution around selected large airways of the recovery group following chronic HDM exposure (HDMR) and PF models. These plots compare: (A) the asthma recovery group (HDMR) (n=6) to the pulmonary fibrosis group at 2 weeks (TGF-β-2w) (n=12); (B) 3 weeks (TGF-β-3w) (n=4); and (C) 4 weeks (TGF-β-4w) (n=5) following delivery of adTGF-β1. The plots demonstrate if a difference can be detected between the presence of fibrosis and the presence of only airway remodelling (HDMR). A one way ANOVA was performed at each bin. The blue boxes indicate regions of statistical significance ($P < 0.05$). Error is presented as SEM.

3.4.2 Asthma and Neutrophilic Inflammation Induced by LPS

Only the neutrophilic inflammation group at 24 h was compared to the three exposure groups from the asthma model since it was the only time point found to have significant inflammation compared to the control.

From the density distributions between neutrophilic inflammation (LPS – 24 h) and the acute (HDMA) (**Figure 32 A**), chronic (HDME) (**Figure 32 B**) and recovery (HDMR) (**Figure 32 C**) asthma models, only the HDMA and HDME group had regions which were significantly different from LPS group. The voxels in the HDMA group were shifted to the denser region with an elevated peak ~15 HU compared to the LPS group. This rightward shift in the HDMA group produced a region (~-400 to -300 HU) that has significantly less voxels compared to the LPS group. The HDME group had an even more pronounced increase in voxel frequency on the denser side (~50 HU) which was found to be significantly higher than the LPS group. This shift to the denser region produced an area with significantly fewer voxels than the LPS group in the lower density region (~-400 to -150 HU). It appears from these results that compared to the LPS group the HDMA group has a greater number of voxels in the denser region, and the HDME group had an even greater increase in voxels in the denser region. No differences were observed between HDMR and LPS.

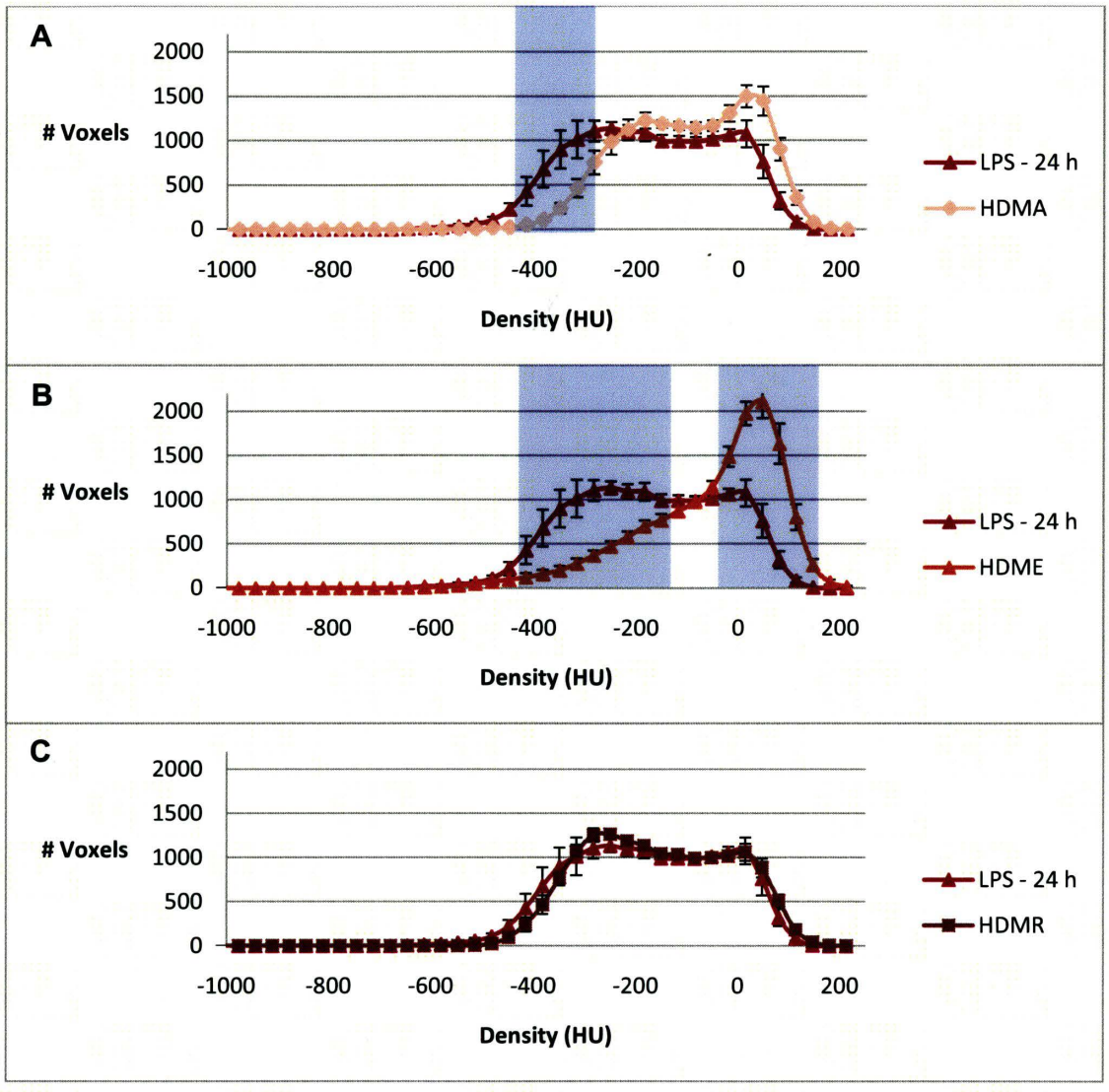

Figure 32. Comparative density distribution of selected large airways in mouse models of LPS induced neutrophilic inflammation and asthma. Plot (A) demonstrates if a difference can be detected between neutrophilic inflammation (LPS-24h) (n=7) and eosinophilic inflammation (HDMA) (n=6); (B) compares neutrophilic inflammation (LPS-24h) and eosinophilic inflammation and airway remodelling (HDME) (n=12); and (C) demonstrates if a difference can be detected between neutrophilic inflammation (LPS-24h) and airway remodelling (HDMR) (n=6). One way ANOVAs were performed at each bin comparing the exposure groups to each other. All points represent the mean values and SEM. The blue boxes indicate regions of statistical significance ($P < 0.05$).

3.4.3 Pulmonary Fibrosis and Neutrophilic Inflammation Induced by LPS

As previously mentioned, only the neutrophilic inflammation group at 24 hours (LPS-24h) after LPS exposure was compared to the three time points from the PF model since it was the only time point found to have significant inflammation compared to the controls. Compared to the 24 h post LPS group (LPS – 24 h) all three pulmonary fibrosis groups are shifted to the denser region on the right peaking at ~15 HU. This difference in density distributions between the PF and LPS plots produced a measureable region in the in the lower density range (~-300 HU) where the LPS group has significantly more voxels than the TGF-β-2w (**Figure 33 A**), TGF-β-3w (**Figure 33 B**) and TGF-β-4w (**Figure 33 C**) groups. In addition, the week 4 PF group was found to possess significantly more voxels than the LPS group in the denser region (~-150 to 15 HU). The week 2 and 3 groups of pulmonary fibrosis both had significantly more voxels in the very low density range on the left (~-700 to -550 HU). From these results it appears that the plots of the PF groups are all shifted to the denser region compared to the LPS group.

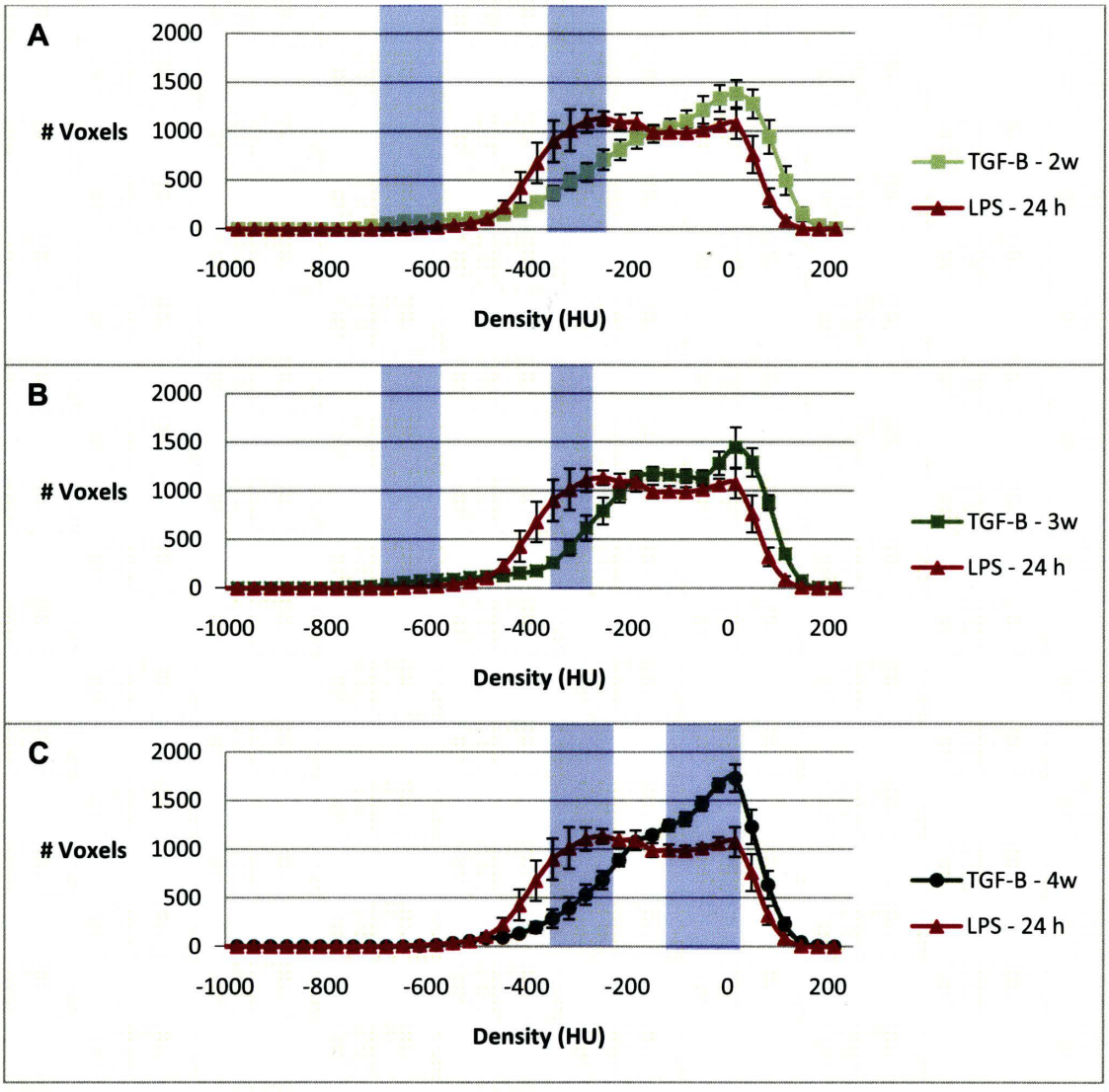

Figure 33. Comparative density distribution around selected large airways in mouse models of PF and LPS induced neutrophilic inflammation 24 hrs after LPS delivery. Plot A. compares 2 weeks after delivery of adTGFβ-1(TGF-β-2w) (n =12) and neutrophilic inflammation (LPS-24h) (n = 7); B. compares fibrosis at 3 weeks after delivery of adTGFβ-1(TGF-β-3w) (n = 4) and neutrophilic inflammation (LPS-24h); and C. compares fibrosis at 4 weeks after delivery of adTGFβ-1(TGF-β-4w) (n = 5) and neutrophilic inflammation (LPS-24h). All points represent the mean values and SEM. One way ANOVAs were performed at each bin comparing the exposure groups to each other. The blue boxes indicate regions of statistical significance ($P < 0.05$).

4 DISCUSSION

The objectives of this thesis were to determine if quantitative micro-CT was a sensitive measure of disease progression within disease models and could be used to distinguish between different pulmonary pathologies in mice. This was addressed by evaluating if quantifiable differences exist in the densitometry outputs using a novel large airway segmentation technique.

CT densitometry was used since visual interpretation of micro-CT images for preclinical studies is difficult due to the limited resolution capabilities of many micro-CTs employed in research. With this equipment pathologies that increase density will all appear as varying regions of high attenuation; whereas, in clinical imaging, increases in density can be characterized based on visible changes in density patterns (eg. honey combing, reticular changes, ground glass opacities). The same holds true for pathologies that cause a decrease in density. Quantitative CT appears to be the best way to distinguish between pathologies in animal models since density changes that are difficult to visualize can be measured from the CT data. Our study has shown that CT densitometry can distinguish diseased from healthy lungs, disease progression in asthma and LPS induced neutrophilic inflammation, and different lung pathologies can be detected, with each disease model having its own unique lung density profile

(**Figure 34**). This provides, for the first time, evidence that CT can be used to distinguish differences between pathologies in animal models of disease.

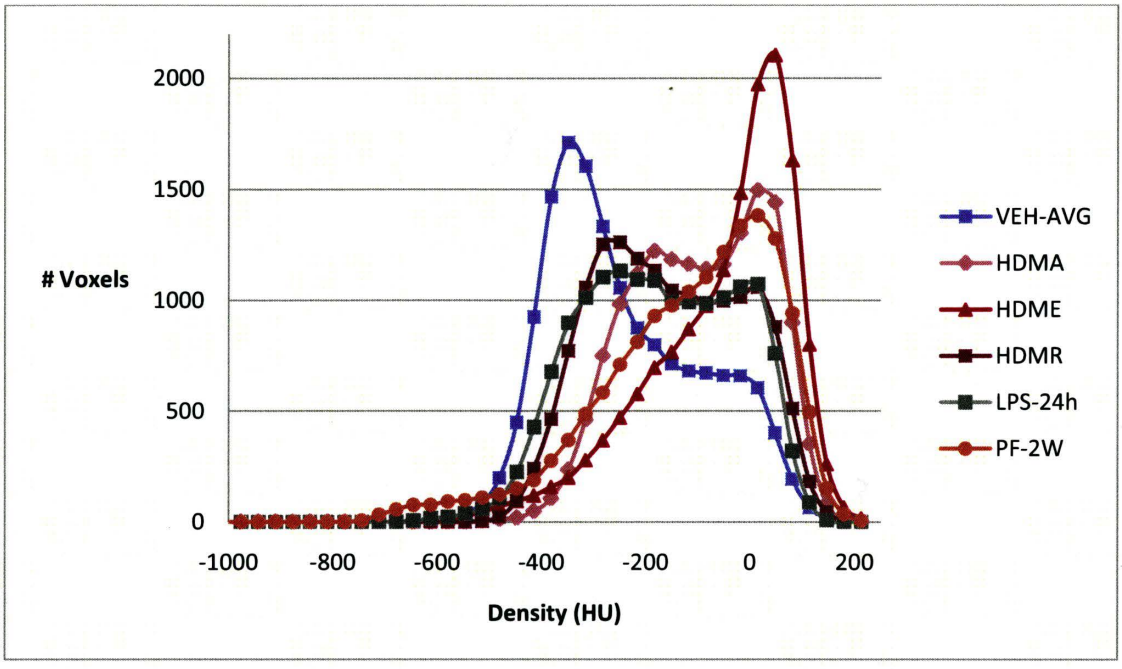

Figure 34. Summary of CT densitometry of PF, asthma and LPS disease models

Initially looking at each model compared to its control, our results showed a significant increase in density in the peribronchial region in the models of asthma, pulmonary fibrosis and LPS-induced neutrophilic inflammation. One would expect if either inflammation, remodelling or fibrotic tissue is present in the lung, an increase in the density range around 0 HU (equivalent to the density of water) or greater than 0 HU (tissues denser than water, eg. fibrosis) would accompany these pathologies. In the asthma models, significant differences were present in

all three examined disease states (acute, and chronic asthma, and recovery following chronic asthma) compared to controls. The overall density profiles were shifted to the denser region with an increase in the number of voxels around 0 HU especially in the acute and chronic asthma groups (peaking at 15 and 50 HU, respectively). The measured increase in density in each of the asthma models was associated with the presence of either peribronchial and perivascular eosinophilic inflammation (characterized as cellular infiltration in the H&E stained lung sections and measured by TCC and DCC from the BALF), airway remodelling (characterized by visible increases in smooth muscle deposition and goblet cell hyperplasia) or both. The histology and cytology outcomes of our disease models corresponded with results from Johnson and colleagues which showed the acute asthma group possessing peribronchial inflammation characterized by eosinophilia, the chronic asthma group possessing airway remodelling in addition to inflammation, and the recovery group which retained its airway remodelling and had no significant inflammation based on TCC (Johnson et al, 2004). However, in our recovery group histological images of the lungs expressed minimal peribronchial inflammation. In addition to histology and cytology, the asthma groups were also hyperresponsive to methacholine compared to controls, confirming that the asthma models were successfully recreated. Thus the presence of peribronchial inflammation, airway remodelling or both in the disease groups is readily distinguished from a non-inflamed healthy

lung using our CT densitometry methodology. The measured increases in density using CT in the acute and chronic asthma groups corresponded to outcomes reported in the literature. Quantitative CT measurements were used to assess density changes in the airways of a chronic asthma mouse model (Lederlin et al, 2010) and in the lung and thoracic regions of acute asthma models in rats (Jobse et al, 2009). In both cases the presence of pathologies due to either inflammation or both inflammation and airway remodelling produced either a higher regional airway density or a loss of airspace in the lung and an increase in more dense regions compared to controls (Lederlin et al, 2010; Jobse et al, 2009). The use of CT densitometry to quantify changes in a recovery model after chronic allergen delivery has not been published in literature thus far.

For the LPS group, neutrophilic inflammation was only markedly different from the controls at the 24 h time point at which cellular infiltration is also visible in the airspaces H&E stained lung slices. This corresponded to a flattening of the curve with a shift in voxel frequency to the denser region (-200 to 50 HU). The LPS 7h plot shape did not change, but it appeared to shift slightly to the denser region. With the rightward shift, there were regions in the LPS 7 h plot with voxel frequencies significantly greater (in the denser region (~50 HU)) and smaller (in the less dense region (~-400 HU)) than the control group. This may indicate the start of neutrophilic inflammation since neutrophils were present in the BALF at the 7 h time point, however, at this point the TCC was not significantly different

from the controls. The results at 7 and 24 hours after direct pulmonary exposure to LPS correspond to a previous study by Alm and colleagues which showed that TCC and neutrophils are present at 4 h; however, it is not statistically higher until 24 hrs after LPS delivery in BALB/c female mice (Alm et al, 2010). In addition to neutrophils, pulmonary edema will also be present. This would increase lung density as well as lung weight; however, lung weight was not measured (Alm et al, 2010). Future studies should measure changes in lung weight as a marker of pulmonary edema in order to correlate pulmonary density relative to edema since this likely has an effect on increasing lung density. At 2 weeks following delivery inflammation is absent (based on TCC, and DCC) and no pathological changes appear to be present in the lungs which corresponded to outcomes reported by Santos and colleagues who found 1 week after delivery of LPS the histology was no different from controls (Santos et al, 2006). The CT densitometry results correspond to the histology and cytology data, but could not be compared to the literature since no published data examines the use of CT densitometry for measuring acute neutrophilic inflammation in mice after exposure to LPS.

In the pulmonary fibrosis group, all three time points (PF-2W, 3W & 4W) produced plots which were shifted rightward towards the denser region and peaked around 0 HU compared to the control group which had a peak at -350 HU. The increase in overall density around the airways corresponded with the presence of fibrotic deposition around the airways and throughout the

parenchyma. Fibrosis was characterized by visual increases in fibrotic deposition and honeycombing of the parenchyma in the PSR stained lung slides. The presence of fibrosis at these time points corresponded to results reported in the literature (Rodt et al, 2010). In addition to histology, total cell counts were not found to be significantly different from controls and macrophages were the major cellular infiltrate, which was also reported in the literature (Warshamana et al, 2002). However, the sample size for histology and BAL sampling was too small to perform statistics at week 3 (n=2). The other two time points (2 & 4 weeks) had small sample sizes (n=3) so there may have been differences in TCC and DCC not detected. Elevated cell counts may be due to a high dose of the adTGF-β1, which has been reported to cause persistent cellular infiltration lasting up to 28 days following delivery, characterized by elevated macrophages (Warshamana et al, 2002). Nonetheless, the models appeared to be accurately created, and CT densitometry outputs of our airway segmentation protocol allows the detection of fibrosis in the PF disease animals compared to controls. This corresponds to results from the literature (Guerrero et al, 2007; Rodt et al, 2010). Hence, from the CT densitometry plots of the airway segmentations it appears that measurable density changes are associated with pathological changes such as fibrosis, inflammation, and airway remodelling, that are causing a shift to the denser region compared to the controls.

Longitudinal progression within the disease models was able to be quantified using the airway segmentation method when the disease model itself had pathological changes present, either pathological progression or resolution (for LPS). Within each model the density plots showed differences in plot shape and horizontal shift at the various time points, but not in the pulmonary fibrosis model. In the asthma model, pathological changes in the lung at the examined time points, which were confirmed from histology, were accompanied by alterations in shape and horizontal shift of the densitometry plots. The acute (HDMA) and chronic asthma (HDME) groups, and the recovery group (HDMR) all had regions which were found to be statistically different from each other. From histology the HDMA and HDME groups, both had eosinophilic inflammation and in the case of the HDME group, airway remodelling (characterized by smooth muscle and goblet cell hyperplasia). The measured density differences between the HDMA and HDME (with the HDME group having statistically higher voxel frequency in the range of 14.6 to 146.7 HU; and HDMA having a statistically higher voxel frequency in -282.6 to -117.5 HU range) may be due to the increased density from airway remodelling. The extent of inflammation (measured by total cell counts) in the HDME group is slightly higher, but not significantly different from the HDMA group. However, the TCC reflects cells in the entire lung, whereas, the airway segmentation is only measuring densities within a limited area. In the lung sections, the HDME group appeared to have increased regions of inflammation

around the airways compared to HDMA group. Thus, the sharp peak in the HDME plot could partly be due to a regional increase in inflammation around the airways (as seen in histological lung sections) compared to the HDMA group, in addition to the presence of airway remodelling. This needs to be determined by a quantitative assessment of inflammation in the lung sections. It is difficult to determine if inflammation has completely resolved in the HDMR group, since local peribronchial inflammation, although to a lesser extent than observed with HDMA and HDME, was visualized on lung sections. However, based on TCC there is no statistical difference in counts from controls. This should be validated by a quantitative assessment of regional inflammation from the lung sections to see if there is a local elevation in cells compared to controls. Between the HDMA and HDMR group, HDMR had significantly more voxels in the lower density range (~-350 to -250 HU). This would indicate a difference between the presence of eosinophilic inflammation (HDMA) causing a larger rightward shift to the denser region compared to airway remodelling only (HDMR). These results show that measurable differences between the acute, chronic and recovery asthma models are present using the airway segmentation method to analyze the CT data, thus suggesting CT is sensitive to pathological changes in asthma. In the literature the only study using micro-CT densitometry to assess a mouse asthma model, by Lederlin and colleagues, used a segmentation technique that was similar to our method. However, they only assessed density differences after chronic OVA

exposure (Lederlin et al, 2010). The only published study using CT densitometry in either mice or rats is by Jobse and colleagues, who measured longitudinal progression of inflammation within an acute asthma model of a rat at day 3, 7, and 10 after administration of HDM (Jobse et al, 2009). They found that peak density in this model occurred at 7 days due to peribronchial inflammation (Jobse et al, 2009).

In the LPS model, the CT densitometry plot of the LPS 24h group is clearly different from LPS 7h and 2w. The difference between LPS 24h and the other time points coincides with a significant increase in BALF TCC and neutrophils at 24 h. These results correspond to a previous study by Alm and colleagues which showed that TCC and neutrophils are elevated at 4 h and are statistically higher at 24 h in BALB/c female mice (Alm et al, 2010). In our study, the 7 h group did not have significant inflammation based on the TCC and this produced a density plot with a similar shape to the control group, but slightly shifted to the right. The likely difference between our 7 h outcome and the elevated TCC and neutrophils seen 4h after LPS delivery in the Alm study is that they used a ~10 fold higher LPS dose. The rightward shift may indicate a regional increase in inflammation which may not be detectable by TCC. Card and colleagues showed notable peribronchiolar and perivascular inflammation 6 h following delivery of a similar dose of LPS (Card et al, 2006), however, that was in C57BL/6 mice which have been shown to possess a heightened inflammatory response to LPS (Alm et al,

2010). In our LPS group, some inflammation was apparent in the 7 h lung sections. This cellular infiltrate was identified as neutrophils from the BALF. At two weeks following LPS delivery, inflammation had completely subsided based on the TCC and no neutrophils were present. The plot itself was found to be no different from the control group nor the LPS 7 h group. Based on these outcomes it appears the presence of or absence of statistically elevated neutrophilic inflammation is identifiable using airway density analysis.

The pulmonary fibrosis groups appeared to express similar TCC, and structural changes in the lung (determined from histology). These similarities were reflected in the density plots, which were absent of any measurable differences between the examined week 2, 3, and 4 time points. A study performed by Warshamana and colleagues indicated active fibrogenesis at 2 weeks after delivery of the adTGFβ-1 in C57BL/6 mice. This continued until 4 weeks when pathological progression appeared to resolve based on histopathology (Warshamana et al, 2002). Thus, further analysis of biochemical markers (eg. hydroxyl proline to test for collagen levels) or histomorphometry would be required to make any firm conclusions to whether or not alterations in fibrotic deposition are present at the different time points. Our results correlate with results found by Rodt and colleagues (Rodt et al, 2010). Using the same TGFβ-1 adenovirus vector they examined serial changes in the lung density of mice using micro-CT at 1, 2, 3, and 4 weeks after administering the vector.

Quantitative micro-CT was used to indirectly measure the extent of fibrosis by examining areas of aeration (Rodt et al, 2010). In addition, visual scoring of the extent of lung consolidation was performed. From these data they also were not able to detect significant differences between the time points (Rodt et al, 2010).

When comparing the disease models significantly distinct voxel frequencies were found between density regions in all disease models, suggesting the various pathologies have unique density profiles (**Figure 34**). In the LPS induced neutrophilic inflammation group peak neutrophilic inflammation occurred at 24 h following LPS delivery, producing a plot which is significantly different from the HDMA and HDME groups, but not the HDMR group. The HDMR and LPS-24 h groups appeared to be identical. These differences in the HDMA and HDME groups compared to LPS-24 h may be explained by the apparent differences in inflammation patterns noted in the lung sections. Based on lung histology the LPS group produced a more diffuse cellular infiltration throughout the lung while the HDMA and HDME groups had cells localized densely around the airways. We found that airway remodelling alone cannot be distinguished from neutrophilic inflammation using our segmentation method.

Increases in low density voxel frequency (~-600 HU) were present in the PF-2w and 3w groups compared to all asthma groups (HDMA, HDME and HDMR) and the LPS- 24 h group. An increase in voxel frequency in this region may indicate the expansion of an airspace or airway in response to an increase in

elastance in another region caused by fibrotic changes (Ask et al, 2008). This hypothesis corresponds to our results that airway diameter was statistically larger at 2 week PF time point compared to controls. In the PF-4w group elevated voxel frequencies in this region (~-600 HU) are not present, which may be due to the fact that the animals at this time point expressed less extensive fibrosis. The assumption that the PF-4w group expresses less fibrosis is based on the fact that it was largely comprised of a cohort who received the adTGFβ-1 by a slightly altered delivery method. This possibly caused these animals to have less of the adTGFβ-1 reach the lungs than at the other time points. Dosing variation of adTGFβ-1 has been reported to alter the extent and rate of fibrotic progression in C57BL/6 mice (Warshamana et al, 2002). In addition, Lee and colleagues demonstrated that peripheral bronchial dilation measured from micro-CT images showed good correlation with the extent of fibrogensis (rated using a histopatholgical score). Thus increased airway space (indicated by low density voxel frequency) may represent more extensive fibrosis (Lee et al, 2008). Further analyses comparing the airway diameters of the PF-4w group to the PF-2w groups and a histomorphometric analysis of fibrosis should be performed to confirm this hypothesis.

Looking at the denser region ~0 HU, there are only marked increases in voxel frequency in the HDME group compared to all three PF time points (PF-2w, PF-3w, PF-4w). This increase in voxel frequency at 0 HU in the HDME group

indicates that eosinophilic inflammation in conjunction with airway remodelling produces a distinctly different plot from all pulmonary fibrosis groups. Compared to the HDMR and LPS-24 h groups the voxels in the PF groups are all shifted towards the denser region. This shift in the PF groups produces greater voxel frequencies in the denser region (~0 HU) compared to both HDMR and LPS-24 h. However, voxel frequency to the PF groups was only measured to be significantly higher in the PF-4w group compared to HDMR and LPS-24 h. Surprisingly, in the denser region (~0 HU) no density differences were noted between the PF groups and HDMA apart from a single bin that had fewer voxels than the PF-4w group (~-50 HU).

From these results it appears that the chronic asthma model (HDME) can be differentiated from the pulmonary fibrosis model at all time points using this segmentation method. However, the acute asthma model (HDMA) is not as easily distinguished from the PF time points. The HDMA results are similar to the recovery asthma group (HDMR) and LPS-24h group, however, these groups appear to present densitometry profiles that were relatively less dense producing regions which were statistically different from the PF groups. Thus, it appears that all PF groups can all be easily distinguished from HDME and HDMR, and LPS-24h using CT densitometry alone. Although no statistical differences were found between the density plots of the three PF groups, there appears to be some variation in the comparative densitometry specifically between the PF-2w & 3w

and the PF-4w groups. Further, analysis of the lung sections, such as histomorphometry is required to assess if differences in fibrogenesis are present between the PF time points.

Visual examination of the CT images revealed increases in regions of high attenuation around the airways in all time points in the asthma and pulmonary fibrosis models, and at the 24h time point after delivery of LPS. These outcomes correspond with the results of previous studies (Lederlin et al, 2010; Rodt et al, 2010) as well as the presence of increased cell counts and/or visible pathological changes in histology. Given the image resolution capabilities of the micro-CT we used, the number of projections taken, and the voxel size of 115 μm, it is difficult if not impossible to use visual interpretation to identify and grade pathological processes present in the lung without the associated histology.

In this study the micro-CT densitometry of the large airway region was compared in female BALB/c and C57BL/6 mice with ages ranging from 12 weeks to 24 weeks in age. To ensure that variability in the density profiles was not due to the strain or age of the mice, density differences between the control mice were compared. Differences in the models were determined not to be due to mouse strains (BALB/c and C57BL/6), age (12 weeks to 24 weeks) or failure to reproduce the animal models (which were validated from histology and physiology for the asthma model). An analysis of the control density plots from

the airway segmentations of mice between age groups and strain show no significant differences (**Appendix, Figure 45** & **Figure** 46).

Since the airway lumen was included in the airway segmentation analyses of airway diameters were performed in the acute and chronic asthma models, and in the pulmonary fibrosis group. The analysis of the lumen diameter showed that there are no significant differences between the airway diameters in the asthma models compared to the control animals. These results correlate with data found by Lederlin and colleagues, who found no difference in the airway lumen areas derived from micro-CT images in murine models of chronic asthma (Lederlin et al, 2010). Therefore, in the asthma group, changes in density were assumed to be associated primarily with the parenchyma, airway walls and surrounding tissues in the peribronchial area. For the pulmonary fibrosis group an increase in airway diameter at the measured time point (2w) was noted compared to controls. These results correlate to finding by Lee and colleagues which found that the presence of fibrosis is associated with peripheral bronchial dilation (Lee et al, 2008).

5 LIMITATIONS OF STUDY

There are a number of potential limitations of this study; one of them is the segmentation protocol itself. Although it has been found to be an efficient way to distinguish the presence of pathologies the segmentation is limited to describing

changes only around the airways. The large airway segmentations were specifically created for this thesis in order to have a reproducible method that could be used in all animal models after analysis of the thoracic segmentation was found to be insensitive to density changes (data not shown). Furthermore, a lung segmentation method used in certain preclinical studies on mice (using the threshold range if -100 to -990 HU) (Guerrero, et al, 2007) could not extract the whole lung region in all models due to the presence of pathologies within and around the airways which caused increased lung density (>-100 HU). This prevented inclusion of regions of interest which were highly fibrotic or inflamed. Since our intent was to quantify these pathologies and not exclude them, the airway segmentation was deemed the best method as all disease models had been previously reported to express peribronchial pathologies in varying degrees (Card et al, 2006; Johnson et al, 2004; Kolb et al, 2002); and this was visually determined to be present in our models from the micro-CT images.

Another potential limitation of the segmentation is that it was created by manual selection. This introduces a certain degree of user subjectivity in the region of interest, as well as possible variation in the region chosen between the animals themselves, although anatomical landmarks were used. Furthermore, it does not contribute to the goal of using CT densitometry to eliminate observer subjectivity present in visual assessment of CT images. Another limitation was the degree of variability apparent in the pulmonary fibrosis animals (**Appendix**,

Figure 47) with peak voxel frequency occurring at -300 to 50 HU. This variability was visually confirmed in the CT images (data not shown). The likely cause of this variability in CT densities is that altered amounts of adTGF-β were delivered to the lungs and hence subsequent inconsistent development of fibrosis and possibly elevations in macrophage infiltration may have been present. The adTGF-β was delivered using different IT methods. The dosage remained consistent, but the anaesthetic, device and delivery technique used were altered due to low survival rates of the first two groups. Due to this, it is believed that the first two groups received a higher dose with the more efficient intratracheal delivery technique. Warshamana and colleagues have shown that increasing the dose of adTGF-β in mice produce an early onset of fibrotic deposition and persistent inflammation, seen up to 28 days after delivery (Warshamana et al, 2002). Thus, dosing changes between groups and within groups could produce the variability noted in our data. To control for variability in the airway segmentations, outliers were removed from the final grouped analysis. The data was considered an outlier based initially on CT densitometry plots and then visual confirmation of the histology slides. This same degree of variability was not noted in the asthma and LPS data.

In addition, since the airway segmentation represents a small portion of the entire lung, whole lung measurements such as TCC and pulmonary resistance may not correlate to regional density changes, and pathological changes in the

rest of the lung will be excluded. This may be of concern for our models since regional differences have been reported in murine models of asthma. Wegmann and colleges found that acute asthma protocols have shown proximal inflammation whereas chronic protocols of aerosolized OVA delivery have been shown to contain both proximal and distal inflammation (Wegmann et al, 2005). Regional changes in pathologies have also been noted in the pulmonary fibrosis model created by adTGF-β. It has been reported that fibrogenesis starts at the delivery site (the airways) and then spreads throughout the parenchyma (Warshamana et al, 2002). Longitudinal studies trying to assess fibrotic development will likely not be amenable to measurements by the airway segmentation method once fibrotic progress spreads beyond the finite region of interest. However measuring density changes in the airways may describe another characteristic of the disease such as increased airway resistance. Thus, the intended use of this method must be considered with these limitations in mind when planning future studies.

Another limitation to the study is our method employed to perform the statistical analyses. This method examined differences in plots on a bin by bin basis. Previous studies have used an average value such as relative area (RA), which examines changes in density within a specific density range. For example, RA has been employed in clinical studies to stage COPD by measuring the number of voxels in the range of -950 HU and smaller (Akira et al, 2009) and -

450 HU in pre-clinical studies of emphysema in mice (Froese et al, 2007). A RA-type analysis was initially performed on our airway segmentations. No published target density (like -950 HU for COPD in humans or -450 HU for mice) exists for animal models of asthma, PF, or LPS, so a cumulative plot of the baseline CT histogram data was created (**Appendix, Figure 48**). The density at which 50% of the voxels in the airway segmentation were found in a healthy lung was chosen, which was -249.5 HU. Using this value an RA measurement was performed from -249.5 HU and greater. This was useful for determining if pathologies are present within asthma, LPS and pulmonary fibrosis groups; however it was not useful for distinguishing between pathologies (**Appendix, Figure 49** Figure **51**). The shapes of many of the curves in the different models have unique profiles. To assess the shape of the curve, our method examined differences in plots on a bin by bin basis instead of using an average value like RA. This method was time consuming, and did not produce a value that could then be correlated to pathological changes. However, it was able to distinguish between the different pathologies which produce increased attenuation in the lungs when a common densitometry parameter like relative area (RA) could not.

Our study demonstrated the importance of the plot shape for describing the presence of lung pathologies. This was previously reported by Hiromitsu, and colleagues; they found that the shape of the histogram from lung segmentation was characteristic of the pathologies present (Hiromitsu et al, 2009). An example

of this is the incorporation of plot shape descriptors such as measurements of skewness and kurtosis, in addition to more common measurements such as MLA, to better describe pathological progression in clinical CT studies of idiopathic pulmonary fibrosis (Best et al, 2008). Another branch of research is trying to take advantage of the different density patterns produced by pathologies in order to better characterize a disease state. This is called texture analysis and it applies pattern recognition algorithms to describe CT data and is able to characterize instances of fibrosis compared to inflammation, however, this research is currently in its infancy (Zavaletta, Bartholmai, and Robb, 2007).

Finally, using micro-CT for quantitative assessment will be bound to present a certain amount of variation in the HU values of the air and water standards (Levi et al, 1982). The standards of air and water used to convert the attenuation values to HU for this thesis have been shown to have standard deviations of 50 to 100 HU respectively (data not shown). Thus, if significant differences are measured over a region spanning two bins or less (~66 HU) it is difficult to make any confident claims of significance. Nonetheless, since many of the regions were greater than 2 bins in width the horizontal variability of density values does not diminish the validity of our outcomes.

6 CONCLUSIONS

Using our method of airway segmentation it is possible to distinguish between a healthy and a diseased lung in all three murine pulmonary disease models of asthma, PF and neutrophilic inflammation induced by LPS. The examined regions around the airways showed altered density patterns with a shift to the denser region. Pathological changes, such as the progression of asthma from the acute to chronic model, and the resolution of eosinophilic inflammation, and the development and resolution of a neutrophilic inflammation by LPS, can also be assessed using this method. No changes were seen in the PF group and this correlated with histological findings, however, further analysis needs to be done in order to confirm that fibrotic changes were similar between the PF time points. This method of analysis affords a non-invasive way to assess disease progression longitudinally which will be useful for the testing of novel therapeutics to assess resolution of pathologies over time within the same subject. With this analysis it appears that it is also possible to distinguish between many of the pathologies based on the density profiles alone, which could not be seen by thoracic segmentation (data not shown). This is one of the benefits of the regional CT density assessment, allowing the detection of localized pathologies around the airways which whole lung assessments may not be sensitive enough to detect. Applications of this study should include focusing on regional differences in the plots which are unique to each disease model. These can be used to develop standard assessment methods like those that already exist in human CT

densitometry studies of COPD (eg. measuring the RA using the threshold value of -950 HU).

7 FUTURE DIRECTIONS

Given the available equipment and software, the airway segmentation method was the best method for the purposes of this study. The results of this segmentation have shown that there are specific regions of interest that appear to be characteristic of the certain pathologies; for example, the increase in the region ~-600 HU in the early fibrosis group time points (week 2 and 3), or the very large peak ~50 HU that is present in the chronic asthma model. These outcomes now need to be addressed to develop a method of assessing the data in a more disease focused way. Since this thesis covers a range of pathologies there are many disease specific applications of this model; however, no one quantitative CT method can best describe all disease models. Future studies should include a longitudinal assessment with a dose response component to see if this quantitative CT method can detect differences in the degree of pathologies present over time. In the literature, alterations in degrees of cellular infiltration and the temporal development of fibrosis have been noted in murine models of PF (Washamana et al, 2002). Furthermore, the extent of edema and inflammation has also been shown to increase with increasing dose of LPS (Alm, et al, 2010), and CT densitometry has been able to quantify differences in rat models of acute asthma produced by varying HDM doses using a lung

segmentation (Jobse et al, 2009). In addition, the airway segmentation method should continue to be developed on individual disease bases to find a standard density threshold (or range of values) characteristic of that particular pathology. Finding a standardized density range to characterize pathologies would be useful for disease identification and/or measuring disease progression. This has been previously reported in human studies of COPD. In clinical studies examining COPD by CT densitometry, -950 HU was found to be the ideal threshold to measure RA in order of detect emphysematous regions and this was found to correlate with disease progression (Akira et al, 2009). Using our airway segmentation method regions that could be further explored include the very low density range <-350 HU in the pulmonary fibrosis group which might indicate increased fibrosis (leading to airway expansion); or for asthma, changes around 0 HU might describe increased peribronchial inflammation.

Since the airway segmentation only describes a limited region further investigation quantifying localized pathological changes need to be performed. So far, the only quantitative measurements on a regional scale are from the CT densitometry plots. TCC may not necessarily correlate with regional density changes being measured within the segmentation. For example, visible differences in the extent of peribronchial inflammation were seen in lung sections between the HDMA and HDME groups even though TCC were found to be no different. In addition, the TCC of the recovery group, which were previously

reported to be no different from controls, still appeared to possess elevated peribronchial cellular infiltration compared to controls (present in histology), which is possibly a sign of local inflammation around the airways. Cases of persistent inflammation have been previously reported. Wegmann and colleagues found that inflammation remained significantly higher than controls at 6 weeks of recovery from their model of chronic asthma (Wegmann et al, 2005). Our TCC results correlate with the findings of a study by Johnson and colleagues that found (using a very similar asthma protocol) that at 2 and 4 weeks after cessation of HDM delivery, TCC was not significantly higher than controls, although they are slightly elevated (Johnson et al, 2004). In this case representative histology was not presented. Thus, no definite conclusion can be made concerning the cause of the plot differences until further analysis is performed such as histomorphometry examining the extent of peribronchial inflammation between HDMA and HDME. The same should be applied for the LPS 7 h group and 24 h group since there could possibly be a localized increase in cell around the airways at 7 h after delivery since neutrophils were detected and the CT densitometry plot expressed a slight shift to the denser region.

Other methods of statistical analysis should be explored. Descriptors of the plot shift and shape (skewness and kurtosis) have been shown to be useful in clinical CT studies of pulmonary fibrosis (Best et al, 2008). However, our segmentation produces plots which in some cases are bimodal so these are not

easily applied to our data. One possible solution is using a multiple normal distribution curve fitting program designed by Professor P. MacDonald (Department of Mathematics & Statistics, McMaster University). This produces a curve fit to the frequency plot using any multiple number of normal distribution curves to accurately describe the data; an example of a HDMA control is seen in (**Figure 35**). This plot gives a mean of each normal curve and the SD, goodness of fit, and the percentage of area taken up by each curve, providing outcome measurements which describe the plots' shape.

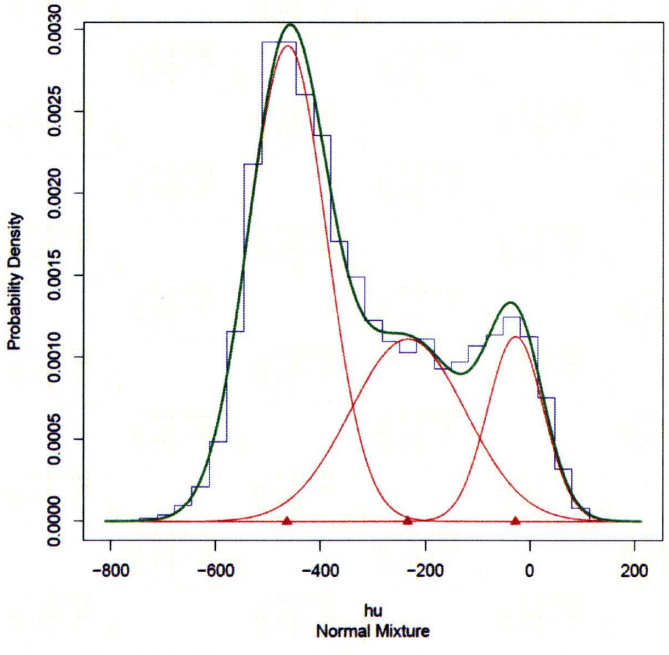

Figure 35. Mixed normal distribution curve fitting to large airway segmentation in a mouse. The frequency plot (blue) represents the density distribution of voxels in one animal acutely exposed to HDM (HDMA – AA01). The red curves indicate the three normal distributions with means centered at the red arrows. The resulting fitted curve appears in green.

8 BIBLIOGRAPHY

Akira, M., Toyokawa, K., Inoue, Y., & Arai, T. (2009). Quantitative CT in Chronic Obstructive Pulmonary Disease: Inspiratory and Expiratory Assessment. *Cardiopulmonary Imaging*. AJR 192:267-272

Allen, J.E., Bischof, R.J., Chang, H-Y. S., Hirota, J.A., Hirst, S.J., Inman, M.D., Mitzner, W. & Sutherland, T.E. (2009). Animal Models of Airway Inflammation and Airway Smooth Muscle Remodelling in Asthma. *Pulmonary Pharmacology & Therapeutics*, *22*, 455-465

Alm, A.S., Li, K., Chen, H., Wang, D., Andersson, R., & Wang, X. (2010). Variation of Lipopolysaccharide-Induced Acute Lung Injury in Eight Strains of Mice. *Respiratory Physiology & Neurobiology* 171(2): 157-164

Ahn, J.H., Kim, C.H., Kim, S.J., Lee, S.Y., Kim, Y.K., Kim, K.H., Moon, H.S., Song, J.S., Park, S.H., & Kwon, S.S. (2007). Inflammatory and Remodeling Events in Asthma with Chronic Exposure to House Dust Mites: A Murine Model. *Journal of Korean Medical Science, 22(6)*, 1026-1033

Artaechevarria, X, Pérez-Martin, D., Ceresa, M., de Biurrun, G., Blanco, D., Montuenga, L.M., van Ginneken, B., Ortiz-de-Solorzano, C. & Muñoz-Barrutia, A. (2009). Airway Segmentation and Analysis for the Study of Mouse Models of Lung Disease Using Micro-CT. *Physics in Medicine and Biology, 54*, 7009-7024

Artaechevarria, X., Blanco, D., de Biurrun, G., Ceresa, M., Pérez-Martin, D., Bastarrika, G., de Torres, J.P., Zulueta, J.J., Montuenga, L.M., Ortiz-de-Solorzano, C. &

Munoz-Barrutia, A. (2010). Evaluation of Micro-CT for Emphysema Assessment in Mice: Comparison with Non-Radiological Techniques. *European Society of Radiology, epub*

Ask, K., Labiris, R., Farkas, L., Moeller, A., Froese, A., Farncombe, T., McClelland, G.B., Inman, M., Gauldie, J. & Kolb, M.R.J. (2008). Comparison Between Conventional and "Clinical" Assessment of Experimental Lung Fibrosis. *Journal of Translational Medicine, 6* (16), 1-10

Auffray, C., Adcock, I.M., Chung, K.F., Djukanovic, R., Pison, C., & Sterk, P.J. (2010). An Integrative Systems Biology Approach to Understanding Pulmonary Diseases. *American College of Chest Physicians, 137*, 1410-1416

Best, A.C., Lynch, A.M., Bozic, C.M., Miller, D., Grunwald, G.K., & Lynch, D.A. (2003). Quantitative CT Indexes in Idiopathic Pulmonary Fibrosis: Relationship with Physiologic Impairment. *Radiology*, *228*, 407-414

Best, A. C., Meng, J., Lynch, A.M., Bozic, C.M., Miller, D., Grunwald, G.K., & Lynch, D.A. (2008). Idiopathic Pulmonary Fibrosis: Physiologic Tests, Quantitative CT Indexes, and CT Visual Scores as Predictors of Mortality. *Radiology, 246*(3), 935-940

Boehm, H. F., Fink, C., Attenberger, U., Becker, C., Behr, J. & Reiser, M. (2008). Automated Classification of Normal and Pathologic Pulmonary Tissue by Topological Texture Features Extracted from Mult-Detector CT in 3D. *European Society of Radiology, 18 (12)*, 2745-2755

Bonniaud, P., Margetts, P.J., Ask, K., Flanders, K., Gauldie, J., & Kolb, M. (2005). TGF-β Smad 3 Signaling Link Inflammation to Chronic Fibrogenesis. *Journal of Immunology, 8*, 5390-5395

Bogaert, P., Tournoy, K.G., Naessens, T., & Grooten, J. (2009). Where Asthma and Hypersensitivity Pneumonitis Meet and Differ. *The American Journal of Pathology, 174*(1), 3-13

Bousquet. J., Jeffery, P.K., Busse, W.W., Johnson, M., & Vignola, A.M. (2000). Asthma. From Bronchoconstriction to Airways Inflammation and Remodelling. *American Journal of Respiratory Critical Care Medicine, 161(5)*, 1720-1745

Bozinovski, S., Jones, J., Beavitt, S.-J., Cook, A.D., Hamilton, J.A., & Anderson, G.P. (2004). Innate Immune Response to LPS in Mouse Lung are Suppressed and Reversed by Neutralization of GM-CSF via Repression of TLR-4. *American Journal of Physiology, 286*(4), L877-L885

Brass, D. M., Tomfohr, J., Yang, I. V., & Schwartz, D. A. (2007). Using Mouse Genomics to Understand Idiopathic Interstitial Fibrosis. *Proceedings of the American Thoracic Society, 4*, 92-100

Card, J. W., Carey, M.A., Bradbury, J.A., DeGraff, L.M., Morgan, D.L., Moorman, M.P., Flake, G.P. & Zeldin, D.C. (2006). Gender Differences in Murine Airway Responsiveness and Lipopolysaccharide-Induced Inflammation. *The Journal of Immunology, 177*(1), 621-630

Cavanaugh, D., Travis, E.L., Price, R. E., Gladish, G., White, A., Wang, M., & Cody, D. Quantification of Bleomycin-Induced Murine Lung Damage In Vivo with Micro-Computed Tomography. *Academic Radiology*, *13*(12), 1505-1512

Cavigli, E., Comiciottoli, G., Diciotti, S., Orlandi, I., Spinelli, C.,. Meoni, E., Grassi, L., Farfalla, C., Pistolesi, M.,Falaschi, F. & Mascalchi, M. (2009). Whole-Lung Densitometry Versus Visual Assessment of Emphysema. *European Radiology, 19,* 1686-1692

Cheng, I., Nilufar, S., Flores-Mir, C., & Basu, A. (2007). Airway Segmentation and Measurement in CT Images. Proceedings of the 29th Annual International Conference of the Institute of Electrical and Electronic Engineers

Chung, J.H., Kradin, R.L., Greene, R.E., Shepard, J.-A.O., & Digumarthy, S.R. (2010). CT Predictors of Mortality in Pathology Confirmed ARDS. *European Radiology, epub*

Cormack, A.M. (1973). Reconstruction of Densities from their Projections, with Applications in Radiological Physics. *Physics in Medicine and Biology*, *18* (2), 195-207

Coxson, H. O. (2008). Quantitative Computed Tomography Assessment of Airway Wall Dimensions: Current Status and Potential Applications for Phenotyping Chronic Obstructive Pulmonary Disease. *Proceedings of the American Thoracic Society, 5*, 940-945

Coxson, H. O. & Rogers, R. M. (2005). Quantitative Computed Tomography of Chronic Obstructive Pulmonary Disease. *Academic Radiology, 12*(11), 1457-1463

Dobbins, J.T. & Godfrey, D.J. (2003). Digital X-Ray Tomosynthesis: Current State of the Art Clinical Potential. *Physics in Medicine and Biology, 48*, R65-R106

Einfeld, D.A., Schroeder, R., Roelvink, P.W., Lizonova, A., King, C.R., Kovesdi, I., & Wickham, T.J. (2001). Reducing Native Tropism of Adenovirus Vectors Requires Removal of Both CAR and Integrin Interations. *Journal of Virology,75*(23), 11284-11291

Ertel, D., Kyriakou, Y., Lapp, R. M., & Kalender, W. A. (2009). Respiratory Phase-Correlated Micro-CT Imaging of Free-Breathing Rodents. Physics in Medicine and Biology, *54*, 3837-3846

Fahy, J.V. (2008). Eosinophilic and Neutrophilic Inflammation in Asthma. *Proceedings of the American Thoracic Society, 6,* 256-259

Farncombe, T.H. (2008), Software-based Respiratory Gating for Small Animal Conebeam CT. *Medical Physics, 35*, 1785-1792

Ford, N.L., Martin, E.L., Lewis, J.F, Veldhuizen, A.W., Drangova, M., & Holdsworth, D.W. (2007). In Vivo Characterization of Lung Morphology and Function in Anesthetized Free-Breathing Mice Using Micro-Computed Tomography. *Journal of Applied Physiology, 102*, 2046-2055

Ford, N.L., Thornton, M.M., & Holdworth, D.W. (2003). Fundamental Image Quality Limits for Microcomputed Tomography in Small Animals. *American Association of Medical Physics, 30*(11), 2869-2877

Froese, A.R., Ask, K., Labiris, R., Farncombe, T., Warburton, D., Inman, M.D., Gauldie, J. & Kolb, M. (2007). Three-Dimensional Computed Tomography Imaging in an Animal Model of Emphysema. *European Respiratory Journal, 30*, 1082-1089

Fulkerson, P.C., Rothenberg, M.E. & Hogan, S.P. (2005). Building a Better Mouse Model: Experimental Models of Chronic Asthma. *Clinical and Experimental Allergy* 35: 1251-1253

Galani, V., Tatsaki, E., Bai, M., Kitsoulis, P., Lekka, M., Nakos, G., & Kanavaros, P. (2010). The Role of Apoptosis in the Pathophysiology of Acute Respiratory Distress Syndrome (ARDS): An Up-to-date Cell-specific Review. *Pathology – Research and Practice, 206*, 145-150

Gauldie, J., Bonniaud, P., Sime, P., Ask, K., & Kolb, M. (2007). TGF-β, Smad3 and the process of progressive fibrosis. *Biochemical Society Transactions, 35*(4), 661-664

Global Initiative for Asthma (GINA). (2009). Global Strategy for Asthma Prevention and Management. 1-26

Glaab, T., Taube, C., Braun, A., & Mitzner, W. (2007). Invasive and Noninvasive Methods for Studying Pulmonary Function in Mice. *Respiratory Research, 8*(63), 1-10

Goris, M.L., Zhu, H.J., Blankenberg, F., Chan, F., & Robinson, T.E. (2003). An Automated Approach to Quantitative Air Trapping Measurements in Mild Cystic Fibrosis. *Chest, 123*(5), 1655-1663

Graham, F.L. & Prevec, L. (1991). Manipulation of Adenovirus Vectors. Method of Molecular Biology. *Gene Transfer and Expression Protocols, 7*. E.J. Murray and J.M. Walker, eds. Humana Press Inc., Clifton, NJ, 109-111

Grenier, P., Mourey-Gerosa, I., Benali, K., Brauner, M. W., Leung, A. N., Lenoir, S., Cordeau, M.P. & Mazoyer, B. (1996). Abnormalities of the Airways and Lung Parenchyma in Asthmatics: CT Observations in 50 Patients and Inter- and Intraobserver Variability. *European Radiology, 6*, 199-206

Gross, T.J. & Hunninghake, G.W. (2001). Idiopathic Pulmonary Fibrosis. *New England Journal of Medicine: Review Article, 345*, 517-525

Guerders, M.M., Paulissen, G., Crahay, C., Quesada-Calvo, F., Hacha, J., Van Hove, C., Tournoy, K., Louis, R., Foidart, J.M., Noël, A. & Cataldo, D.D. (2009). Mouse Models of Asthma: A Comparison Between C57BL/6 and BALB/c Strains Regarding Bronchial Responsiveness, Inflammation, and Cytokine Production. *Inflammation Research, 58(12)*, 845-854

Guerrero, T., Castillo, R., Noyola-Martinez, J., Torres, M., Zhou, X., Guerra, R., Cody, D., Komaki, R. & Travis, E. (2007). Reduction of Pulmonary Compliance Found with High-Resolution Computed Tomography in Irradiated Mice. *International Journal of Radiation Oncology Biology Physics, 67(*3), 879-887

Gupta, S., Siddiqui, S., Haldar, P., Entwisle, J.J., Mawby, D., Wardlaw, A.J., Bradding, P., Pavord, I.D., Green, R.H., & Brightling, C.E. (2010). Quantitative Analysis of High-resolution Computed Tomography Scans in Severe Asthma Subphenotypes. *Thorax 65*, 775-781

Haegens, A., Heeringa, P., van Suylen, R.J., Steele, C., Aratani, Y., O'Donoghue, R.J., Mutsaers, S.E., Mossman, B.T., Wouters, E.F., & Vernooy, H.J. (2009). Myeloperoxidase Deficiency Attenuates Lipopolysaccharide-induced Acute Lung Inflammation and Subsequent Cytokine and Chemokine Production. *Journal of Immunology, 182*(12), 7990-7996

Heremans, A., Verschakelen, J.A., Van fraeyenhoven, L., & Demedts, M. (1992). Measurement of Lung Density by Means of Quantitative CT Scanning: A Study of Correlations with Pulmonary Function Tests. *Chest, 102(3)*, 805-811

Hirota, J.A., Budelsky, A., Smith, D., Lipsky, B., Ellis, R., Xiang, Y.Y., Lu, W.Y., & Inman, M.D. (2010). The Role of interleukin-4R Alpha in the Induction of Glutamic Acid Decarboxylase in Airway Epithelium Following Acute House Dust Mite Exposure. *Clinical & Experimental Allergy*, *40*(5), 820-830

Hounsfeld, G.N. (1973). Computerized Transverse Axial Scanning (Tomography): Part 1. Description of System. *British Journal of Radiology, 46*, 1016-1022

Hsia, C.C.W., Hyde, D.M., Ochs, M., & Weibel, E.R. (2010). An Official Research Policy Statement of the American Thoracic Society/European Respiratory Society:

Standards for Quantitative Assessment of Lung Structure. *American Journal of Respiratory and Critical Care Medicine, 181*, 394-418

Inman, M.D. (2010). Trends and Recommendations in Studies of Mouse Airway Function. *Clinical & Experimental Allergy, 40*, 524-527

Jansson, A.H., Eriksson, C., & Wang, W. (2004). Lung Inflammatory Responses and Hyperinflation Induced by an Intratracheal Exposure to Lipopolysaccharide in Rats. *Lung, 182*, 163-171

Jobse, B.N., Johnson, J.R., Farncombe, T.H., Labiris, R., Walker, T.D., Goncharova, S. & Jordana, M. (2009). Evaluation of Allergic Lung Inflammation by Computed Tomography in a Rat Model In Vivo. *European Respiratory Journal,* 33, 1437-1447

Johnson, K. A. (2007). Imaging Techniques for Small Animal Imaging Models of Pulmonary Disease: Micro-CT. *Toxicologic Pathology, 35*, 59-64

Johnson, J.R., Wiley, R.E., Fattouh, R., Swirski, F.K., Gajewska, B.U., Coyle, A.J., Gutierrez-Ramos, J-C., Ellis, R., Inman, M.D. & Jordana, M. (2004). Continuous Exposure to House Dust Mite Elicits Chronic Airway Inflammation and Structural Remodelling. *American Journal of Critical Care Medicine, 169*, 378-385

Junqueira, L.C.U., Bignolas, G., & Brentani, R.R. (1979). Picrosirius Staining Plus Polarization Microscopy, a Specific Method for Collagen Detection in Tissue Sections. *Histochemical Journal, 11*, 447-455

Kalender, W. A. & Kyriakou, Y. (2007). Flat-Detector Computed Tomography (FD-CT). European Journal of Radiology, *17,* 2767-2779

Kasahara, K., Shiba, K., Ozawa, T., Okuda, K., & Adachi, M. (2002). Correlation Between the Bronchial Subepithelial Layer and Whole Airway Wall Thickness in Patients with Asthma. *Thorax, 57*, 242-246

Kolb, M., Margetts, P.J., Anthony, D.C., Pitossi, F., & Gauldi, J. (2001). Transient Expression of IL-1β Induces Acute Lung Injury and Chronic Repair Leading to Pulmonary Fibrosis. *The Journal of Clinical Investigation*, *107*(12), 1529-1536

Kolb, M., Bonniaud, P., Galt, T., Sime, P.J., Kelly, M.M., Margetts, P.J., & Gauldie, J. (2002). Differences in Fibrogenic Response after Transfer of Active Transforming Growth Factor-β1 Gene to Lung of "Fibrosis-Prone" and "Fibrosis-Resistant" Mouse Strains. *American Journal of Respiratory Cellular and Molecular Biology, 27*, 141-150

Langheinrich, A. C., Leithäuser, B., Greschus, S., von Gerlach, S., Breithecker, A. Matthias, F.R., Rau, W.S., & Bohle, R.M. (2004). Acute Rat Lung Injury: Feasibility of Assessment with Micro-CT. *Radiological Society of North America, 233*(1), 165-171

Lederlin, M., Ozier, A., Montaudon, M., Begueret, H., Ousova, O., Marthan, R., Berger, P. & Laurent, F. (2010). Airway Remodelling in a Mouse Asthma Model Assessed by In-Vivo Respiratory-Gated Micro-Computed Tomography. *European Radiology, 20*, 128-137

Lee, H.J., Goo, J.M., Kim, N.R., Kim M.A. Chung, D.H., Son, K.R., Kim, H.C., Lee, C.H., Park, C.M., Chun, E.J., & Im, J.G. (2008). Semiquantitative Measurement of Murine Bleomycin-Induced Lung Fibrosis in In Vivos and Postmortem Conditions Using Microcomputed Tomography: Correlation with Pathologic Scores-Initial Results. *Investigative Radiology, 43*(6), 453-460

Leigh, R., Ellis, R, Wattie, J., Southam, D.S., de Hoogh, M., Gauldie, J., O'Byrne, P.M. & Inman, M. (2002). Dysfunction and Remodelling of the Mouse Airway Persist after Resolution of Acute Allergen-Induced Airway Inflammation. *American Journal Respiratory Cellular and Molecular Biology, 27*, 526-535

Levi, C., Gray, J.E., McCullough, E.C., & Hattery, R.R. (1982). The Unreliability of CT Numbers as Absolute Values. *American Journal of Roentgenology, 139*, 443-447

Little, S.A., Sproule, M.W., Cowan, M.D., Macleod, K.J., Robertson, M., Love, J.G., Chalmers, G., McSharry, C. & Thomson, N.C. (2002). High Resolution Computed Tomographyic Assessment of Airway Wall Thickness in Chronic Asthma: Reproducibility and Relationship with Lung Function and Severity. *Thorax, 57*, 247-253

Lundblad, L.K.A., Thompson-Figueroa, J., Allen, G.B., Rinaldi, L., Norton, R.J., Irvin, C.G., & Bates, J.H.T. (2007). Airway Hyperresponsiveness in Allergically Inflammed Mice. *American Journal of Respiratory and Critical Care Medicine, 175*, 768-774

Lynch, D.A. (2007). Quantitative CT of Fibrotic Interstitial Lung Disease. *Chest, 131*, 643-644

Melgert, B.N., Postma, D.S., Kuipers, I., Geerlings, M., Luinge, M.A., van der Strate, B.W., Kerstjens, H.A., Timens, W. & Hylkema, M.N. (2005). Female Mice are More Susceptible to the Development of Allergic Airway inflammation than Male Mice. *Clinical and Experimental Allergy, 35(11)*, 1496-1503

Moore, B.B. & Hogaboam, C.M. (2008). Animal Models of Human Lung Disease: Murine Models of Pulmonary Fibrosis. American Journal of Physiology: *Lung Cellular and Molecular Physiology, 294*, L152-L160

Namati, E., Thiesse, J., Sieren, J.C., Ross, A., Hoffman, E.A., & McLennan, G. (2010). Longitudinal Assessment of Lung Cancer Progression in the Mouse Using In Vivo Micro-CT Imaging. *Medical Physics, 37*, 4793-4805

Nials, A.T. & Uddin, S. (2008). Mouse Models of Allergic Asthma: Acute and Chronic Allergen challenge. *Disease Models & Mechanisms, 1*, 213-220

Paulus, M.J., Gleason, S.S., Kennel, S.J., Hunsicker, P.R., & Johnson, D.K. (2000). High Resolution X-ray Computed Tomography: An Emerging Tool for Small Animal Cancer Research. *Nature: Neoplasia, 2*(1-2), 62-70

Postnov, A. A., Meurrens, K., Weiler, H., Van Dyck, D., Xu, H., Terpstra, P., & De Clerck, N.M. (2005). In Vivo Assessment of Emphysema in Mice by High Resolution X-ray Microtomography. *Journal of Microscopy, 220*, 70-75

Poulsen, K. & Simonsen, J. (2007). Computed Tomography as Routine in Connection with Medico-Legal Autopsies. *Forensic Science International, 171*, 190-197

Ritman, E. L. (2005). Micro-Computed Tomography of the Lungs and Pulmonary-Vascular System. *Proceedings of the American Thoracic Society, 2*, 477-480

Robinson, P. J & Kreel, L. (1979). Pulmonary Tissue Attenuation with Computed Tomography: Comparison of Inspiration and Expiration Scans. *Journal of Computer Assisted Tomography, 3*(6), 740-748

Rodt, T., von Falck, C., Dettmer, S., Halter, R., Maus, R., Ask, K., Kolb, M., Gauldie, J., Länger, F., Hoy, L., Welte, T., Galanski, M., Maus, U.A. & Borlak, J. (2010). Micro-Computed Tomography of Pulmonary Fibrosis in Mice Induced by Adenoviral Gene Transfer of Biologically Active Transforming Growth Facter-β1. *Respiratory Research, 11*(181), 1-8

Saavedra, M.T. & Lynch, D.A. (2009). Emerging Roles for CT Imaging in Cystic Fibrosis. *Radiology, 252*(2), 327-329

Santos, F.B., Nagato, L.K.S., Boechem, N.M., Negri, E.M., Guimarães, A., Capelozzi, V.L., Faffe, D.S., Zin, W.A., & Rocco, R.M. (2006) Time Course of Lung Parenchyma Remodelling in Pulmonary and Extrapulmonary Acute Lung Injury. *Journal of Applied Physiology, 100*(1), 98-106

Schuster, D.P., Kovacs, A., Garbow, J., & Piwnica-Worms, D. (2004). Recent Advances in Imaging the Lungs of Intact Small Animals. *American Journal of Respiratory Cell and Molecular Biology, 30*(2), 129-138

Simon, B. A., Christensen, G.E., Low, D.A., & Reinhardt, J.M. (2005). Computed Tomography Studies of Lung Mechanics. *Proceedings of the American Thoracic Society, 2*, 517-521

Sime, P.J., Xing, Z., Graham, F. L., Csaky, K. G., & Gauldie, J. (1997). Adenovector-Mediated Gene Transfer of Active Transforming Growth Factor-Beta1 Induces Prolonged Severe Fibrosis in Rat Lung. *Journal of Clinical Investigation,* 100, 768-776

Smith, H.J. (2011). Modalities and Methods: Computed Tomography. GE Health, Medical Diagnostics, *Medcyclopaedia.com*, accessed Jan 15, 2011

Sont, J.K., Willems, L.N.A., Bel, E.H., van Krieken, J.H.J.M., Vandenbroucke, J.P., Sterk, P.J., & AMPUL Study Group. (1999). Clinical Control and Histopathological Outcome of Asthma when Using Airway Hyperresponsiveness as an Additional Guide to Long-Term Treatment. *American Journal of Respiratory and Critical Medicine*, *159*, 1043-1051

Southam, D.S., Ellis, R., Wattie, J., Glass, W., & Inman, M.D. (2008). Goblet Cell Rebound and Airway Dysfunction with Corticosteroid Withdrawal in a Mouse Model of Asthma. *American Journal of Respiratory and Critical Medicine*, *178*(11), 1115-1122

Stoel, B.C. & Stolk, J. (2004). Optimization and Standardization of Lung Densitometry in the Assessment of Pulmonary Emphysema. *Investigative Radiology, 39*(11), 681-688

Sumikawa, H., Johkoh, T., Yamamoto, S., Yanagawa, M., Inoue, A., Honda, O. Yoshida, S., Tomiyama, N., & Nakamura, H. (2009). Computed Tomography Values Calculation and Volume Histogram Analysis for Various Computed Tomographic Patterns of Diffuse Lung Diseases. *Journal of Computer Assisted Tomography, 33*(5), 731-738

Suryanarayana,C. & Norton, M.G. (1998). X-Ray Diffraction: A Practical Approach. Plenum Press, New York, N.Y. 14-17

Sverzellati, N., Calabrò, E., Chetta, A., Conari, G., Larici, A.R., Mereu, M., Cobelli, R., De Filippo, M., & Zompatori, M. (2007). Visual Score and Quantitative CT Indices in Pulmonary Fibrosis: Relationship with Physiologic Impairment. *Radiologia Medica*, *112*, 1160-1172

Takeda, K. & Gelfand, E. W. (2009). Mouse Models of Allergic Diseases. Current Opinion in *Immunology, 21*, 660-665

Tanimoto, H. & Arai, Y. (2009). The Effect of Voxel Size on Image Reconstruction in Cone-Beam Computed Tomography. *Oral Radiology, 25*(2), 149-153

Taube, C., Dakhama, A., & Gelfand, E.W. (2004). Insights into the Pathogenesis of Asthma Utilizing Muring Models. *International Archives of Allergy and Immunology, 135(2)*, 173-186

Warshamana, G.S., Pociask, D.A., Fisher, K.J., Liu, J.-Y., Sime, P.J. & Brody, A.R. (2002). Titration of Non-Replicating Adenovirus as a Vector for Transducing Active TGF-β1 Gene Expression Causing Inflammation and Fibrogenesis in the

Lungs of C57BL/6 Mice. *International Journal of Experimental Pathology, 83*, 183-201

Washko, G.R., Criner, G.J., Mohsenifar, Z., Sciurba, F.C., Sharafkhaneh, A., Make, B.J., Hoffman, E.A., & Reilly, J.J. (2008). Computed Tomographic-Based Quantification of Emphysema and Correlation of Pulmonary Function and Mechanics. *Journal of Chronic and Obstructive Pulmonary Disease,* 5, 177-186

Wegener, O.H., Koeppe, P., & Oeser, H. (1978). Measurement of Lung Density by Computed Tomography. *Journal of Computer Assisted Tomography, 2*, 263-273

Wegmann, M., Fehrenbach, H., Fehrenbach, A., Held, T., Schramm, C., Garn, H., & Renz, H. (2005). Involvement of Distal Airways in a Chronic Model of Experimental Asthma. *Clinical and Experimental Allergy, 35*, 1263-1271

Wheater, P.R., Burkitt, H.G., Daniels, V.G. (1987). Functional Histology: A Text and Colour Atlas. Longman Group UK Limited, 23-24

Xing, Z., Braciak, T., Jordana, M., Croitoru, K., Graham, F.L., & Gauldie, J. (1994). Adenovirus-Mediated Cytokine Gene Transfer at Tissue Sites: Overexpression of IL-6 Induces Lymphocytic Hyperplasia in the Lung. *The Journal of Immunology, 153*(9), 4059-4069

Yamashiro, T., Matsuoka, S., Estépar, R.S.J., Dransfield, M.T., Diaz, A., Reilly, J.J., Patz, S., Murayama, S., Silverman, E.K., Hatabu, H., & Washko, G.R. (2010). Quantitative Assessment of Bronchial Wall Attenuation With Thin-Section CT: An

Indicator of Airflow Limitation in Chronic Obstructive Pulmonary Disease. American Journal of Roentgenology: *Cardiopulmonary Imaging, 195*, 363-369

Zavaletta, V.A., Bartholmai, B.J., & Robb, R.A. (2007). High Resolution Multidetector CT-Aided Tissue Analysis and Quantification of Lung Fibrosis. *Academic Radiology*, *14*, 772-787

9 APPENDIX

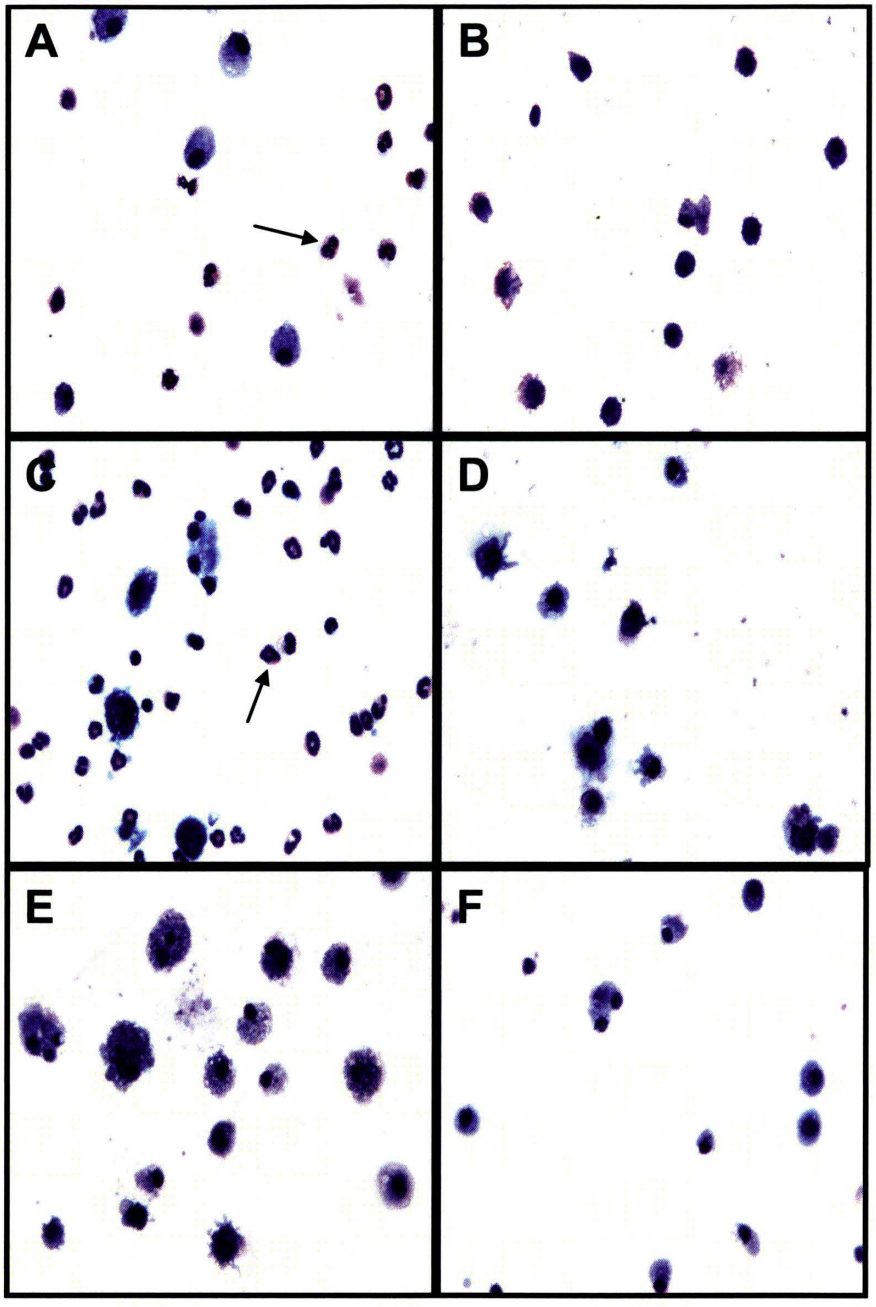

Figure 36. Representative cells in BALF from asthma models. (A) acute HDM exposure (HDMA), (B) vehicle treated control (VEH-HDMA), (C) chronic exposure (HDME), (D) VEH-HDME, (E) recovery following chronic exposure (HDMR), and (F) its vehicle-treated control (VEH-HDMR). Black arrows indicate eosinophils.

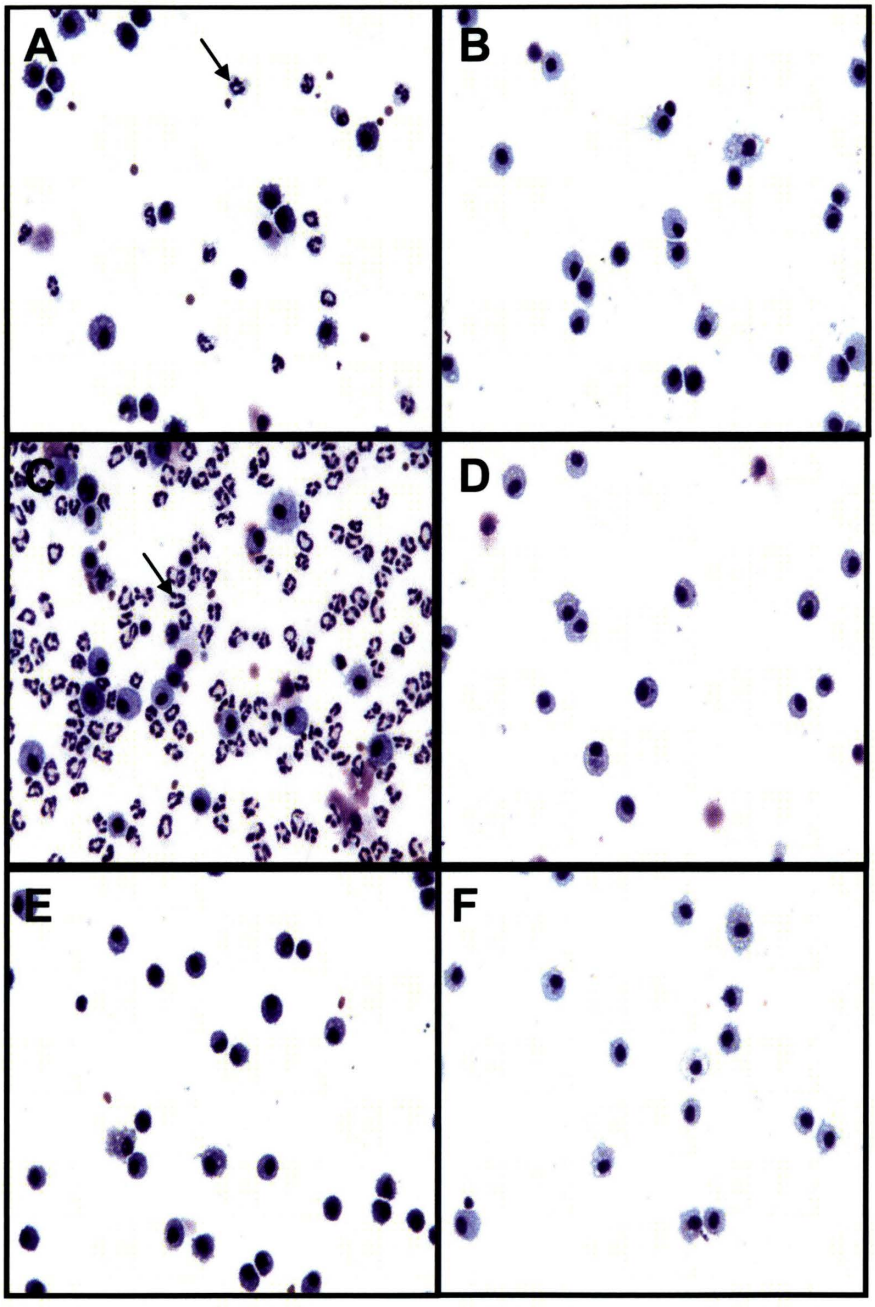

Figure 37. Representative cells in BALF from LPS induced neutrophilic inflammation models (X40). (A) 7 hrs post LPS, (B) vehicle treated control (VEH-7h), (C) 24 hrs post LPS, (D) vehicle treated control (VEH-24h), (E) and 2 weeks post LPS, and (F) its vehicle-treated control (VEH-2w). Arrows indicate neutrophils.

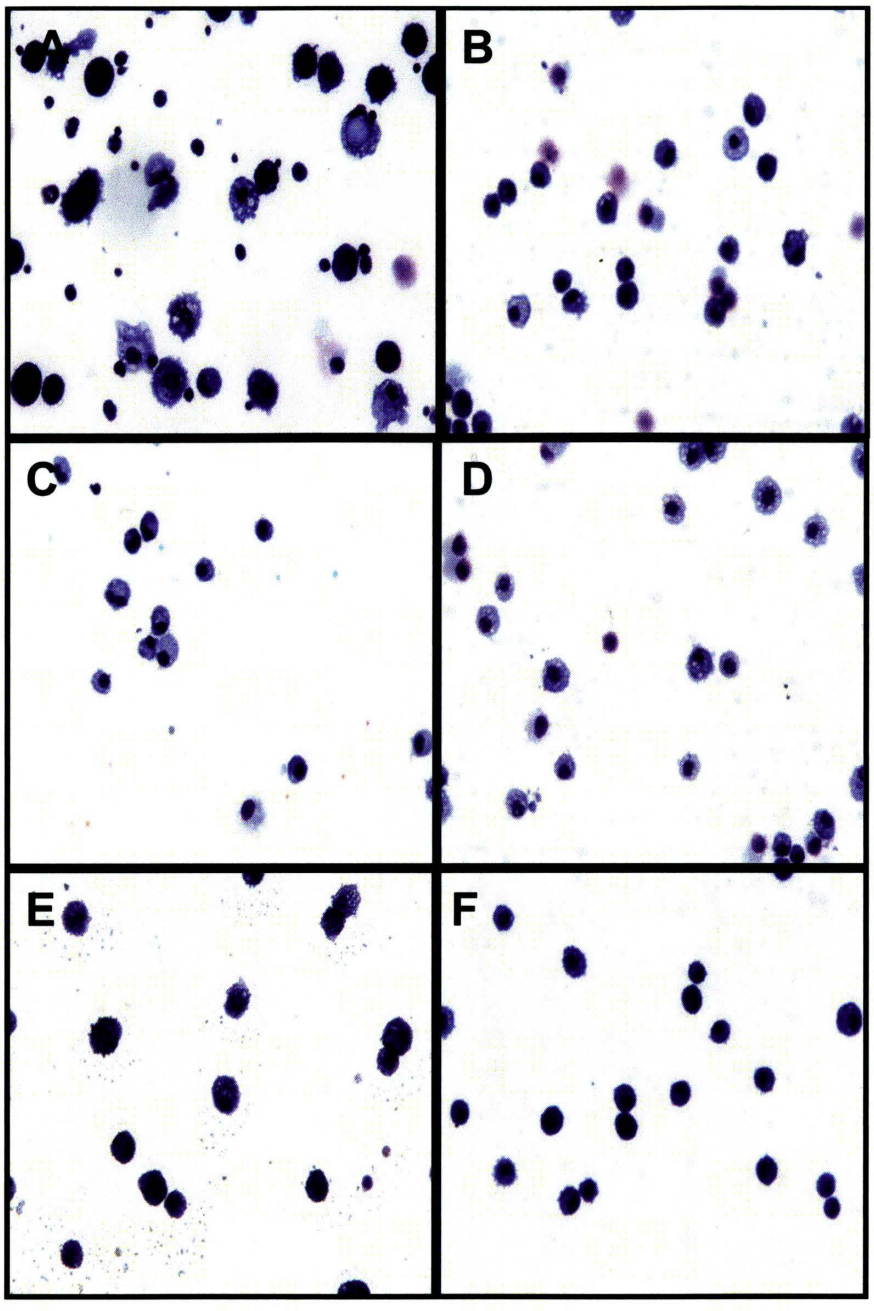

Figure 38. Representative cells in BALF from adTGF-β induced PF models. (A) 2 weeks, (B) vehicle treated control (VEH-2w), (C) 3 weeks, (D) VEH-3w, (E) and 4 weeks, and (F) vehicle-treated control (VEH-4w) after intratracheal adTGF-β delivery.

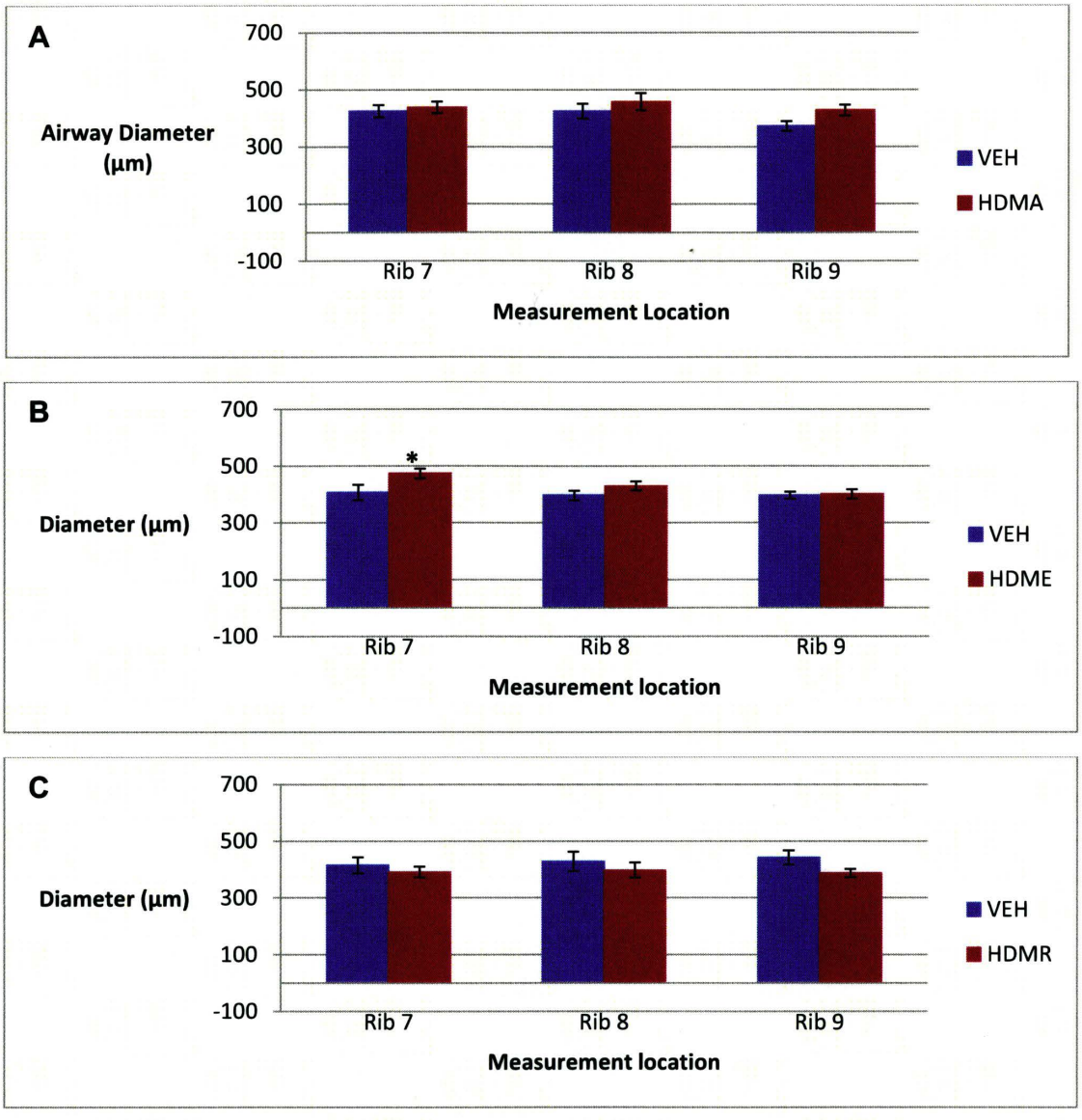

Figure 39. Mean airway diameters of the asthma model. The purpose of this analysis was to compare if differences in airway diameter exist between the asthma and control groups since the segmentation includes the airway lumen. (A) acute asthma model (HDMA) (n = 6) vs. age-matched, vehicle treated controls (VEH) (n = 6); chronic asthma model (HDMA) (n = 12) vs. age-matched, vehicle treated controls (VEH) (n = 12); andthe recovery following chronic HDM exposure (HDMR) (n = 6) vs. age-matched, vehicle treated controls (VEH) (n = 6). Error is in SEM. (*) indicates significant difference ($P < 0.05$).

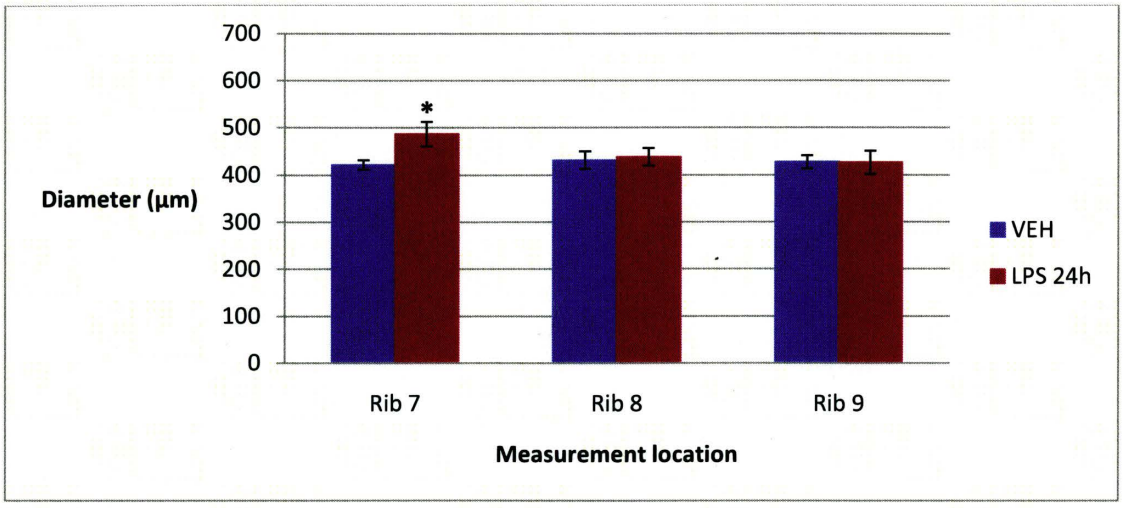

Figure 40. Mean airway diameters of mice 24 hrs after receiving LPS (n = 6) compared to controls (VEH) (n = 6). The purpose of this analysis was to compare if differences in airway diameter exist between the LPS 24h and control groups since the segmentation includes the airway lumen.

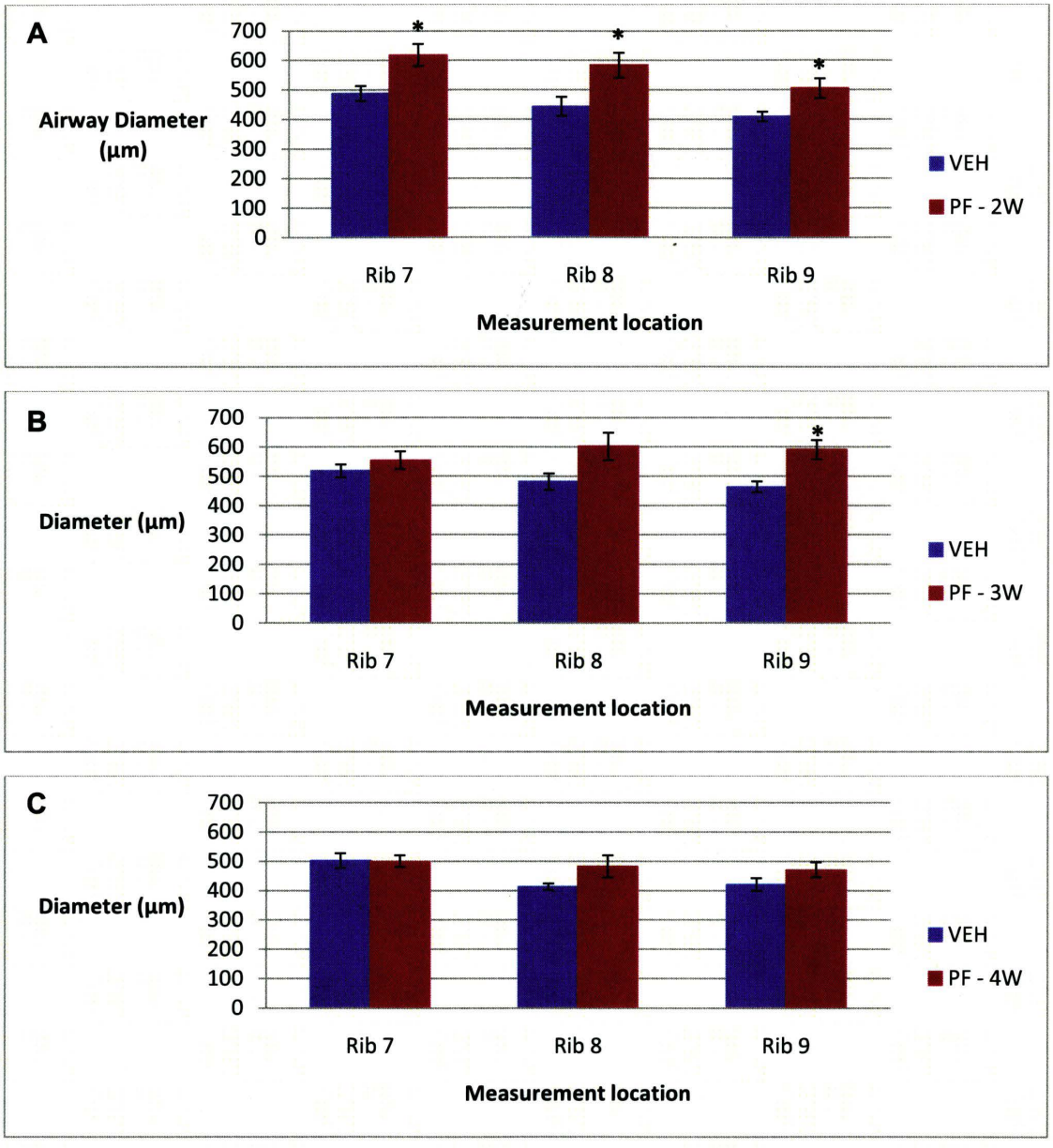

Figure 41. Mean airway diameters of pulmonary fibrosis model. The purpose of this analysis was to compare if differences in airway diameter exist between the pulmonary fibrosis and control groups since the segmentation contains the airway lumen. Time point at (A) 2 weeks (PF-2w) (n = 12), (B) 3 weeks (PF-3w) (n = 4), and (C) 4 weeks (PF-4w) (n = 5) after delivery of adTGFβ-1 compared to their age-matched, vehicle treated control groups: VEH-2w (n=6), VEH-3w (n=6), VEH-4w (n = 6). Error is in SEM. (*) indicates significant difference ($P < 0.05$).

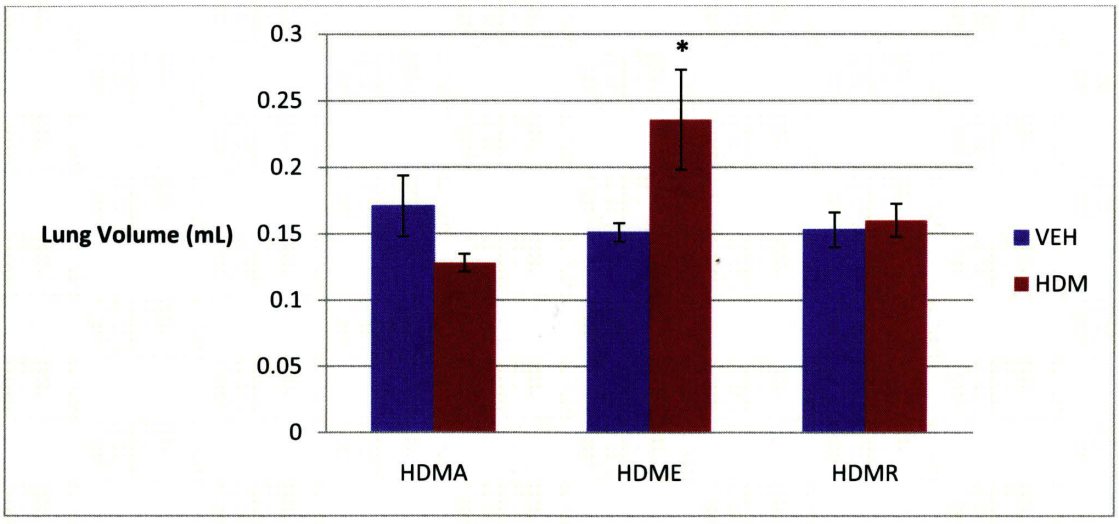

Figure 42. Average lung volumes of mice in the asthma model compared to controls. Volumes are derived from thoracic segmentation of CT images at end expiration. The groups compared were: HDMA (n=6); VEH-HDMA (n=6); HDME (n=12), VEH-HDME (n=12); HDMR (n=6), VEH-HDMR (n=6). Error is in SEM. (*) $P < 0.05$

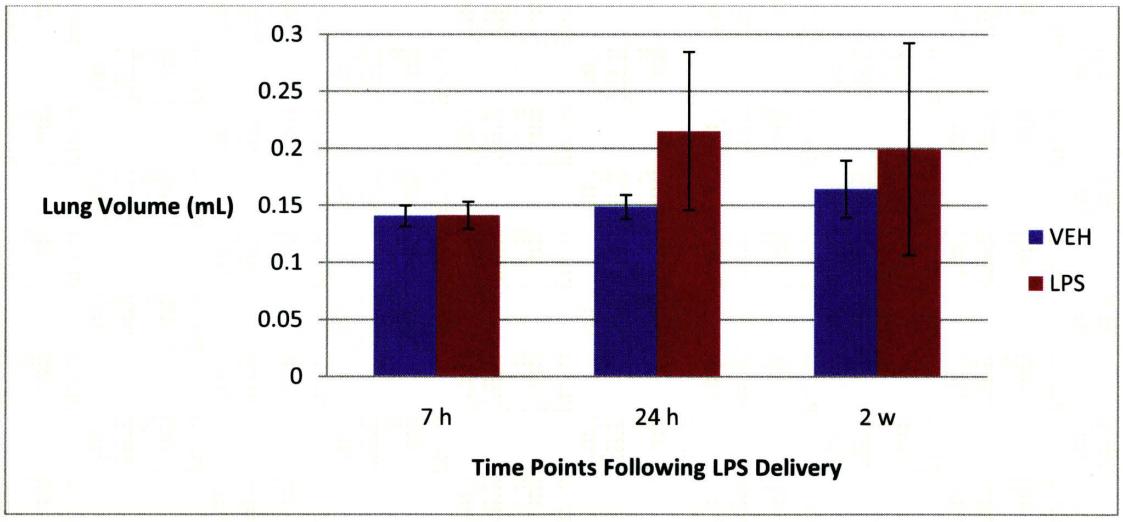

Figure 43. Average lung volumes of mice in the LPS model after delivery of compared to controls. Volumes are derived from thoracic segmentation of CT images at end expiration. The groups compared were: LPS-7h (n=6) vs. VEH-7h (n=12); LPS-24h (n=7) vs. VEH-24h (n=8); LPS-2w (n=6) vs. VEH-2w (n=4). Error is in SEM.

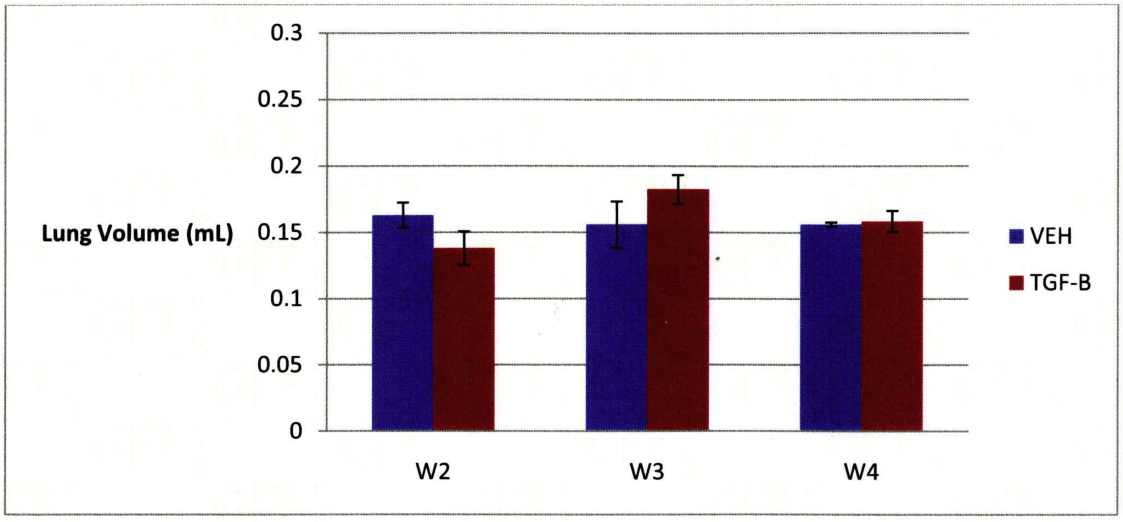

Figure 44. Average lung volumes of mice in the pulmonary fibrosis model after delivery of adTGFβ-1 compared to controls. Volumes are derived from thoracic segmentation of CT images at end expiration. The groups compared were: PF-2w (n=11) vs. VEH-2w (n=6); PF-3w (n=7) vs. VEH-3w (n=6); PF-4w (n=8) vs. VEH-4w (n=6). Error is in SEM.

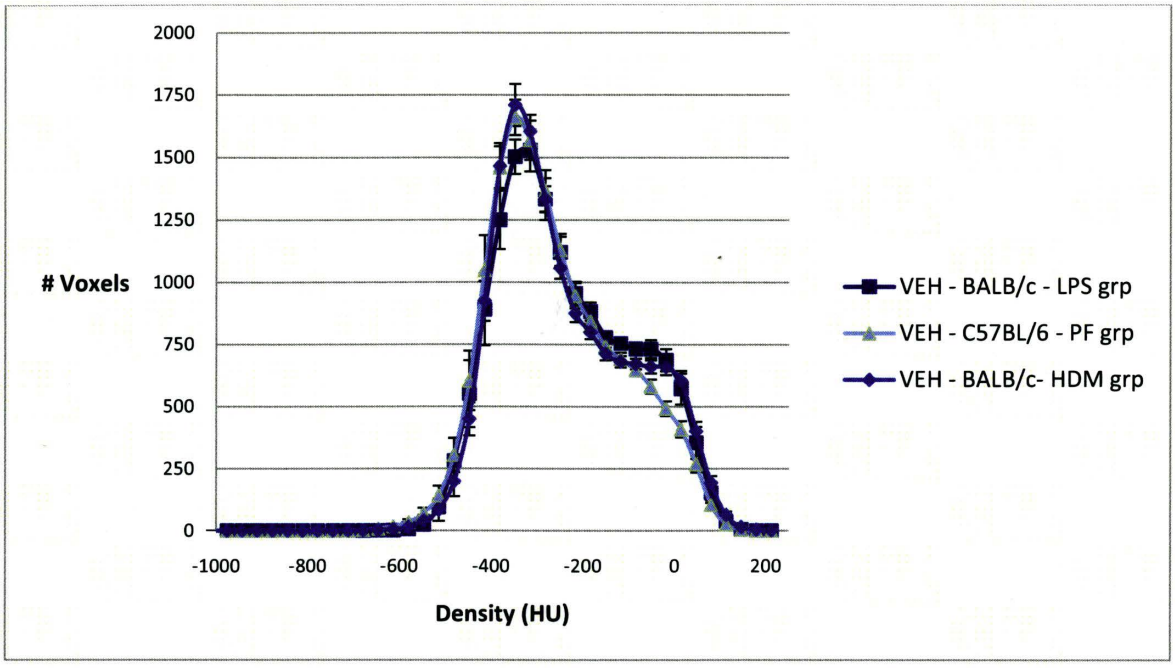

Figure 45. Comparison of the density distribution of selected large airways of two mouse strains (BALB/c and C57BL/6). This plot presents density distribution derived from large airway segmentations in CT images of all examined controls groups of each disease model: the LPS induced neutrophilic inflammation (VEH – BALB/c – LPS group) (n=16), asthma (VEH – BALB/c – HDM group) (n=24), and PF (VEH – BALB/c – PF group) (n=18) models. The purpose of this analysis is to assess if density differencescould be present with altered mouse strain. No differences were found between each of the three control groups. All points represent the mean values. A one way ANOVA was performed over all bins comparing the controls to each other. Error is in SEM.

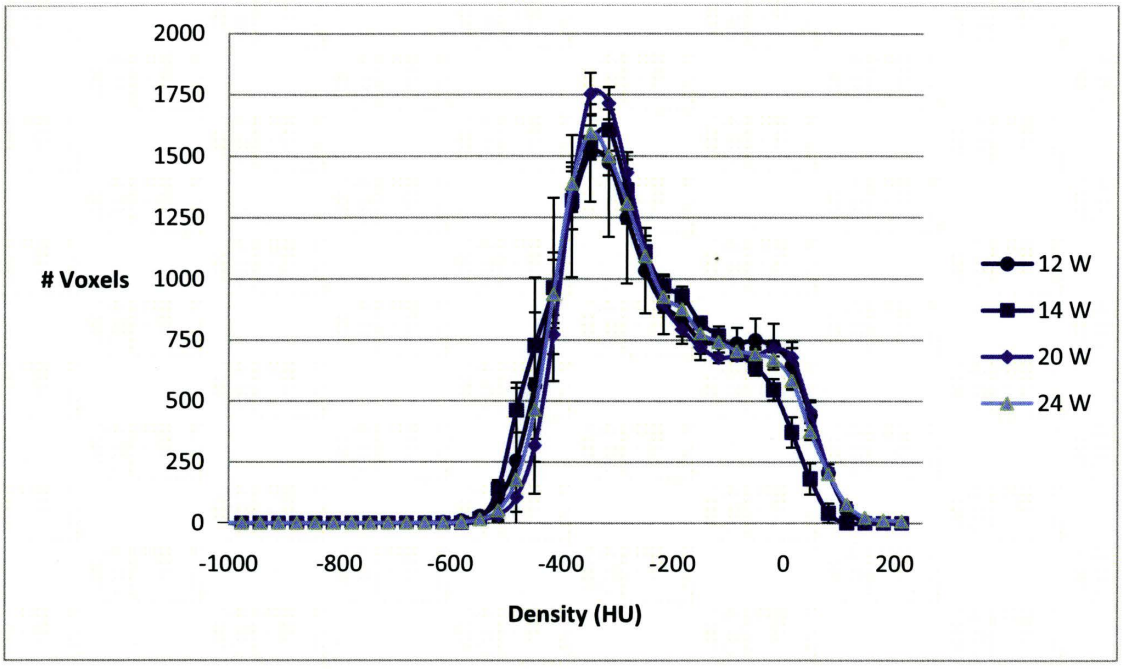

Figure 46. Age comparison of the density distributions of selected large airways in control groups of BALB/c mice. This plot presents density distribution derived from large airway segmentations in CT images of all examined control groups: ~12 weeks old (12 W) (n=8); ~14 week old (14 W) (n=4); ~20 week old (20 W) (n=12); and ~24 week old (24 W) (n=6) female BALB/c mice. This examines density differences that could be present with altered age. No differences were found between each of the three control groups. All points represent the mean values. A one way ANOVA was performed over all bins comparing the controls to each other. Error is in SEM.

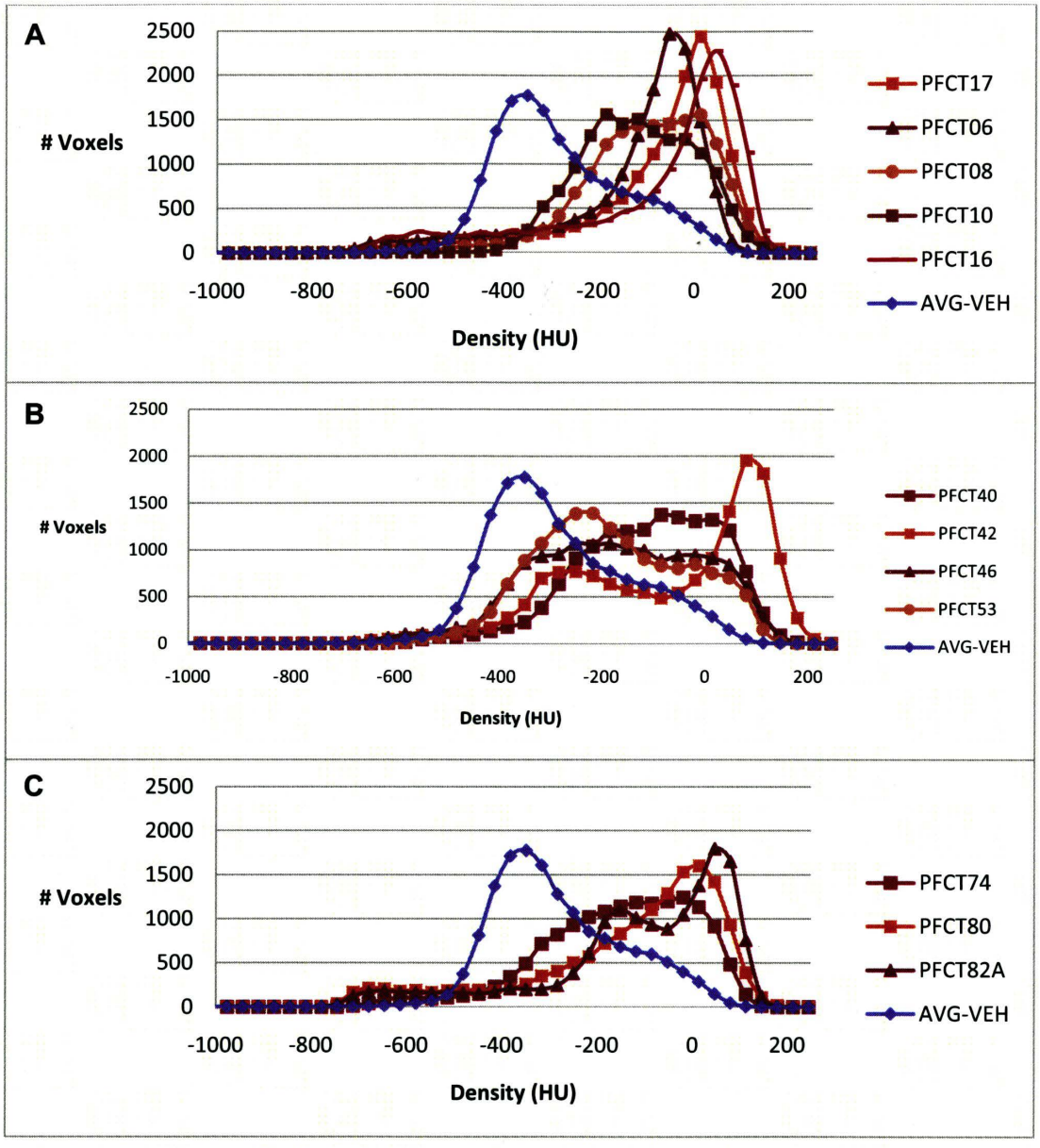

Figure 47. CT densitometry output from large airway segmentation in mice 2w after delivering TGF-β1 compared to the averaged frequency distribution of their age matched and adenovirus vector treated control (AVG-VEH). The above three plots includes data from airway segmentation in all female C57BL/6 mice used in the data for the week 2 time point. The label PFCT indicates each individual subject exposed to adTGFβ-1; and AVG-VEH indicates the average control group: (A) Group 1; Group 2 (B); Group 3 (C).

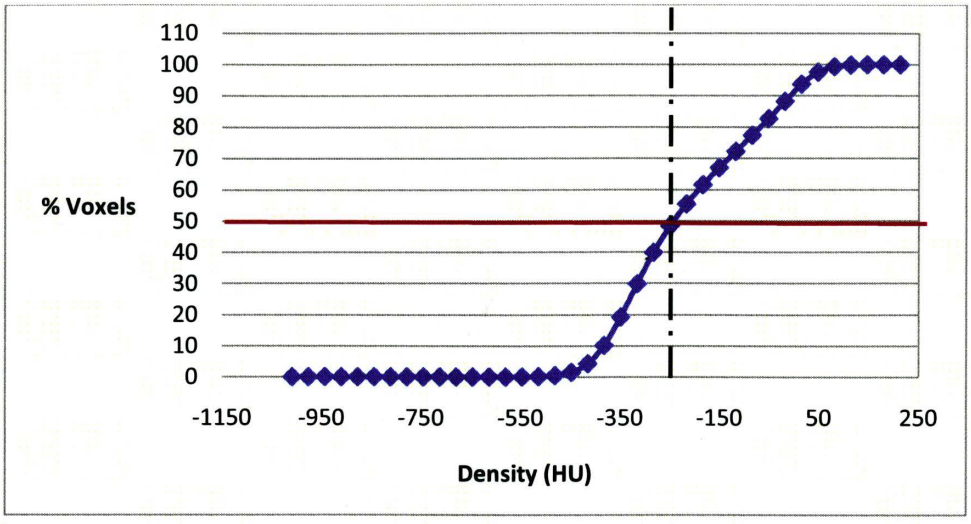

Figure 48. Representational cumulative plot of baseline data in a large airway segmentation. Cumulative data from baseline airway segmentation density plots of all mouse models. The red line indicates 50% of voxels. The dotted line indicates the median density (-249.5 HU).

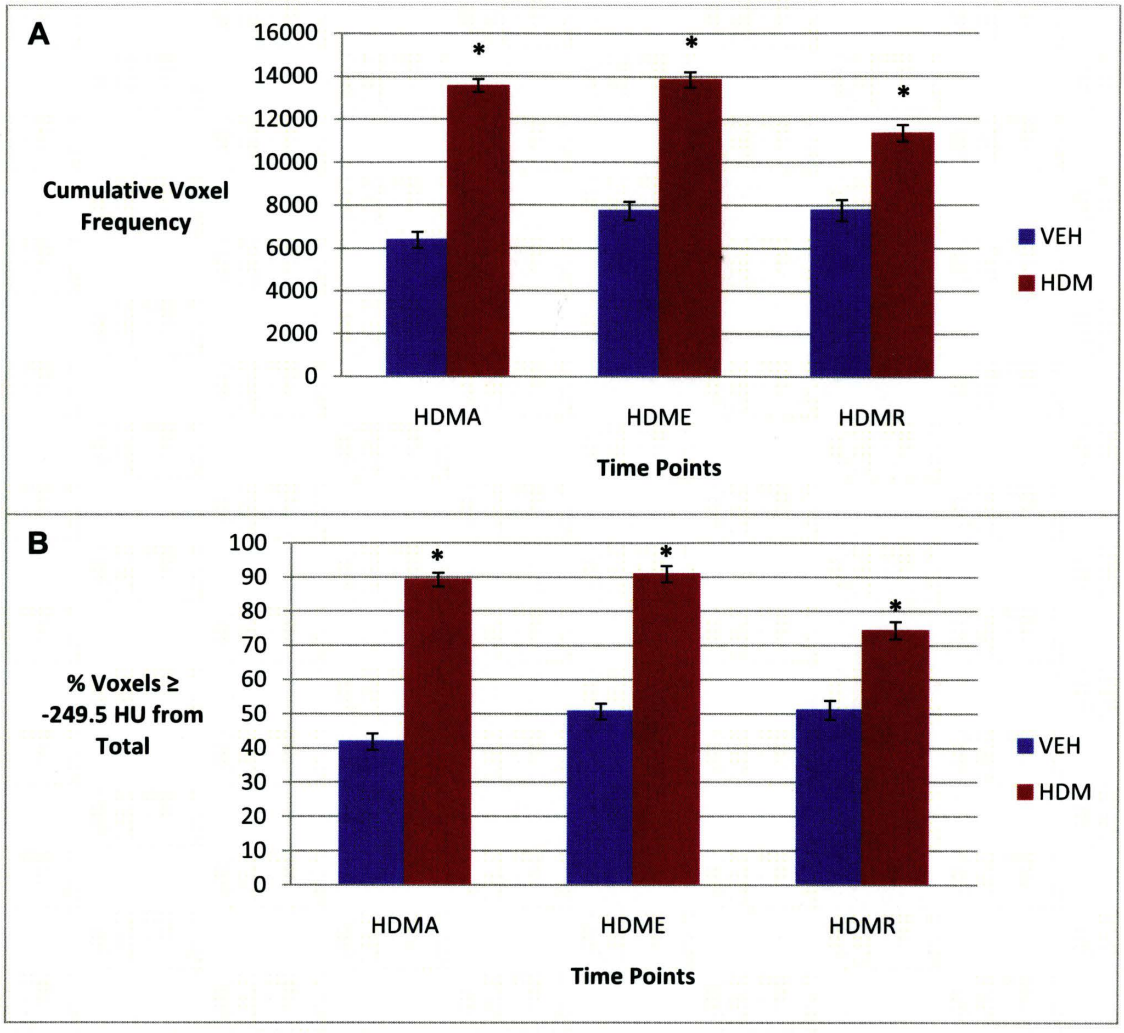

Figure 49. Cumulative voxel frequency from -249.5 to 220 HU of the large airway segmentations in the three different mouse asthma models. Total number of voxels was measured from -249.5 HU and greater. The data is expressed as (A) the cumulative number of voxels in the density range of -249.5 HU to 220 HU and (B) % voxels in the -249.5 to 220 HU range compared to total voxels in airway segmentation. HDMA (n=6); VEH-HDMA (n=6); HDME (n=12), VEH-HDME (n=12); HDMR (n=6), VEH-HDMR (n=6). All points represent the mean values. Error is SEM. (*) indicates significant difference ($P < 0.05$).

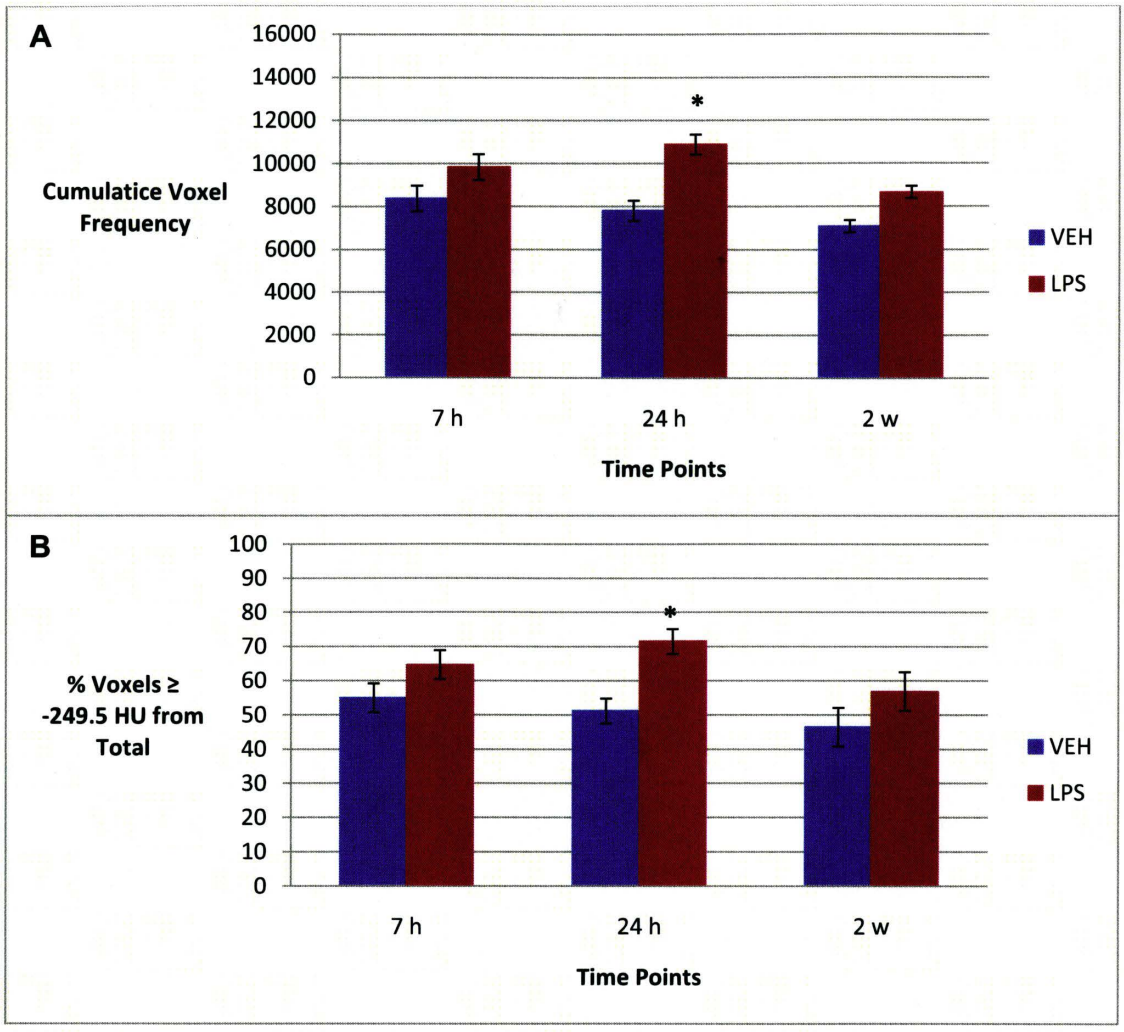

Figure 50. Cumulative voxel frequency from -249.5 to 220 HU of the large airway segmentations of mice following exposure to LPS. The total number of voxels was measured from -249.5 HU and greater in the LPS model. The data is expressed as (A) the cumulative number of voxels in the density range of -249.5 HU to 220 HU and (B) % voxels in the -249.5 to 220 HU range compared to total voxels in airway segmentation. LPS-7h (n=6), VEH-7h (n=12); LPS-24h (n=7), VEH-24h (n=8); LPS-2w (n=6), VEH-2w (n=4). All points represent the mean values. Error is SEM. (*) indicates significant difference ($P < 0.05$).

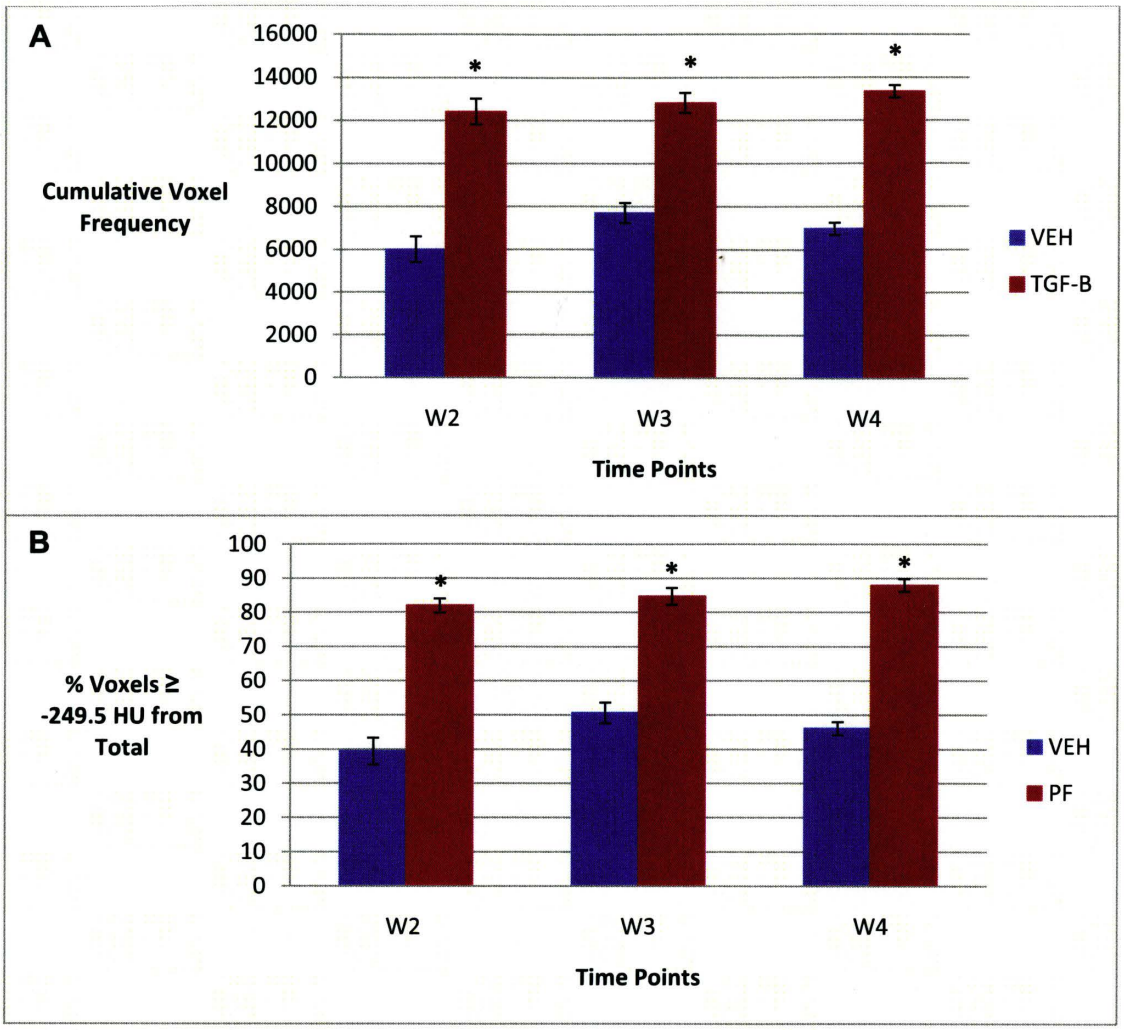

Figure 51. Cumulative voxel frequency from -249.5 to 220 HU of the large airway segmentations in mouse models of pulmonary fibrosis following delivery of TGF-B1 at 2 weeks (n = 12), 3 weeks (n = 12), and 4 weeks (n = 10). The total number of voxels was measured from -249.5 HU and greater in the PF model. The data is expressed as (A) the cumulative number of voxels in the density range of -249.5 HU to 220 HU and (B) % voxels in the -249.5 to 220 HU range compared to total voxels in airway segmentation. PF-2w (n=11) vs. VEH-2w (n=6); PF-3w (n=7) vs. VEH-3w (n=6); PF-4w (n=8) vs. VEH-4w (n=6). All points represent the mean values. Error is SEM. (*) indicates significant difference ($P < 0.05$).